Synthesis, Characterization and Catalytic Performance of Cerium Dioxide with Different Morphologies for HCl Oxidation

Chenwei Li

Synthesis, Characterization and Catalytic Performance of Cerium Dioxide with Different Morphologies for HCl Oxidation

Cumulative dissertation

Presented by

Chenwei Li

Born in 11.04.1990

in Anhui, China

Submitted to the

Faculty of Biology and Chemistry

and prepared in the

Institute of Physical Chemistry

For the degree of

Doktor der Naturwissenschaften

(*Dr. rer. nat.*)

Justus Liebig University Giessen, Germany

Giessen 2018

This thesis is accepted as a doctoral dissertation in fulfillment of the requirements for the degree of *Doctor Rerum Naturalium* by the Faculty of Biology and Chemistry, Justus Liebig University Giessen, Germany.

Members of the thesis committee: Prof. Dr. Herbert Over

Prof. Dr. Yanglong Guo

Prof. Dr. Bernd M. Smarsly

Prof. Dr. Peter J. Klar

1. Reviewer   Prof. Dr. Herbert Over

Physical-Chemistry Institute, Justus Liebig University Giessen

2. Reviewer   Prof. Dr. Yanglong Guo

Research Institute of Industrial Catalysis, East China University of Science & Technology

I declare that I have completed this dissertation single-handedly without the unauthorized help of second party and only with the assistance acknowledged therein. I have appropriately acknowledged and referenced all text passages that are derived literally from or based on the content of published or unpublished work of others, and all information that relates to verbal communications. I have abided by the principles of good scientific conduct laid down in the character of the Justus-Liebig-University of Giessen in carrying out the investigations described in the dissertation.

Giessen, 11,04,2018

Chenwei Li

Acknowledgements

I would like to cordially express my deepest appreciation to Prof. Dr. Herbert Over, who provided me the opportunity to work in such an excellent group for my Dr. rer. nat. thesis as a joint Ph.D student in Justus Liebig University Giessen. It is a great honor to work with him on this very challenging and interesting project of Ce based catalysts for HCl oxidation. Without his guidance and continuous encouragement, this thesis could not have reached its present form. Through every discussion with him I have obtained not only the scientific knowledge, but also learned how to deeply discuss the experimental data and then efficiently propel the research project. I am also grateful for his constructive comments towards scientific writing and preparation of presentations. All what I learned from him will play an important role in my future work and accompany with me in my whole life.

Equally, I extend my appreciation to my supervisor Prof. Dr. Yanglong Guo in China, who led me into the heterogeneous catalysis world, especially in the field of HCl oxidation and copper-based catalysts. It is my honor to work as a Master-Ph.D student in his research group. His rich experiences in the field of industrial catalysis and thoughtful guidance have taught me not only the scientific and engineering knowledge, but also how to perform the research work for fulfilling the requirement of industrial application. All of these skills I learned from him is helpful for my future work and accompany with me in the rest of my life.

I am very grateful to Prof. Dr. Bernd M. Smarsly, who co-supervised my scientific work in Justus Liebig University Giessen. He has contributed a lot to the preparation of catalysts, not only for supplying the characterization apparatus but also for fruitful discussion about the crystal growth during hydrothermal method. I thank him for applying the beam time of in-situ SAXS measurement for my materials and helping analyze the data comprehensively. I appreciate also his comments and the polishing of english writing in my scientific publications.

I specially thank Prof. Dr. Igor Djerdj from J. J. Strossmayer University of Osijek, who gave strong support in the Rietveld refinement analyses of my XRD data.

VIII

Table of Content

X

1. Abstract

CeO_2 represent a promising alternative for the widely used Ru-based catalysts for the HCl oxidation reaction in order to recover Cl_2. CeO_2 powder has been extensively studied previously, which has clarified the reaction mechanism, the relation between the catalytic activity and feed composition, the reaction temperature, and the Cl coverage on the surface. In general, particles in powder catalysts expose various facets, predominantly low index surfaces with low surface energies. However, correlation between the specific facets and catalytic performance are still unknown. Thus the investigation of catalytic activity and stability over shape-controlled CeO_2 nanoparticles (nano-rods, nano-cubes, and nano-octahedrons with exposing preferentially (110), (100), and (111) facets, respectively) is the main research focus of this Ph.D project.

This cumulative dissertation comprises two main parts: a literature review which includes the investigation of the HCl oxidation reaction and application of Ce-based catalysts and my research results including two peer-reviewed scientific publications and one completed manuscript to be submitted as scientific publications.

The introduction starts with the motivation of HCl oxidation to recover the Cl_2 and the investigation over different metal-based catalysts, revealing that CeO_2 is a promising catalyst material to replace the industrialized RuO_2 catalysts. A brief review of the investigation of shape-controlled CeO_2 nanoparticles for some oxidizing reactions indicates that catalysts with specific facets show different catalytic activity and different reaction mechanism. Some studies of doped CeO_2 catalysts for enhancing its activity and stability on oxidizing reaction are discussed. Especially, Zr-doped CeO_2 nano-particles for the Deacon reaction are discussed explicitly.

In the first paper of this Ph.D project, the shape-controlled CeO_2 nanoparticles (nano-rods, nano-cubes, and nano-octahedrons) were prepared by hydrothermal method and their activity and stability were investigated for HCl oxidation reaction under two reaction conditions (mild: $Ar:HCl:O_2 = 7:1:2$ and harsh: $Ar:HCl:O_2 = 6:2:2$). Several kinds of characterizations (X-ray Diffraction (XRD), X-ray photoelectron spectroscopy (XPS), Transmission electron microscopy (TEM), Scanning electron microscope (SEM), and Oxygen storage capacity (OSC)) were performed for the as prepared CeO2 catalysts to investigate their physicochemical properties and how these properties affect the catalytic activity and stability. It turned out that nano-rods are most

active in terms of the Space time yield (STY), followed by the cubes and finally the octahedrons. The very same trend is reconciled with the Complete Oxygen Storage Capacity (OSCc) with the rods having the highest OSCc and the octahedrons having lowest one. Regarding the stability of these catalysts ex-situ characterizations were conducted after the HCl oxidation reaction by various techniques (i.e. XRD, XPS, and TEM). XRD showed the changes of bulk structures (i.e. formation of hydrate $CeCl_3$ crystal phase for the CeO_2 nano-cubes and CeO_2 nano-octahedron catalysts under harsh condition). Rietveld refinement of the XRD data discriminated the mixed phases and quantified the concentration of the crystal phase of $CeCl_3 \cdot nH_2O$, presenting the degree of chlorination. The surface compositional and morphological changes were addressed by XPS and TEM, respectively. The results indicated that rods are stable without any morphology change under harsh condition, while cubes and octahedrons are unstable, as can be determined by the destruction of their morphology and the forming the crystal phase of hydrate $CeCl_3$. However, for the mild reaction condition, all the catalysts are stable.

In the second paper we systematically investigated the catalytic stability as a function of temperature in order to clarify the correlation between the chlorination degree and the reaction temperature. A simple theoretical model based on pure thermodynamics for the chlorination of the catalyst to validate the experimental data. To visualize morphological changes and the phase transformations, the shape-controlled CeO_2 nano-cubes with facets of preferential (100) orientation were fabricated. Due to crystallinity of the formed $CeCl_3 \cdot nH_2O$ phase, the degree of chlorination was quantified by the Rietveld refinement. The results showed that CeO_2 is substantially chlorinated below 380 °C, revealing a low catalytic activity originated from the hydrate $CeCl_3$. While both the activity and chlorination degree change abruptly at 390 °C. Based on the model of chlorination for CeO_2, we discovered that the leading driving force for the chlorination is the formation of the side product H_2O. Thus, adding a small amount (1 %) of H_2O into the feed gas stream can essentially remove the driving force for chlorination, thereby improving the catalytic stability. This modelling result, evidenced by our experiment data, is not only helpful for understanding the catalytic mechanism of our catalytic system but might also be extended to other heterogeneously catalysed oxidation reactions, in particular where H_2O is formed as a by-product.

In the third paper, mixed $Ce_{1-x}Zr_xO_2$ (x = 2 %, 5 % and 20 %) nano-rods were successfully synthesized and were exposed to HCl oxidation reaction for 24 h under different reaction mixture

(10% O_2, 20%-30% HCl and balanced with Ar) at 430 °C to investigate their stability. For Pure CeO_2 nano-rods bulk chlorination already started at reaction mixtures of HCl:$O_2 > 2$, thus revealing a lower stability and a dramatic loss in activity. $CeCl_3 \cdot nH_2O$ was formed via nucleation and growth forming large single crystalline particles. A doping of 5 % Zr for the mixed $Ce_{1-x}Zr_xO_2$ catalysts already efficiently suppressed the bulk chlorination for a reaction mixture of Ar:HCl:$O_2 = 6.5:2.5:1$. XPS measurements revealed that the chlorine concentration is too high to be solely assigned to on-surface chlorine. Additional XPS measurements conducted after an oxygen plasma treatment verified that some of Cl penetrated into the near surface region. For even harsher reaction conditions (i.e. Ar:HCl:$O_2 = 6:3:1$) none of these $Ce_{1-x}Zr_xO_2$ catalysts were stable at 430 °C. However, even pure CeO_2 nano-rods were stable under such harsh reaction conditions when the reaction temperature was set to 500 °C.

2. Introduction and Motivation

2.1 Chlorine and HCl

Chlorine (Cl_2) serves as a basic element for the large-scale production of a great variety of indispensable chemicals and consumer products. Many sectors like water treatment, food safety, healthcare, transportation, energy and environment, advanced technology, defense and law enforcement and building construction depend on chlorine chemistry [1]. Among these, polyvinyl chloride (PVC) is one of the most major products in the chlorine chemistry, followed by organic chemistry products such as isocyanates and oxygenates [2]. The high utility of chlorine is elucidated by the so-called Chlorine Tree [**Figure 1.1**] which depicts manifold products of the chlorine related chemistry. Worldwide, the chlorine production has been rapidly increased since 1965 and the production is expected to grow continually.
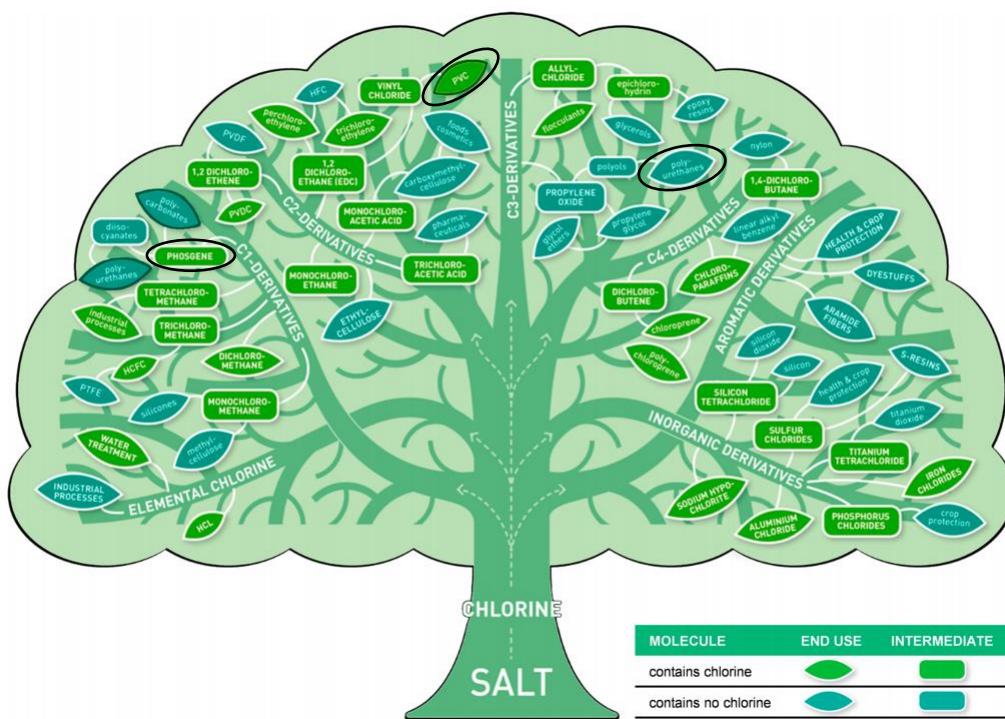

Figure 1.1. Products of the Chlorine Tree. Copyright 2016 Euro Chlor [2]

HCl is one of the inevitable by-products of these chlorine relevant processes and is produced far beyond its market demand. The main process leading to a large amount of HCl is the synthesis of polyurethanes and polycarbonates by the phosgene-mediated method. Methylene diphenyl

diisocyanate (MDI) and toluene diphenyl diisocyanate (TDI) are the key raw materials in the production of polyurethanes. During the phosgenation step 4 moles of HCl per mole of MDI or TDI are produced [3]. The report forecasts the global MDI market to grow at a Compound Annual Growth Rate (CAGR) of 6.5 % by volume during 2014-2019. The largest companies in the global MDI market are BASF, Bayer, Huntsman, Kumho Mitsui and Yantai Wanhua [4]. The global market for polyurethanes was estimated to be 13,650 kilotons in 2010 and was expected to reach 17,946 kilotons by 2016 [5]. All these data suggest a continuous growth in the amount of the side product HCl. In the industry HCl is used as raw material for the production of ethylene dichloride (EDC) by the oxychlorination of ethylene. However in the EDC process only a small amount of HCl is consumed, compared to the overall produced "side product HCl". In addition, neither the neutralization by alkali nor the sale of hydrochloric acid is profitable. Therefore, efficient technologies which enable the recycling of the surplus HCl into Cl_2 are highly required. The heterogeneously catalytic oxidation of HCl to Cl_2 (Deacon Process) is such an attractive solution, particularly because of its energy efficiency and environmental friendliness compared to another strategies: HCl electrolysis [6].

2.2 The history of the Deacon Reaction

The Deacon reaction has been described over 140 years ago by chemist Henry Deacon [7, 8]. In the beginning Mn, Fe, and Cu metals were used as catalysts. Then Cu has been determined as the main active element, supported on a pumice surface. Unfortunately, its applications were limited by some general problems, including the rapid deactivation of the catalysts due to the formation of volatile copper-chloride species when the reaction temperature is above 400 °C and severe corrosion issues caused by unreacted HCl and H_2O. Nevertheless, it is worth noting that the Deacon Process was the first applied large-scale catalytic gas-phase reaction.

Arnold et al. [9] reported the thermodynamic properties, which provide the possibility to calculate the equilibrium conversion of HCl at different reaction conditions. As an exothermic reaction (2 HCl + ½ O_2 → Cl_2 + H_2O; $\Delta_r H$ = -59 kJ/mol) the HCl equilibrium conversion will be improved at lower temperatures, but the reaction rate would be decreasing due to the kinetic reason as well. Meanwhile, the excess O_2 in the feed gas leads to higher HCl conversion, whereas the

separation fee between the unreacted feed gas and product will be also foreseeable increased [**Figure 1.2**].

The main issue of the Deacon reaction is the stability of the catalyst because higher reaction temperatures result in the volatilization of the Cu catalyst. Due to this limitation in stability, several modifications for the Deacon process have been explored during the 20th century [**6**].
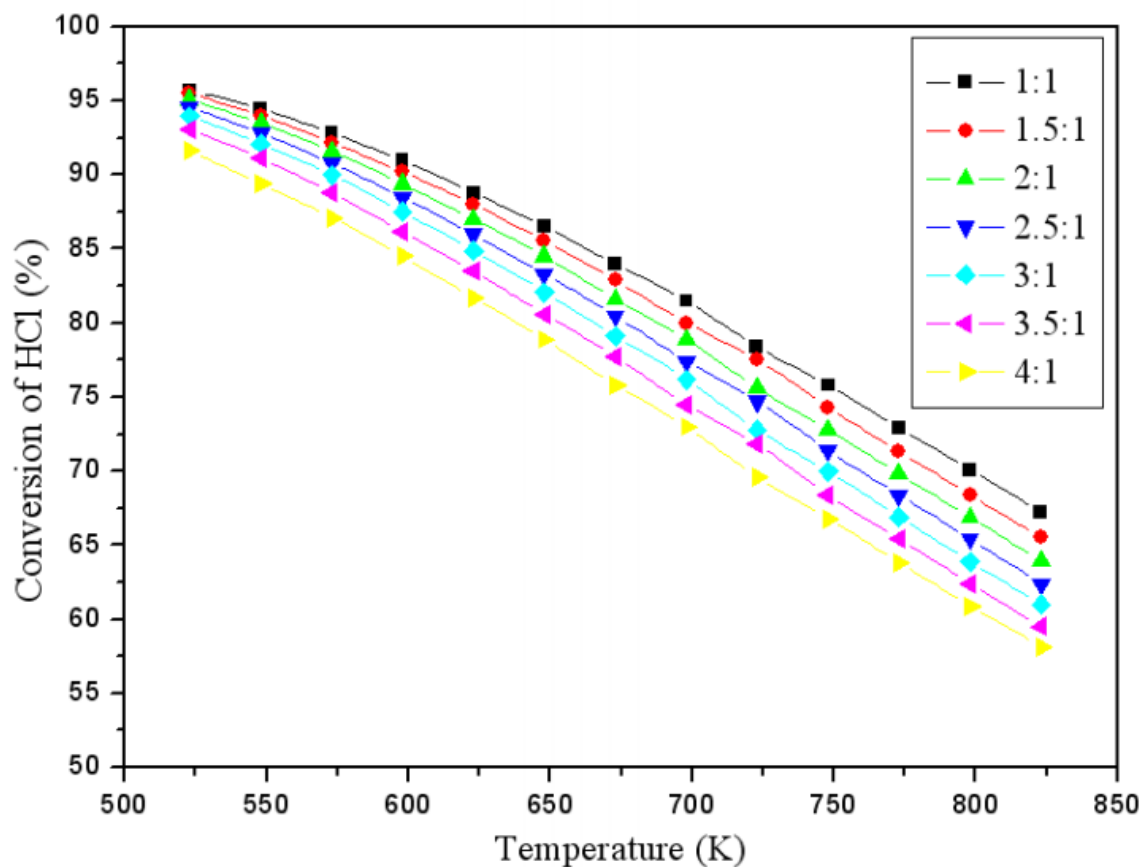
Figure 1.2. Effect of reaction temperature on the equilibrium conversion of HCl with different molar ratio of HCl and O_2 (HCl:O_2=1:1~4:1) in the feed gas [**10**].

Shell-Chlor Process

The Shell-Chlor process was designed by Shell company [**11**]. In the 1960s they used a $CuCl_2$-KCl-$LaCl_3$/SiO_2 catalyst for the HCl oxidation reaction in a fluidized-bed reactor. The reaction temperature was around 365 °C and the HCl conversion was about 80 %. KCl and $CuCl_2$ were equally concentrated in the catalyst with KCl used to inhibit the volatilization of the copper species.

Further a small amount of rare earth metal was added as the second promoter for improving the activity. However, this process was abandoned due to corrosion issues in the plant.

MT-Chlor Process

In the 1980s Mitsui chemicals used Cr_2O_3/SiO_2 as the catalyst in a fluidized-bed reactor in the so-called MT-Chlor process [**12, 13**]. The MT-Chlor process plant a facility in Kyushu. It produced 30 kiloton Cl_2 in the first year and doubled that amount after two years. As a result the stability of the catalyst was significantly improved compared to the Shell-Chlor catalyst. However, the disadvantage of this process is the use of environmentally unfriendly and potentially very toxic materials, i.e.Chromium. In addition, the Cr_2O_3 was also very sensitive to the Fe, which means the materials of the reactor must contain less than 1 % Fe, leading to great cost for the equipment.

Sumitomo Process and Bayer Process

In 1999 Sumitomo Chemical developed RuO_2/TiO_2-rutile as the catalyst with a very high activity (HCl conversion was around 90 %) at low reaction temperature (300 °C) and remarkable stability for more than 15000 h in a fixed-bed reactor [**14, 15**]. In 2002, they licensed a plant with a capacity of 100 kiloton Cl_2 per year in Japan, followed by three additional plants worldwide. Until now no critical problem was reported about this commercial process. Afterwards, Bayer also developed a sort of ruthenium-based catalysts for the Cl_2 recovery by gas phase HCl oxidation [**16, 17**]. Their RuO_2/SnO_2-Al_2O_3 catalyst showed a HCl conversion about 40 % for 7000 h in the temperature range from 280 °C to 380 °C [**18, 19**]. This process has been successfully piloted as well. Seki et al. reported that RuO_2 can be formed as a highly active and remarkably stable film on the surface of the TiO_2-rutile support due to its rutile structure [**16**].

However, ruthenium is still an expensive metal and its market price has been fluctuating dramatically [**Figure 1.3**], thereby limiting the large-scale industrialization. These imperfections has motivated many research groups to investigate alternative and cost-effective catalysts that can also be applied for industrialization. In the last decade many efforts were devoted to develop new catalysts and to understand the mechanism of the HCl oxidation reaction.

Ruthenium
Monthly Average prices between 16 Mar 2002 and 16 Mar 2017
JM Base Price $/0z
Ruthenium average: $141.46
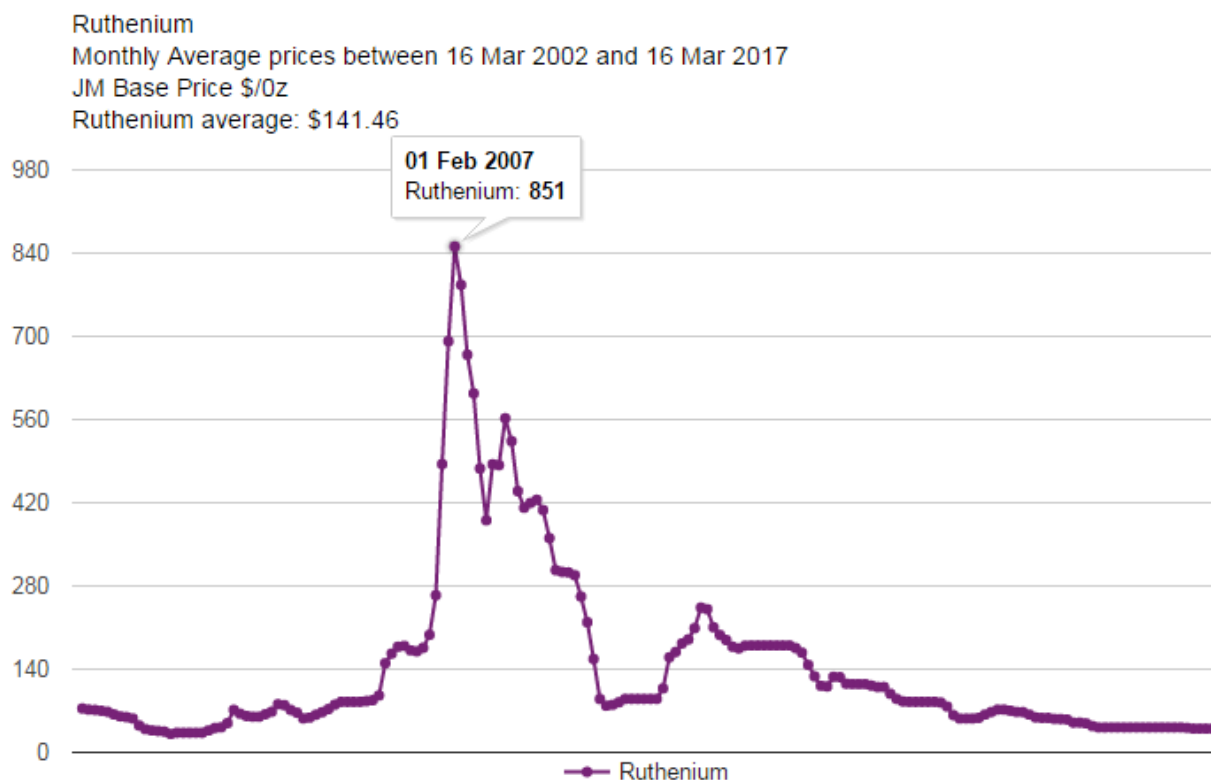
Figure. 1.3. Monthly average prices of ruthenium between 16 Mar 2002 and 16 Mar 2017. Data retrieved from [20].

2.3. The state-of-the-art on catalytic HCl oxidation with Cu-based catalyst

As mentioned before copper-based catalysts were used in the original Deacon process as well as the Shell-Chlor process. Unfortunately, both of them can't be successfully industrialized due to the fast deactivation of catalysts by the volatilization of the copper chlorides and the severe corrosion issues in the plant caused by hydrochloric acid. However, with a much lower price and compared to Ruthenium, many groups kept on investigating on copper-based catalyst.

Hammes et al. investigated the activity and stability of CuTi mixed oxides by doping a third metal. The activity results revealed that $Nb_1Cu_{10}Ti_{89}O_x$ had the highest Cl_2 STY and the kinetic results confirmed that the apparent activation energy decreases by doping of Nb. Furthermore,

only 1 mol% Nb doping can effectively decelerate the loss of Cu with excess O_2, thus improving the catalyst stability. Nevertheless, there is no further application news about this catalyst [21].

Fei and co-workers investigated CuO-CeO_2 mixed oxide catalysts with different molar ratio supported on Y type zeolite. At the reaction condition of 1 bar (T_{bed}=430 °C, m_{cat}=5 g, HCl=80 ml/min and HCl:O_2=1:1) the CuO(12wt%)-CeO_2(13wt%)/Y catalyst showed the highest activity (HCl conversion: 85%) and best stability over 1200 hours without decreasing activity, thus representing a promising industrialized catalyst for the HCl oxidation reaction. After several characterizations (XRD, H_2-TPR, SEM, XPS, Raman, and etc.) they confirmed that the high content of well dispersed CuO species and intensively synergetic effects between the CuO and CeO_2 species are the main contributions for the high activity [22]. Furthermore, some intrinsic kinetic studies were conducted after eliminating the influence of external and internal diffusion to clarify the mechanism of the catalytic reaction. The empirical intrinsic kinetic model has been established on the assumption that the surface reaction (absorbed HCl react with absorbed O_2) is the rate-controlling step. Finally, the experimental results were consistent with the predicted data calculated from the intrinsic kinetic model, being very helpful for the industrial reactor design and scale-up in the future [23]. According to the news reports, they have piloted with one factory in Changzhou with a capability of 1000 ton per year.

Amrute and his co-worker discovered a copper catalyst based on a delafossite structure ($CuAlO_2$) which displayed for over 1000 h under Deacon reaction conditions (N_2:HCl:O_2=5:1:4, T_{bed}=380 °C，W/F^0(HCl) = 8.96g h mol^{-1}). However, this structure was quite unstable and the copper species were easily transformed into $CuCl_2$, CuCl, and CuO during the reaction. Surprisingly, the activity was not decreased by the copper loss of around 40 % caused by forming volatile $CuCl_2$ and CuCl, which is inconsistent with other copper-based catalysts reported before. They explained that the progressive formation of $CuAl_2O_4$, CuO, and copper chloride outstripped the deactivation caused by volatilization of the copper chlorides [24]. Furthermore, they kept working on copper-based delafossite structure ($CuMO_2$) with different metals (M=Cr, Ga, Fe, Mn) by the same preparation method. After testing the catalytic performance with regard to the HCl oxidation, $CuCrO_2$ showed a better activity than $CuAlO_2$ with the activity of the other three catalysts even lower than that of $CuAlO_2$. The XRD results of all used catalysts revealed an interesting behaviour: for $CuCrO_2$ no bulk chlorination after the reaction and even in pure HCl for several hours has not been observed. However, for the other four catalysts bulk chlorination occurred during the reaction. It suggested

that this discovery of $CuCrO_2$ catalyst can solve the problems of the copper loss because of its unique delafossite structure. A 100 hours stability experiment was also operated successfully. In order to further improve the activity, $CuCrO_2$ (70 wt%)-CeO_2 (30 wt%) composites were prepared by the mechanochemical activation of $CuCrO_2$ and CeO_2 powders materials. This material exhibits a four times higher activity than each single phase and presents a feasible alternative to ruthenium-based catalyst for the Cl_2 recycling process. Unfortunately, there are no followed-up reports about this application or a pilot plant of this catalyst [25].

Feng and co-workers used a $CuCl_2$-KCl-$LaCl_3$/γ-Al_2O_3 catalyst with $CuCl_2$ as the active component, KCl and $LaCl_3$ as promoters and γ-Al_2O_3 as supporting material. According to the results the best weight ratio of $CuCl_2$, KCl and $LaCl_3$ was determined to be 3:1:2. The HCl conversion could reach about 80 % under the reaction condition 0.1 MPa, T_{bed}=340 °C, GHSV of 450 L/(kgcat·h), and HCl/O_2 = 2:1. Afterwards, a long-term stability of the best active catalyst was investigated and a remarkable stability for over 9600 h was observed without losing any activity. Consequently, this catalyst has already been successfully implemented in a pilot production with 1000 t/year Cl_2 in Shanghai Chlor-Alkali Chemical Company for 2 years. Now, they are building the industrialization setup with a capability of 100 kton/year Cl_2 in Jinshan District in Shanghai. To deeply understand the catalyst, several characterization technics were applied thus confirming that the KCl can promote the reduction of Cu^{2+} to Cu^+ while $LaCl_3$ significantly reduces the reaction temperature for oxidizing $CuCl_2$ to CuO and therefore producing chlorine [26, 27]. However, the reaction mechanism which is significant for the further improvement of the catalyst and optimization of large-scale industrialization application had not been investigated yet.

2.4. The state-of-the-art on catalytic HCl oxidation with Ce-based catalyst

2.4.1 Pure CeO$_2$ catalyst
Pure CeO$_2$ catalyst applied in Deacon Reaction

CeO_2 has attracted the researchers' interest in view of its wide application in a variety of catalytic reactions [28-34]. In these reactions it had been employed both as catalyst and supporter because of its excellent redox properties and high oxygen storage capacity (OSC). For the same reason CeO_2 had also been claimed as a potentially suitable catalyst for HCl oxidation at high

temperature in some patents [35, 36]. Amrute and his co-worker systematically studied CeO_2 powders by varying their properties, i.e. calcination temperature, surface area and OSC values with regard to the HCl oxidation at different reaction conditions. The results of catalytic performance tests illustrated that the activity is related to the oxygen vacancies and bulk chlorination could be suppressed in O_2-rich feeds. As reported in their kinetic study the reaction order on oxygen was calculated as 0.5, suggesting a positive effect of the oxygen pressure. Through the characterization and DFT simulations the mechanism over CeO_2 catalyst for the HCl oxidation reaction was further proposed. The bulk chlorination took place under HCl-rich condition while the bulk chloride phase disappeared when the catalyst was exposed to O_2-rich conditions. Under the reaction condition of $O_2/HCl > 0.75$ the catalysts were bulk stable, whereas, surface chlorine/chloride was also detectable by XPS technique. DFT simulations showed that Cl activation from vacancy positions to surface Ce atoms is the most energy-demanding step, although the re-oxidation step is the rate-determined step due to the oxygen-chlorine competition for the available active site [37].

Meanwhile Farra et al. used in-situ techniques to investigate the correlation between Cl coverage and catalytic activity over CeO_2 catalyst for HCl oxidation. Based on the in-situ Prompt Gamma Activation Analysis (PGAA) they conclude that the chlorination rate of CeO_2 during the reaction is not influenced by the pre-chlorination degree. The chlorination degree would increase at HCl-rich feed condition. Contrarily the de-chlorination process is dominated under the oxygen-rich feed conditions where bulk $CeCl_3$ is transformed back to CeO_2. Afterwards the surface coverage studies showed that increasing either the ratio of O_2 to HCl or the temperature will remove the surface Cl and increase the surface OH concentration, accompanied by enhancing the reactivity at the same time. Additionally the experiment with pure Cl_2 into the probe mixture feed gas confirmed that the Cl_2 had no effect on the surface Cl coverage except the strong inhibition of the reaction rate during the reaction [38]. In order to clarify how the surface acid/base properties of the CeO_2 varied during HCl oxidation, several kinds of characterizations such as probe molecule (CO_2, NH_3 and CO) adsorption, Micro-calorimetry, in-situ FTIR, TPD and DFT calculations have been applied for CeO_2 in fresh and post-reaction states. Combining both the experiments and calculations, Farra et al. concluded that the initial surface basicity of CeO_2 has been removed during the reaction, thus the surface became more acidic upon reaction. This phenomenon could be explained by the replacement of surface lattice O with Cl species and that the formed OH groups were rather acidic naturally. They also confirmed a linear correlation of OH concentration with the reactivity when

T or pO_2 is varied. However, a converse trend was observed when pHCl is changed [**39**]. As an alternative for the active surface, i.e. chlorinated CeO_2, a bulk oxychloride phase, namely CeOCl, was also considered as a potential catalyst for the HCl oxidation reaction. Synthesized CeOCl was tested under different feed compositions. The results showed that CeOCl is not stable either in harsh condition (oxygen-lean) or in mild condition (oxygen-rich). Excess oxygen feeds completely transformed CeOCl into CeO_2 during the reaction, indicating that the bulk CeO_2 plays a significant role in the HCl oxidation [**40**].

Kanzler et al. investigated the stability of CeO_2 nano-fibers under HCl oxidation reaction. The reaction was measured for 60 hours at the so-called 'mild' (Ar:HCl:O_2 = 7:1:2) and 'harsh' (Ar:HCl:O_2 = 6:2:2) condition, respectively. Afterwards BET, SEM and XRD were used to characterize the changes of physicochemical properties and morphology between the fresh and post-reaction samples. At the harsh reaction conditions the well-defined fibers were destroyed completely and new crystal phase of $CeCl_3$ was formed [**Figure 1.4C**]. Nevertheless the morphology of the fibers did not change and no crystal phase of $CeCl_3$ was detectable by the XRD after the mild condition [**Figure 1.4B**]. These visible morphological changes directly show how the unstable catalyst looks like after HCl oxidation [**41**].
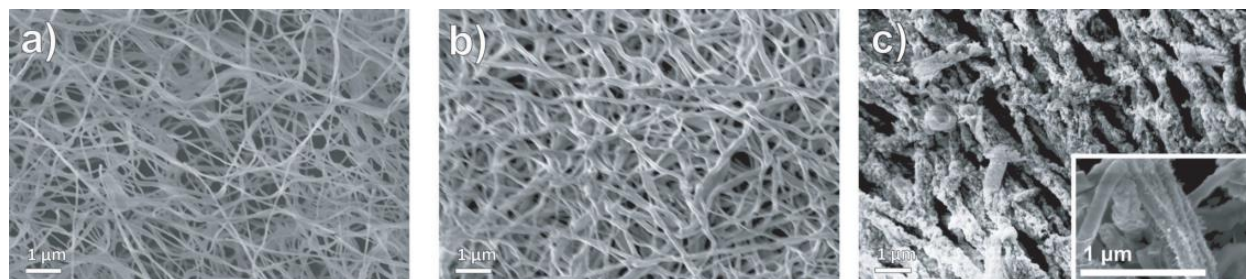
Figure 1.4. SEM of different samples. a) as-prepared CeO_2 fibers. b) CeO_2 fibers after 60 h of mild condition. c) CeO_2 fibers after 60 h of harsh condition [**41**].

Investigation of CeO₂ nanoparticles with different morphologies

Over the last decade CeO_2 nanoparticles with well-defined morphologies (nano-rods, nano-cubes and nano-octahedrons) exposing preferentially (110), (100), and (111) facets have attracted much attention [**42-46**]. These different facet orientation could influence the catalytic activity as the active component or the carrier during the reaction. Further people can investigate the reaction on the atomic level to get a better insight into the reaction. The shape-controlled CeO_2 particles

were used to investigate structure sensitivity of various catalytic reactions (VOC oxidation, Water-Gas shift reaction, CO oxidation, Soot combustion, and some other oxidizing reaction) [**47-61**].

Volatile Organic Compounds (VOC) are considered as one of the main pollutants, that have always been hazardous to atmospheric environment and have negative effects on indoor air quality, thus being greatly harmful to public health. Zhang et al. studied the dichloromethane oxidation reaction depending on different morphologies of CeO_2 nanoparticles. The nano-rods showed the best performance, which was attributed to its high surface area, abundant oxygen vacancies and increased amount of adsorbed active oxygen species during the reaction [**48**].

Research in the field of low-temperature water gas shift reaction (WGS) has attracted much attention due to its potential in the production of clean hydrogen for fuel cell applications. Si et al. synthesized an Au-CeO_2 catalyst by depositing Au on the different facets of nano-rods, nano-cubes, and nano-polyhedra in a two-step process. These catalysts were used in the Water-Gas shift reaction. It was shown that the shape of the catalyst, i.e. its crystal planes, has a strong effect on the activity. The CeO_2 nano-rods enclosed by (110) and (100) facets were most active for gold activation and stabilization. They concluded that the lowest formation energy of anion vacancies in the (110) facet for nano-rods can contribute to more oxygen vacancies and higher lattice strain, thereby enhancing the activity [**49**].

Another catalytic reaction, the dimethyl carbonate synthesis from CO_2 and methanol, was used to study the effect of specific facets on the activity of shape-controlled CeO_2 by Wang et al. The results showed that the spindle-like CeO_2 exhibit the highest DMC yield with the key factors determined to be exposed active (111) facets and a large amount of acid-basic sites [**51**]. Murciano et al. used shape-controlled CeO_2 nano-particles for the total oxidation of polycyclic aromatic hydrocarbons. The results showed that nano-rods are most active followed by nano-cubes and finally the nanoparticles, suggesting that (110) and (100) facets with the higher oxygen storage capacity are more active than the (111) facets [**53**].

Hu et al. studied the effect of the shape-selective oriented CeO_2 on the catalytic properties of Pd/CeO_2 for both CO oxidation and propane oxidation. Interestingly, the Pd/CeO_2(nano-rods) displayed the best performance for CO oxidation, whereas Pd/CeO_2 (nano-octahedrons) represented the most active catalyst for propane oxidation. These results indicate that different facets contribute the different interactions of Pd-O-Ce at the interface, which clearly elucidates the strong correlation between morphology and reactivity [**54**].

Soot is one of the main pollutants emitted by diesel engines, which contain NO_x, CO, and unburned hydrocarbons. Aneggi et al. investigated the shape-dependent activity of CeO_2 for soot combustion. The results confirmed that nano-cubes with predominantly CeO_2(100) facets displayed higher activity than polycrystalline CeO_2 with predominantly (111) facets [**57**].

Inverse results were found for the hydrogenation of C_2H_2 from Vilé and his co-workers. They compared the effect of (100) facets (predominantly exposed by nano-cubes) with the (111) facets (mainly in normal nano-particles) on their performance for C_2H_2 hydrogenation and CO oxidation. Due to the different oxygen vacancy chemistry and defect sites on each facet, the sample with (100) plane showed a higher oxidation activity than that with (111) plane for CO oxidation, while the (111) plane dominated in the hydrogenation reaction. The reason for the inverse results is that hydrogenation is opposite to the oxidation and benefitted over the low-vacancy surface, suggesting the key role of oxygen on the stabilization of reactive intermediates [**62**].

All these literature confirmed a strong correlation between the facets orientation and catalytic performance under various reaction. The CeO_2 powder have been extensively investigated in HCl oxidation, however, the correlation between the specific facets and catalytic performance (activity and stability) is still elusive. In order to clarify this point, we employed shape-controlled CeO_2 nano-particles (namely, cubes, rods, and octahedrons), exposing (100), (110), and (111) facets, for HCl oxidation reaction, respectively. These results are presented in **Chapter 3.1** and **Chapter 3.2**.

2.4.2 Doped CeO$_2$ catalyst

Application of rare earth metal doped CeO$_2$ catalyst

In spite of the wide application of pure CeO_2 there are still some obstacles such as comparatively low catalytic activity and poor thermal stability during some reactions. In order to solve these problems and make further improvement of the CeO_2 based catalysts, people have made much effort and found doping by a second metal is a feasible strategy [**62**]. The rare-earth metals (such as La, Pr, and Sm) as well as Zr are often used as dopants. Krishna et al. investigated the performance of CeO_2 catalysts modified by rare-earth metals for soot oxidation and concluded that the La and Pr doped CeO_2 catalysts show much higher activity than Sm and Y doped and pure CeO_2 catalysts. The enhanced activity is related to an increased surface area in the case of $CeLaO_x$, and to better redox properties in the case of $CePrO_x$. This could be elucidated by the inhibition of the grain growth of CeO_2 under high temperature by doping La^{3+} or $Pr^{3+/4+}$ [**63-65**]. The

improvement of thermal stability of CeO_2-based catalysts by doping La has been widely investigated in a three-way catalyst. Wang et al. reported that the Ceria-Zirconia solid solution modified by La had larger surface area, better thermal stability and higher oxygen storage capacity than the unmodified Ceria-Zirconia solid solution, due to the lattice distortion after doping. In addition La doped fresh samples favored the conversion of NO and the aged samples exhibited higher catalytic activity for all the target pollutants [66, 67]. Meanwhile CeO_2 doped by Sm was also applied for various catalytic reactions [68-74]. Mandal et al. reported that CeO_2-based nano-crystalline frameworks with high concentration of Ce^{3+} and high surface area could be achieved by doping with Sm. Several characterizations were employed revealing that Sm^{3+} doping increased the lattice volume, the mesoporous volume and induced defects on the surface. The H_2-TPR measurements revealed the reduction temperature of bulk CeO_2 shifted to a very low region after doping. The evident change of the reduction properties suggested that the oxygen mobility within doped CeO_2 is enhanced, alongside a higher oxygen diffusibility at lower temperatures ($<$ 300 °C). This promoted reducibility is suggested to be very helpful in the auto-catalytic cycle [68].

Konsolakis et al. investigated the performance of Cu supported on the $Ce_{1-x}Sm_xO_\gamma$ for Volatile organic compound (VOC) oxidation. Unlike other researches this study revealed the opposite effect by Sm doping, indicating a detrimental impact on the VOC oxidation according to Sm content, the more the Sm doped, the worse the catalytic activity. The H_2-TPR results showed that a higher concentration of Sm led to a higher reduction temperature, indicative for the weaker reduction of catalysts. The reason is that the reducible Ce^{4+} was replaced by un-reducible Sm^{3+}, thereby decreasing the reducibility of the whole catalyst material. Moreover these results also illustrate that reducibility is beneficial for VOC oxidation [72].

Applications of Zr doped CeO_2 catalyst

Besides the doping of rare earth metals, CeO_2-ZrO_2 mixed oxides also drew attentions to investigate their physiochemical properties, catalytic activity, and stability for various reactions. First of all, the equilibrium phase diagram of the CeO_2-ZrO_2 system [**Figure 1.5**] has been studied by many researchers [75-80]. Based on these results, we could conclude that the phase of the mixed oxides is dependent on different composition range in $Ce_xZr_{1-x}O_2$ and the most popular phases were summarized below [**Table 1**]. It was reported several times that the doping of trivalent metal ions will not enhance the oxygen storage capacity, whereas the quadrivalent metal ions (such as

Zr^{4+}) can improve the OSC [81-84]. Madier et al. used $^{18}O/^{16}O$ isotope exchange measurements to investigate the oxygen mobility in Ce-based materials, confirming that mixed oxides react more quickly than pure CeO_2. Also the inclusion of Zr into the CeO_2 lattice could markedly improve the thermal stability, with the mixed oxides still maintaining a relatively high surface area after the calcination at 900 °C [81]. The well-known application of $Ce_xZr_{1-x}O_2$ is regarded as the promoter in the automotive TWCs (Three Way Catalysts) [85-88]. Because the TWCs are requested to be exposed to extremely high thermal high temperature (normally > 1000 °C) for longer time periods, a high thermal stability of catalysts is indispensable. Otherwise the 'active oxygen' which is essential for the contact between the noble metal and the CeO_2-based promoter will be lost during the sintering process [88].
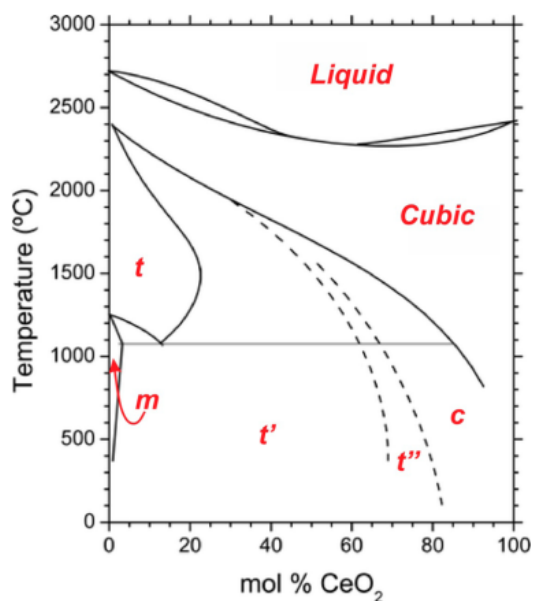

Figure 1.5. Experimental equilibrium phase diagram of the CeO_2-ZrO_2 system. Solid lines represent the stable phase-boundaries and dashed lines correspond to the metastable phase-boundaries [76].

Table 1. Most Metastable, Bulk Homogeneous Phases Identified for $Ce_xZr_{1-x}O_2$ Materials.

Composition	Crystal system and phases	Space group	Unit-cell parameters
$0.90 \leq x \leq 1$	cubic	Fm3m	c/a=1
$0.65 \leq x < 0.90$	Tetragonal (t″)	P42/nmc	c/a=1
$0.20 \leq x < 0.65$	tetragonal (t′)	P42/nmc	c/a > 1
$0.12 \leq x < 0.20$	tetragonal (t)	P42/nmc	c/a > 1
$0 \leq x < 0.12$	monoclinic (m)	P21/c	$a_m \neq b_m \neq c_m, \beta > 90°$
$x=0.5, Ce_2Zr_2O_{7+y}$	pyrochlore	Fd3m	c/a = 1
$x = 0.5, Ce_2Zr_2O_8$	phase κ (cubic)	P213	a = 1.05270 nm
$x = 0.5, Ce_2Zr_2O_8$	phase t*(tetragonal)	P42/nmc	c/a > 1

In addition to the TWCs $Ce_xZr_{1-x}O_2$ are widely used in other reactions, such as Soot Combustion, Oxidation of VOC, Water-Gas Shift Reaction and Steam Reforming. Many researchers investigated the Ce-Zr mixed oxide, in order to replace pure CeO_2 as the catalyst for soot combustion [89-92]. Atribak et al. prepared Ce-Zr mixed oxides with different Ce:Zr ratios under various NO_x/O_2 gas compositions. Among these mixed oxide catalysts $Ce_{0.76}Zr_{0.24}O_2$ has shown the best activity. Meanwhile $Ce_{0.76}Zr_{0.24}O_2$ exhibited high thermal stability at typical reaction temperatures of 1000 °C where the pure CeO_2 is gradually deactivated. Based on the results of characterization (XRD, H_2-TPR, BET) they found the activity is mainly dependent on the surface area and the crystallite size. Additionally other properties as the redox behavior and lattice mobility of O also affect the catalytic activity [90].

Aneggi et al. investigated the effect of specific crystal planes exposed by CeO_2 and Ce-Zr mixed oxides in soot combustion experiments. It is demonstrated that the higher calcination temperature (1000 °C) facilitates the formation of these more active facets ((100) and (110)) than the less active but more stable (111) oriented facets. This preferential exposed facets after calcination is also highly dependent on the amount of Ce, being more evident with pure ceria than with ceria-zirconia. However, at lower calcination temperature (< 500 °C), the fraction of reactive planes (i.e. (110) and (100)) in Ce-Zr is higher than in pure CeO_2. This could be an explanation for the higher activity of Ce-Zr mixed oxides in various reactions. Nevertheless the role of the redox properties of Ce and Ce-Zr in the mechanism of soot oxidation are still not fully understood [91].

Ce-Zr mixed oxides have been applied in various VOCs' combustion investigations [**93-96**]. Bozo and his co-workers prepared a CeO_2-ZrO_2 solid solution by a precipitation method, and investigated the catalytic activity via methane combustion. A $Ce_{0.67}Zr_{0.33}O_2$ solid solution aged at 1000 °C displayed the best thermal stability and catalytic activity and was selected as a support for active phase. Afterwards, $Pd/Ce_{0.67}Zr_{0.33}O_2$ and Pt/Al_2O_3, for comparison, were prepared and measured for the catalytic activity of soot combustion. The results showed that the fresh $Pd/Ce_{0.67}Zr_{0.33}O_2$ catalyst was much more active than the corresponding Pt/Al_2O_3 catalyst, although a deactivation on stream was observed in the 200-500 °C temperature range. If the catalyst was aged at 1000 °C, the thermal stability of the $Ce_{0.67}Zr_{0.33}O_2$ is preserved, whereas the activity is similar to that of an aged Pt/Al_2O_3 catalyst. The same phenomenon also happened when the Pd was replaced by Mn. Therefore Bozo et al. concluded that the CeO_2-ZrO_2 solid solution is not suitable for methane combustion since the application temperature is above 1000 °C [**93**].

Rivas et al. investigated the catalytic performance on the combustion of single and chlorinated VOC/toluene mixtures over a series of $Ce_xZr_{1-x}O_2$ oxides. The incorporation of Zr^{4+} ions into the CeO_2 lattice noticeably lowers the reaction temperature in the combustion of the chlorinated feeds. It is generally stated that toluene is more prone to get completely oxidized by oxygen than chlorinated VOC. However, the chlorinated VOC/toluene mixtures resulted in significant changes in both activity and selectivity compare to the pure chlorinated VOC or toluene. Competitive adsorption presumably plays a key role for the activity, but no species could dominate the adsorption site which can be completely removed by increasing the reaction temperature. It seemed that surface acidity and accessible lattice oxygen control the catalytic performance for chlorinated compounds, while the combustion of toluene was essentially controlled by surface oxygen species. Noticeably these catalysts possess a considerable potential for VOC removal combined with an acceptable stability during the combustion process [**95**].

Gutierrez-Ortiz investigated the adsorption of different volatile organic compound (VOC) on Ce-Zr mixed oxides by Inverse Gas Chromatography (IGC). These chromatography data, combining with other physicochemical properties (surface area, oxygen storage capacity, surface acidity, and reducibility), were correlated to the reactivity and selectivity. It is indicated that the adsorption capacity on the oxide surfaces plays an important role on the activity for chlorinated VOC. Also the selectivity towards different oxidation products depend on both: the oxygen storage

capacity (OSC) and the specific interaction of the chlorinated compounds and the surface of the catalysts [96].

CeO$_2$-ZrO$_2$ based materials are used for water gas shift reaction (WGS) due to their ability to limit the catalyst deactivation by carbonate deposition during start-stop operation [97-102]. Kalamaras et al. synthesized a series of y wt% yPt/Ce$_x$Zr$_{1-x}$O$_2$ catalysts (y=0.1, 0.5 and 1.2; x=0.3, 0.5 and 0.7) and investigated the effect of Zr doping on physicochemical properties and catalytic performance for the WGS reaction. Based on the results they concluded that the introduction of Zr^{4+} into the ceria lattice would decrease the Ce$^{4+}\rightarrow$Ce^{3+} reduction energy, thus directly influencing the catalytic activity. The structure of the active intermediates (C-contained) formed during the WGS also changed due to the doping of Zr^{4+}. Even the concentration of active intermediates (C-contained and H-contained) were found to be strongly dependent on the reaction temperature, support chemical composition (Ce/Zr atom ratio) and Pt particle size [98].

Steam methane reforming (SMR) is a widely applied technology to manufacture hydrogen or synthesis gas (syngas). The most explored system is based on Ce-Zr mixed oxides due to their outstanding redox properties [103-111]. Roh et al. prepared Ni-Ce$_{(1-x)}$Zr$_x$O$_2$ catalysts by the co-precipitation method and studied their catalytic performance on the SRM reaction under severe reaction conditions (GHSV $>$ 150000 h^{-1}). Through the optimization of the CeO$_2$/ZrO$_2$ ratios, Ni-Ce$_{0.8}$Zr$_{0.2}$O$_2$ was found to exhibit the highest CH$_4$ conversion as well as stability. The extraordinary catalytic performance was mainly related to the synergic effect of Ce$_{0.8}$Zr$_{0.2}$O$_2$ solid solution, high Ni dispersion, high thermal stability and high oxygen storage capacity [106]. Au/Ce$_{(1-x)}$Zr$_x$O$_2$ catalysts were employed for oxidative steam reforming of methanol in the temperature range of 200-400 °C. The initial activity was efficiently promoted by doping 25 mol% Zr^{4+} into the CeO$_2$ lattice to form a solid solution, which also contributes to high stability and less coke formation. However, increasing the support calcination temperature to more than 400 °C would cause the simultaneous agglomeration of CeO$_2$ and segregation of ZrO$_2$, thus leading to a reduced activity [108].

Doped CeO₂ catalysts applied in Deacon Reaction

As mentioned previously bulk CeO_2 had been largely investigated as a promising catalyst for the Deacon Reaction. In order to scale up the CeO_2 based catalysts system, several strategies were made for further improvement of activity and stability [**112-116**]. Farra and co-workers investigated trivalent (La, Sm, Gd, and Y) and tetravalent (Hf, Zr, and Ti) metals as dopants for CeO_2 to enhance the catalytic performance in the HCl oxidation. The catalysts were test under 'extremely mild condition' (O_2:HCl = 9:1) at 430 °C. The results revealed a promoting effect on the activity and stability after doping Zr and Hf, whereas all the trivalent dopants were detrimental. For the Hf- and Zr-doped catalysts a 10 % Hf and 20 % Zr doping has shown to give the best performance regarding catalytic activity and stability, respectively. At the initial 5 hours all the catalysts exhibited a slight deactivation of around 3-5 % compared to the original reactivity. The oxygen vacancy formation energy followed the order of trivalent＞tetravalent＞undoped under oxidizing condition, suggesting irrelevance with the reactivity. According to DFT calculations only a balanced reduction of both Cl and O vacancy formation energies results in an enhanced reactivity [**112**]. Möller and co-workers prepared CeO_2 nano-fibers with different contents of Gd doping (CGO) by electrospinning and investigated their physicochemical properties, oxygen storage capacity and catalytic performance with regard to the HCl oxidation. The in-depth characterization evidenced that the formed CGO was a solid solution with high surface area and the Gd was randomly distributed within the CeO_2 lattice. Surprisingly, the OSC had a positive correlation with the increasing concentration of the doped tetravalent metal: Gd. However, the activity in the HCl oxidation had the contrary tendency which is in agreement with the work of Farra et al. [**112**]. Additionally Gd doping was not able to stabilize the Ce-based catalysts for the HCl oxidation reaction. It indicated that they are not feasible strategies for increasing of oxygen vacancies for enhancing the catalytic activity on HCl oxidation of CGO catalysts. Nevertheless the combination of various characterization techniques would be very helpful to deeply and accurately understand the correlation between the doping/vacancies onto the oxygen storage capacity and the catalytic performance of CeO_2 [**113**]. Urban et al. synthesized $Zr_{1-x}Ce_xO_2$ (x=0.1~1) nanofibers by electrospinning and measured their catalytic performance (reactivity and stability) for HCl oxidation under 'mild' and 'harsh' condition, respectively. The results indicated that the activity is enhanced when the concentration of Ce is increased from 0 mol% to 30 mol% of the catalysts. For the other $Zr_{1-x}Ce_xO_2$ (x=0.4~1) catalysts, the activity were shown no difference under the same

reaction condition. Meanwhile SEM and XRD measurements of the $Zr_{1-x}Ce_xO_2$ catalyst after HCl oxidation under 'harsh' conditions indicate that 20 mol% Zr can stabilize the CeO_2-based nanofibers by inhibiting the bulk chlorination from the HCl. However it was also observed that the OSC does not regulate the catalytic activity of the Ce-based catalysts [114]. A series of $Ce_xZr_{1-x}O_2$ (x=0, 0.1, 0.3, 0.5, 0.7, 0.9, and 1) mixed oxides were prepared by a soft reactive grinding procedure and were investigated by Fei and co-workers. Several characterization technics were utilized to investigate the correlation between the physicochemical properties and catalytic performances. The results revealed that a small crystalline size of the nano-particles could improve the activity and the oxygen storage capacity (OSC). They observed a positive correlation between the activity and OSC, which is different to the previous research [112-114]. However, the method for the OSC measurement is quite different. Fei et al. used a H_2/Ar mixture for 0.5 h at 600 °C to completely reduce the samples, and then an O_2/He mix feed gas was induced for re-oxidation. This procedure was quite similar to the measurement of another property, namely the Oxygen storage Capacity complete (OSCc). Among all the catalysts they discovered that the $Ce_{0.5}Zr_{0.5}O_2$ with mixed phases (cubic and tetragonal) exhibited the highest OSC and the best catalytic activity for the HCl oxidation reaction. Furthermore kinetic studies of $Ce_{0.5}Zr_{0.5}O_2$ confirmed that the rate-determining step is the desorption of Cl atoms which are bound to the active site, thus competing with the adsorption of O_2/HCl [115]. Instead of the Zr doped CeO_2-based catalysts, ZrO_2 has also been used as a support and investigated by Moser and co-workers. In order to scale up the CeO_2-based catalysts for HCl oxidation reaction, different stable and inert metal oxides (ZrO_2, Al_2O_3, and TiO_2) were utilized as a support material and the concentration of Ce was varied in the range of 3-20 wt%. They found that CeO_2/ZrO_2 showed the best catalytic performance among these catalysts and the most active one being CeO_2/ZrO_2 (9 mol% Ce). This 9 mol% CeO_2/ZrO_2 was run for a long-term stability experiment in a pilot plant. Its remarkable activity and robust stability presented a realistic alternative to RuO_2-based catalysts for industrialization. The kinetic data showed that the apparent activation energy was calculated to be 60 kJ/mol, which is significantly lower than the value of 90 kJ/mol for bulk CeO_2 catalysts. The oxygen reaction order of 0.4 is as similar to bulk CeO_2. Based on the Rietveld refinement results of XRD data, Moser et al. observed the transformation from monoclinic phase to tetragonal phase of ZrO_2 by the CeO_2 impregnation. However, the Zr was incorporated into the CeO_2 lattice can't be undoubtedly evidenced. In situ PGAA allowed people to clarify the correlation between the reaction parameters and the Cl

coverage. The results illustrated that increasing temperature and O_2/HCl ratio reduces the Cl uptake, and concomitantly, higher reactivity, which is similar to pure CeO_2. But the lower apparent activation energy of CeO_2/ZrO_2 indicates that Cl has less significant blocking efficiency at lower temperature compared to pure CeO_2, which can be explained by the electronic modification and strong incorporation within ZrO_2. Based on these results, CeO_2/ZrO_2 is regarded as a cost-effective, eco-friendly, and feasible alternative to the RuO2-based catalysts for the industrialization of the Deacon process. As reported CeO_2/ZrO_2 catalysts have been piloted by Covestro (former Bayer materials) and ETHZ [**116**].

These researches have made valuable contribution over the Ce-based catalysts for chlorine recovery. However, to learn more about the stabilizing effect of Zr^{4+} we need to control the morphology and the exposed facets of single crystalline $Ce_{1-x}Zr_xO_2$ particles such as encountered with nano-rods. Recently, Zr doped CeO_2 with shaped-control morphology nanoparticles attracted many attentions for various reactions [**117-119**]. Naturally, we want to investigate how Zr doping affects the catalytic activity and stability of CeO_2-based nano-rods under even more harsh condition (10% O_2, 20%~30% HCl, and balanced with Ar). In order to clarify this correlation, we prepared the $Ce_{1-x}Zr_xO_2$ nano-rods (x=0, 0.02, 0.05, and 0.2) and measured them in HCl oxidation reaction under various reaction condition. These results are presented in **Chapter 3.3**.

2.5 Reference

1.   http://www.worldchlorine.org/chlorine-chemistry-benefits.

2.   h. w. e. o. t.-c.-u. w.-i.-c.-u.-f. t.-c. tree.aspx.

3.   Y. U. H. Ando, K. Seki, C. Knapp, N. Omoto, M. Kinoshita, *Sumitomo Kagaku*, 2010, **2**, 1-10.

4.   http://www.researchandmarkets.com/research/rtslgd/global_methylene.

5.   http://www.marketsandmarkets.com/PressReleases/mdi-tdi-polyurethane-market.asp.

6.   J. Pérez-Ramírez, C. Mondelli, T. Schmidt, O. F. K. Schlüter, A. Wolf, L. Mleczko and T. Dreier, *Energy & Environmental Science*, 2011, **4**, 4786.

7.   H. Deacon, 1868. **US85370**

8.   H. Deacom, 1871. **US118209**

9.   M. W. M. Hisham and S. W. Benson, *J. Phys. Chem.*, 1995, **99**, 6194-6198.

10.   K. K. Feng, *Doctoral Thesis of East China university of Science and Technology*, 2012.

11.   W. M. H. S. F. WATTIMENA, *Studies in Surface Science and Catalysis*, 1981, **7**, 816-827.

12.   Y. K. H. Itoh, M. Aijoka, S. Takesaka, and M. Katzita, 1989. **US4803065**

13.   Y. K. T. Kiyoura, T. Nagayama, and K. Kanaya., 1989. **US4822589**

14.   H. N. T. Hibi, H. Abekawa, 1999. **US5871707**

15.   K. Seki, *Catal Surv Asia*, 2010, **14**, 168-175.

16.   L. M. A. Wolf, O. F. Schlüter, S. Schubert, 2007. **US20070274897**

17.   J. K. A. Wolf, O. F. Schlüter, L. Mleczko, 2007. **US20070292336**

18.   C. Mondelli, A. P. Amrute, F. Krumeich, T. Schmidt and J. Pérez-Ramírez, *ChemCatChem*, 2011, **3**, 657-660.

19.   A. P. Amrute, C. Mondelli, T. Schmidt, R. Hauert and J. Pérez-Ramírez, *ChemCatChem*, 2013, **5**, 748-756.

20.   http://www.platinum.matthey.com/prices/price-charts.

21.   M. Hammes, H. Soerijanto, R. Schomäcker, M. Valtchev, K. Stöwe and W. F. Maier, *ChemCatChem*, 2014, **6**, 245-254.

22.   Z. Fei, H. Liu, Y. Dai, W. Ji, X. Chen, J. Tang, M. Cui and X. Qiao, *Chemical Engineering Journal*, 2014, **257**, 273-280.

23.   J. Tang, X. Chen, Z. Fei, J. Zhao, M. Cui and X. Qiao, *Industrial & Engineering Chemistry Research*, 2013, **52**, 11897-11903.

24. C. Mondelli, A. P. Amrute, T. Schmidt and J. Perez-Ramirez, *Chemical communications*, 2011, **47**, 7173-7175.

25. A. P. Amrute, G. O. Larrazabal, C. Mondelli and J. Perez-Ramirez, *Angewandte Chemie*, 2013, **52**, 9772-9775.

26. K. Feng, C. Li, Y. Guo, W. Zhan, B. Ma, B. Chen, M. Yuan and G. Lu, *Chinese Journal of Catalysis*, 2014, **35**, 1359-1363.

27. K. Feng, C. Li, Y. Guo, W. Zhan, B. Ma, B. Chen, M. Yuan and G. Lu, *Applied Catalysis B: Environmental*, 2015, **164**, 483-487.

28. Q. Fu, H. Saltsburg and M. Flytzani-Stephanopoulos, *Science*, 2003, **301**, 935-938.

29. J. Kašpar, P. Fornasiero and M. Graziani, *Catalysis Today*, 1999, **50**, 285-298.

30. A. Primo, T. Marino, A. Corma, R. Molinari and H. Garcia, *J Am Chem Soc*, 2011, **133**, 6930-6933.

31. M. Cargnello, J. J. D. Jaén, J. C. H. Garrido, K. Bakhmutsky, T. Montini, J. J. C. Gámez, R. J. Gorte and P. Fornasiero, *Science*, 2012, **337**, 713-717.

32. P. Zhang, H. Lu, Y. Zhou, L. Zhang, Z. Wu, S. Yang, H. Shi, Q. Zhu, Y. Chen and S. Dai, *Nature communications*, 2015, **6**, 8446.

33. X. Yang, S. Kattel, S. D. Senanayake, J. A. Boscoboinik, X. Nie, J. Graciani, J. A. Rodriguez, P. Liu, D. J. Stacchiola and J. G. Chen, *J Am Chem Soc*, 2015, **137**, 10104-10107.

34. M. Scharfe, P. A. Lira-Parada, V. Paunovic, M. Moser, A. P. Amrute and J. Perez-Ramirez, *Angewandte Chemie*, 2016, **55**, 3068-3072.

35. O. F. S. L. Mleczko, S. Schubert, *Assigned to Bayer Material Science*, 2010, **WO2010133313-A1**.

36. S. W. L. G. Lee, I. Sohn, Y.C. Kwon, J. Song, C.-S. Son, *Assigned to Hanwha Chemical Corporation*, 2009, **WO2009035234-A2**.

37. A. P. Amrute, C. Mondelli, M. Moser, G. Novell-Leruth, N. López, D. Rosenthal, R. Farra, M. E. Schuster, D. Teschner, T. Schmidt and J. Pérez-Ramírez, *Journal of Catalysis*, 2012, **286**, 287-297.

38. R. Farra, M. Eichelbaum, R. Schlögl, L. Szentmiklósi, T. Schmidt, A. P. Amrute, C. Mondelli, J. Pérez-Ramírez and D. Teschner, *Journal of Catalysis*, 2013, **297**, 119-127.

39. R. Farra, S. Wrabetz, M. E. Schuster, E. Stotz, N. G. Hamilton, A. P. Amrute, J. Perez-Ramirez, N. Lopez and D. Teschner, *Physical chemistry chemical physics : PCCP*, 2013, **15**, 3454-3465.

40. R. Farra, F. Girgsdies, W. Frandsen, M. Hashagen, R. Schlögl and D. Teschner, *Catalysis Letters*, 2013, **143**, 1012-1017.

41. C. H. Kanzler, S. Urban, K. Zalewska-Wierzbicka, F. Hess, S. F. Rohrlack, C. Wessel, R. Ostermann, J. P. Hofmann, B. M. Smarsly and H. Over, *ChemCatChem*, 2013, **5**, 2621-2626.

42. H.-X. Mai, L.-D. Sun, Y.-W. Zhang, R. Si, W. Feng, H.-P. Zhang, H.-C. Liu and C.-H. Yan, *The Journal of Physical Chemistry B*, 2005, **109**, 24380-24385.

43. C. Sun, H. Li and L. Chen, *Energy & Environmental Science*, 2012, **5**, 8475-8505.

44. M. Hirano and E. Kato, *Journal of the American Ceramic Society*, 1999, **82**, 786-788.

45. Z. Wu, M. Li, J. Howe, H. M. Meyer, 3rd and S. H. Overbury, *Langmuir : the ACS journal of surfaces and colloids*, 2010, **26**, 16595-16606.

46. Y. Lin, Z. Wu, J. Wen, K. R. Poeppelmeier and L. D. Marks, *Nano letters*, 2014, **14**, 191-196.

47. X. Zhang, Z. Pei, H. Lu and H. Huang, *RSC Advances*, 2016, **6**, 84209-84215.

48. R. Si and M. Flytzani-Stephanopoulos, *Angewandte Chemie*, 2008, **47**, 2884-2887.

49. L. Wang, Y. Wang, Y. Zhang, Y. Yu, H. He, X. Qin and B. Wang, *Catal. Sci. Technol.*, 2016, **6**, 4840-4848.

50. S. Wang, L. Zhao, W. Wang, Y. Zhao, G. Zhang, X. Ma and J. Gong, *Nanoscale*, 2013, **5**, 5582-5588.

51. Q. Dai, H. Huang, Y. Zhu, W. Deng, S. Bai, X. Wang and G. Lu, *Applied Catalysis B: Environmental*, 2012, **117-118**, 360-368.

52. L. Torrente-Murciano, A. Gilbank, B. Puertolas, T. Garcia, B. Solsona and D. Chadwick, *Applied Catalysis B: Environmental*, 2013, **132-133**, 116-122.

53. T. S. Sreeremya, A. Krishnan, K. C. Remani, K. R. Patil, D. F. Brougham and S. Ghosh, *ACS applied materials & interfaces*, 2015, **7**, 8545-8555.

54. Z. Hu, X. Liu, D. Meng, Y. Guo, Y. Guo and G. Lu, *ACS Catalysis*, 2016, **6**, 2265-2279.

55. S. Agarwal, L. Lefferts, B. L. Mojet, D. A. J. M. Ligthart, E. J. M. Hensen, D. R. G. Mitchell, W. J. Erasmus, B. G. Anderson, E. J. Olivier, J. H. Neethling and A. K. Datye, *ChemSusChem*, 2013, **6**, 1898-1906.

56. T. Naganuma, *Nano Research*, 2016, **10**, 199-217.

57. E. Aneggi, D. Wiater, C. de Leitenburg, J. Llorca and A. Trovarelli, *ACS Catalysis*, 2014, **4**, 172-181.

58. C. Pan, D. Zhang, L. Shi and J. Fang, *European Journal of Inorganic Chemistry*, 2008, **2008**, 2429-2436.

59. W. Zhang, X. Niu, L. Chen, F. Yuan and Y. Zhu, *Scientific reports*, 2016, **6**, 29062.

60. D. Zhang, X. Du, L. Shi and R. Gao, *Dalton transactions*, 2012, **41**, 14455-14475.

61. G. Vile, S. Colussi, F. Krumeich, A. Trovarelli and J. Perez-Ramirez, *Angewandte Chemie*, 2014, **53**, 12069-12072.

62. T. Montini, M. Melchionna, M. Monai and P. Fornasiero, *Chemical reviews*, 2016, **116**, 5987-6041.

63. K. Krishna, A. Bueno-López, M. Makkee and J. A. Moulijn, *Applied Catalysis B: Environmental*, 2007, **75**, 189-200.

64. K. Krishna, A. Bueno-López, M. Makkee and J. A. Moulijn, *Applied Catalysis B: Environmental*, 2007, **75**, 201-209.

65. K. Krishna, A. Bueno-López, M. Makkee and J. A. Moulijn, *Applied Catalysis B: Environmental*, 2007, **75**, 210-220.

66. Q. Wang, G. Li, B. Zhao and R. Zhou, *Applied Catalysis B: Environmental*, 2010, **100**, 516-528.

67. Q. Wang, G. Li, B. Zhao, M. Shen and R. Zhou, *Applied Catalysis B: Environmental*, 2010, **101**, 150-159.

68. B. Mandal, A. Mondal, S. S. Ray and A. Kundu, *Dalton transactions*, 2016, **45**, 1679-1692.

69. N. Sutradhar, A. Sinhamahapatra, S. Pahari, M. Jayachandran, B. Subramanian, H. C. Bajaj and A. B. Panda, *The Journal of Physical Chemistry C*, 2011, **115**, 7628-7637.

70. M. Guo, J. Lu, Y. Wu, Y. Wang and M. Luo, *Langmuir : the ACS journal of surfaces and colloids*, 2011, **27**, 3872-3877.

71. A. G. M. Silva, T. S. Rodrigues, A. Dias, H. V. Fajardo, R. F. Gonçalves, M. Godinho and P. A. Robles-Dutenhefner, *Catalysis Science & Technology*, 2014, **4**, 814.

72. M. Konsolakis, S. A. Carabineiro, P. B. Tavares and J. L. Figueiredo, *Journal of hazardous materials*, 2013, **261**, 512-521.

73. A. Rangaswamy, P. Sudarsanam and B. M. Reddy, *Journal of Rare Earths*, 2015, **33**, 1162-1169.

74. S. M. Yang, S. Lee, J. Jian, W. Zhang, P. Lu, Q. Jia, H. Wang, T. W. Noh, S. V. Kalinin and J. L. MacManus-Driscoll, *Nature communications*, 2015, **6**, 8588.

75. M. Yashima, H. Arashi, M. Kakihana and M. Yoshimura, *Journal of the American Ceramic Society*, 1994, **77**, 1067-1071.

76. M. Yashima, *Catalysis Today*, 2015, **253**, 3-19.

77. M. Yashima, T. Hirose, S. Katano, Y. Suzuki, M. Kakihana and M. Yoshimura, *Physical Review B*, 1995, **51**, 8018-8025.

78. S. Torng, K. Miyazawa and T. Sakuma, *Ceramics International*, 1996, **22**, 309-315.

79. M. Yashima, S. Sasaki, Y. Yamaguchi, M. Kakihana, M. Yoshimura and T. Mori, *Applied Physics Letters*, 1998, **72**, 182-184.

80. M. Yashima, *The Journal of Physical Chemistry C*, 2009, **113**, 12658-12662.

81. Y. Madier, C. Descorme, A. M. Le Govic and D. Duprez, *The Journal of Physical Chemistry B*, 1999, **103**, 10999-11006.

82. S. Rossignol, Y. Madier and D. Duprez, *Catalysis Today*, 1999, **50**, 261-270.

83. A. Trovarelli, F. Zamar, J. Llorca, C. d. Leitenburg, G. Dolcetti and J. T. Kiss, *Journal of Catalysis*, 1997, **169**, 490-502.

84. O. L. E. Rohart, S. Deutsch,C. Hédouin,H. Aïmin,F Fajardie,M. Allain, P. Macaudière, *Topics in Catalysis*, 2004, **30**, 417-423.

85. L. Lan, S. Chen, Y. Cao, S. Wang, Q. Wu, Y. Zhou, M. Huang, M. Gong and Y. Chen, *Journal of Molecular Catalysis A: Chemical*, 2015, **410**, 100-109.

86. J. Kašpar, P. Fornasiero and N. Hickey, *Catalysis Today*, 2003, **77**, 419-449.

87. R. Di Monte, P. Fornasiero, J. Kašpar, M. Graziani, J. M. Gatica, S. Bernal and A. Gómez-Herrero, *Chemical communications*, 2000, 2167-2168.

88. J. Kaspar, P. Fornasiero, G. Balducci, R. Di Monte, N. Hickey and V. Sergo, *Inorganica Chimica Acta*, 2003, **349**, 217-226.

89. C. A. Neyertz, E. D. Banús, E. E. Miró and C. A. Querini, *Chemical Engineering Journal*, 2014, **248**, 394-405.

90.   I. Atribak, A. Buenolopez and A. Garciagarcia, *Journal of Catalysis*, 2008, **259**, 123-132.

91.   E. Aneggi, C. de Leitenburg, J. Llorca and A. Trovarelli, *Catalysis Today*, 2012, **197**, 119-126.

92.   L. P. dos Santos Xavier, V. Rico-Pérez, A. M. Hernández-Giménez, D. Lozano-Castelló and A. Bueno-López, *Applied Catalysis B: Environmental*, 2015, **162**, 412-419.

93.   C. Bozo, N. Guilhaume, E. Garbowski and M. Primet, *Catalysis Today*, 2000, **59**, 33-45.

94.   B. de Rivas, J. I. Gutiérrez-Ortiz, R. López-Fonseca and J. R. González-Velasco, *Applied Catalysis A: General*, 2006, **314**, 54-63.

95.   E. Diaz, B. de Rivas, R. Lopez-Fonseca, S. Ordonez and J. I. Gutierrez-Ortiz, *Journal of chromatography. A*, 2006, **1116**, 230-239.

96.   J. I. Gutiérrez-Ortiz, B. de Rivas, R. López-Fonseca and J. R. González-Velasco, *Catalysis Today*, 2005, **107-108**, 933-941.

97.   W. Ruettinger, X. Liu and R. J. Farrauto, *Applied Catalysis B: Environmental*, 2006, **65**, 135-141.

98.   C. M. Kalamaras, D. D. Dionysiou and A. M. Efstathiou, *ACS Catalysis*, 2012, **2**, 2729-2742.

99.   F. Meunier, A. Goguet, C. Hardacre, R. Burch and D. Thompsett, *Journal of Catalysis*, 2007, **252**, 18-22.

100.   D. Tibiletti, A. A. Fonseca, R. Burch, Y. Chen, J. M. Fisher, A. Goguet, C. Hardacre, P. Hu and D. Thompsett, *The Journal of Physical Chemistry B*, 2005, **109**, 22553-22559.

101.   A. A. Fonseca, J. M. Fisher, D. Ozkaya, M. D. Shannon and D. Thompsett, *Topics in Catalysis*, 2007, **44**, 223-235.

102.   A. Goguet, R. Burch, Y. Chen, C. Hardacre, P. Hu, R. W. Joyner, F. C. Meunier, B. S. Mun, D. Thompsett and D. Tibiletti, *The Journal of Physical Chemistry C*, 2007, **111**, 16927-16933.

103.   K. Kusakabe, K.-I. Sotowa, T. Eda and Y. Iwamoto, *Fuel Processing Technology*, 2004, **86**, 319-326.

104.   N. Laosiripojana, D. Chadwick and S. Assabumrungrat, *Chemical Engineering Journal*, 2008, **138**, 264-273.

105.   M. H. Halabi, M. H. J. M. de Croon, J. van der Schaaf, P. D. Cobden and J. C. Schouten, *Applied Catalysis A: General*, 2010, **389**, 68-79.

106. H.-S. Roh, I.-H. Eum and D.-W. Jeong, *Renewable Energy*, 2012, **42**, 212-216.

107. H.-S. Roh, K. Y. Koo and W. L. Yoon, *Catalysis Today*, 2009, **146**, 71-75.

108. C. Pojanavaraphan, W. Nakaranuwattana, A. Luengnaruemitchai and E. Gulari, *Chemical Engineering Journal*, 2014, **240**, 99-108.

109. T. Montini, L. Derogatis, V. Gombac, P. Fornasiero and M. Graziani, *Applied Catalysis B: Environmental*, 2007, **71**, 125-134.

110. A. Birot, F. Epron, C. Descorme and D. Duprez, *Applied Catalysis B: Environmental*, 2008, **79**, 17-25.

111. L. Cao, C. Ni, Z. Yuan and S. Wang, *Catalysis Letters*, 2009, **131**, 474-479.

112. R. Farra, M. García-Melchor, M. Eichelbaum, M. Hashagen, W. Frandsen, J. Allan, F. Girgsdies, L. Szentmiklósi, N. López and D. Teschner, *ACS Catalysis*, 2013, **3**, 2256-2268.

113. M. Möller, S. Urban, P. Cop, T. Weller, R. Ellinghaus, M. Kleine-Boymann, C. Fiedler, J. Sann, J. Janek, L. Chen, P. J. Klar, D. M. Hofmann, J. Philipps, P. Dolcet, S. Gross, H. Over and B. M. Smarsly, *ChemCatChem*, 2015, **7**, 3738-3747.

114. S. Urban, N. Tarabanko, C. H. Kanzler, K. Zalewska-Wierzbicka, R. Ellinghaus, S. F. Rohrlack, L. Chen, P. J. Klar, B. M. Smarsly and H. Over, *Catalysis Letters*, 2013, **143**, 1362-1367.

115. Z. Fei, X. Xie, Y. Dai, H. Liu, X. Chen, J. Tang, M. Cui and X. Qiao, *Industrial & Engineering Chemistry Research*, 2014, **53**, 19438-19445.

116. M. Moser, C. Mondelli, T. Schmidt, F. Girgsdies, M. E. Schuster, R. Farra, L. Szentmiklósi, D. Teschner and J. Pérez-Ramírez, *Applied Catalysis B: Environmental*, 2013, **132-133**, 123-131.

117. A. Chen, Y. Zhou, N. Ta, Y. Li and W. Shen, *Catal. Sci. Technol.*, 2015, **5**, 4184-4192.

118. W. T. Chen, K. B. Chen, M. F. Wang, S. F. Weng, C. S. Lee and M. C. Lin, *Chemical communications*, 2010, **46**, 3286-3288.

119. X. Liu, J. Ding, X. Lin, R. Gao, Z. Li and W.-L. Dai, *Applied Catalysis A: General*, 2015, **503**, 117-123.

3. Results and Discussions (Scientific Publications)

3.1 Publication 1

Shape-Controlled CeO$_2$ Nanoparticles: Stability and Activity in the Catalyzed HCl Oxidation Reaction

Chenwei Li, Yu Sun, Igor Djerdj, Pascal Vöpel, Carl-Christian Sack, Tobias Weller, Joachim Sann, Rüdiger Ellinghaus, Yanglong Guo, Bernd M. Smarsly, Herbert Over

ACS Catalysis

Shape-Controlled CeO$_2$ Nanoparticles: Stability and Activity in the Catalyzed HCl Oxidation Reaction

Chenwei Li,[†,‡] Yu Sun,[†] Igor Djerdj,[§] Pascal Voepel,[‡] Carl-Christian Sack,[‡] Tobias Weller,[‡] Rüdiger Ellinghaus,[‡] Joachim Sann,[‡] Yanglong Guo,[*,†] Bernd M. Smarsly,[*,‡] and Herbert Over[*,‡]

[†]Key Laboratory for Advanced Materials, Research Institute of Industrial Catalysis, School of Chemistry and Molecular Engineering, East China University of Science and Technology, Shanghai 200237, PR China

[‡]Physikalisch-Chemisches Institut, Justus Liebig University, Heinrich-Buff-Ring 17, 35392 Giessen, Germany

[§]Department of Chemistry, J. J. Strossmayer University of Osijek, Ulica cara Hadrijana 8/a, HR-31000 Osijek, Croatia

Ⓢ Supporting Information

ABSTRACT: CeO$_2$ is a promising catalyst for the HCl oxidation (Deacon process) in order to recover Cl$_2$. Employing shape-controlled CeO$_2$ nanoparticles (cubes, octahedrons, rods) with facets of preferential orientations ((100), (111), (110)), we studied the activity and stability under two reaction conditions (harsh: Ar:HCl:O$_2$ = 6:2:2 and mild: Ar:HCl:O$_2$ = 7:1:2). It turns out that both activity and stability are structure-sensitive. In terms of space time yield (STY), the rods are the most active particles, followed by the cubes and finally the octahedrons. This very same trend is reconciled with the complete oxygen storage capacity (OSCc), indicating a correlation between the observed activity STY and the OSCc. The apparent activation energies are about 50 kJ/mol for cubes and rods, while the octahedrons reveal an apparent activation energy of 65 kJ/mol. The reaction order in O$_2$ is positive (0.26−0.32). Under mild reaction conditions, all three morphologies are stable, consistent with corresponding studies of CeO$_2$ powders and CeO$_2$ nanofibers. Under harsh reaction conditions, however, cubes and octahedrons are both instable, forming hydrated CeCl$_3$, while rods are still stable. The present stability and activity experiments in the catalytic HCl oxidation reaction over shape-controlled CeO$_2$ nanoparticles may serve as benchmarks for future ab initio studies of the catalyzed HCl oxidation reaction over well-defined CeO$_2$ surfaces.

KEYWORDS: Deacon process, CeO$_2$, shape controlled particles, structure sensitivity, stability, activity
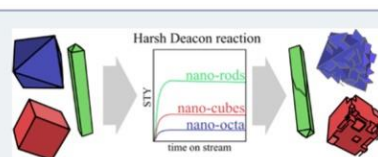
1. INTRODUCTION

The gas-phase oxidation of HCl to Cl$_2$ (Deacon process) constitutes a sustainable way to recycle the byproduct HCl generated, for instance, in the manufacture of polyurethanes and polycarbonates, thereby allowing for closing the overall process cycle.[1,2] The Deacon process is superior to other strategies including HCl electrolysis and neutralization, in terms of energy efficiency and environmental friendliness. However, the Deacon process had faced severe stability problems of the catalyst, so that it had taken about 130 years from its original discovery by Henry Deacon to come up with a commercially viable catalyst.[3] At the end of the millennium, the main driver for searching for new-generation Deacon catalysts was, however, the steady increase in polyurethane and polycarbonate production. Sumitomo Chemical introduced RuO$_2$ supported on rutile TiO$_2$ as an extraordinarily active and stable Deacon catalyst. RuO$_2$ is not only scarce with a high and volatile price, but also RuO$_2$ may face stability problems by forming volatile RuO$_4$ at elevated temperatures that is encountered at "hot-spots" in the fixed-bed reactor during the Deacon process. Therefore, it would be desirable to find an alternative abundant and cost-effective catalyst material from an economical point of view.[2,4,5] A catalytic activity lower than that of RuO$_2$ would be tolerable as long as the catalytic activity of this new material can

be increased by rising the reaction temperature without losing its stability.

Recently, the group of Pérez-Ramírez in collaboration with Covestro (former Bayer MaterialScience) has identified CeO$_2$ as a promising alternative to RuO$_2$.[6,7] A typical reaction temperature using CeO$_2$-based catalysts in the Deacon process is 430 °C, and the activity is indeed substantially lower than that of RuO$_2$-based catalysis being operated at 300 °C. Under harsh reaction conditions (HCl excess), CeO$_2$ powder transforms partly into CeCl$_3$, thereby suppressing the catalytic activity.[6]

In general, particles in powder catalysts expose various facets, predominantly low-index surfaces with low surface energies. To investigate the impact of the facet orientation on the stability and activity of CeO$_2$, here we employ shape-controlled CeO$_2$ nanoparticles (namely, cubes, rods, and octahedrons),[8] exposing preferentially (100), (110), and (111) facets, respectively. These shape-controlled CeO$_2$ particles have been applied to study structure sensitivity of various catalytic reactions both experimentally[9−15] and theoretically.[16] Various

computational studies of the surface energies consistently reported[17−20] an ordering of the stability among these three surfaces: (111)>(110)>(100). However, a recent study from first-principles has shown that the surface energy of the (100) facet is significantly stabilized by entropic effects so that the ordering of surface energies may change at higher temperatures.[21] Assuming highest surface energy for the (100) surface, chemical notion would anticipate also highest catalytic activity for this orientation. A recent study on soot combustion[22] does confirm nanocubes possessing predominantly $CeO_2(100)$ facets display higher activity than polycrystalline CeO_2. The opposite trend was, however, found for the hydrogenation of C_2H_2.[23]

In this paper, we present a study on activity and stability of shape-controlled CeO_2 nanoparticles (rods, cubes, octahedrons) for the corrosive HCl oxidation reaction, employing transmission electron microscopy (TEM), X-ray photoelectron spectroscopy (XPS), and X-ray diffraction (XRD), thereby addressing morphological, compositional, and crystallographic changes, respectively. It turns out that CeO_2 nanorods display the highest stability, although the BET surface area was the highest among the three kinds of particles. In order to separate the catalytic activity (space-time yield, STY) and stability from the impact of the different surface areas of the three materials, the BET surface areas were thoroughly determined by both, nitrogen and krypton physisorption. The normalization with respect to the BET surface area provides the inherent catalytic performance for the three shapes: octahedron (111) > cube (100) > rod (110). As an important parameter, the oxygen storage capacity (OSC) as well as the complete oxygen storage capacity (OSCc) were determined for the three particle morphologies and correlated to the observed activities. We further determined the apparent activation energies and the reaction order in oxygen for the three morphologies.

2. EXPERIMENTAL DETAILS

The shape-controlled CeO_2 particles were synthesized by a previously published hydrothermal method.[8,24] For the preparation of cubes and rods, the Ce-containing solution (0.434 g $Ce(NO_3)_3·6H_2O$ + 2.5 mL of deionized water) was first dropped into a NaOH solution (4.8 g NaOH + 17.5 mL of deionized water) placed in Teflon liner and stirred for 30 min. The Teflon liner was then put inside the autoclave keeping the temperature either at 180 °C (cubes) or at 100 °C (rods) for 24 h. For the preparation of octahedral particles, an aqueous solution of $Ce(NO_3)_3$ (0.217g $Ce(NO_3)_3·6H_2O$ + 2.5 mL of deionized water) was dropped into a solution of 0.0019 g $Na_3PO_4·12H_2O$ + 17.5 mL of deionized water. The hydrothermal reaction took place at 200 °C for 20 h. In all three cases, the precipitates were separated by centrifugation and subsequently washed by deionized water and ethanol several times. Finally, the samples were calcined at 873 K for 6 h in a muffle oven with heating rate of 5 K/min. The calcination temperature of 873 K was chosen to be higher than any temperature occurring in the Deacon reactor so that further temperature-induced sintering of the particles during the Deacon reaction can be excluded.

Transmission electron microscopy (TEM) was performed on a Philipps CM30 instrument operated at 300 kV. Copper mesh grids were used for the sample preparation. High-resolution images were acquired with a JEM-2100 transmission electron microscope operated at 200 kV. The sample was ultrasonically suspended in the ethanol solvent, and one or two droplets of

this slurry were deposited on a copper grid. SEM micrographs were taken by a HREM Merlin (Carl Zeiss MicroImaging GmbH, Göttingen, Germany).

The activity data were normalized to the surface area, measured by N_2 and krypton physisorption (BET) (Quadrasorb evo and Autosorb-iQ; Quantachrome, Boynton Beach, USA) at 77 K.

Structural information on the catalyst is gained by X-ray diffraction (XRD) which is conducted in Θ-2Θ geometry on a Panalytical X'Pert PRO diffractometer with a Cu Kα source (40 kV, 40 mA). Rietveld analysis was carried out by using the FullProf program (Version 2.05).

The concentration of Ce^{3+},Ce^{4+} and Cl in the near-surface region of the particles was quantified by X-ray photoemission spectroscopy (XPS) experiments (PHI VersaProbe II). The photon energy was 1486.6 eV (monochromatized Al $K_α$ line), the X-ray spot size was ∼200 μm with an excitation power of ∼50 W. Charging of the sample was compensated by a flow of electrons with energies of about 1 eV and Ar^+ ions of about 10 eV. The survey spectra were taken with an analyzer pass energy of 93.9 eV and a step size of 0.8 eV while the detail spectra were taken with a pass energy of 23.5 eV and a step size of 0.2 eV. The chamber pressure was ∼10^{-6} Pa during the measurement, and all spectra were taken at room temperature. The data analysis was carried out with CasaXPS Version 2.3.17.

All spectra were energy-corrected by shifting the C 1s hydrocarbon signal to 284.8 eV. For the fitting, we followed the classic approach first suggested by Burroughs et al.[25] and later refined by Romeo et al.[26] with five peaks labeled v, v_0, v', v'' and v''' for the $3d_{5/2}$ and another 5 peaks labeled u, u_0, u', u'', and u''' for the spin−orbit split $3d_{3/2}$. We used Gaussian/Lorentzian peak shapes (GL(30)) to fit the peaks and employed a linear background by splitting the Ce 3d region into 3 sections (v_0 to v'', v''' to u'', and u'''). We constrained the area ratios of the 5/2 and 3/2 species to 3:2. The spin−orbit-splitting of the lines was constrained to a minimum of 18 eV and a maximum of 18.5 eV. In order to have reference data for Ce^{3+} related line positions, we also measured pure Ce_2O_3 as well as $CeCl_3$ reference spectra. (cf. Figure S5)

The catalytic tests of the shape-controlled nanoparticles were conducted in a fixed bed flow reactor. The homemade design of reactor set up[27] comprises the gas supply, the quartz tube reactor, heated by a furnace, and the UV/vis spectrometer for analytic chlorine quantification. The reaction temperature is computer-controlled. The absorbance at a wavelength of $λ_{max}$ = 329 nm (absorption maximum of chlorine) is proportional to the chlorine space time yield (STY) which was routinely counter-calibrated by standard iodometry (KI solution). For the calibration both the concentration of Cl_2 can be time-integrated and then compared to the absorbance integrated over the same time period. Using the Lambert−Beer law, we calibrate the product of the molar absorptivity $ε$ and the path length of the UV beam in the cell d: $εd$. Subsequently with this value we determine the molar concentration from the UV absorbance. STY was derived from the molar concentration c of Cl_2, the volumetric flow rate v, and the mass of the catalyst m_{cat} according to STY = cv/m_{cat}. The flow of gases, supplied by AirLiquide (HCl 4.5, O_2 4.8, and Ar 5.0), was controlled by digital mass flow controllers (MKS Instruments 1179B). Prior to feeding into the reactor, Ar was dried using a water absorption cartridge (ALPHAGAZ purifier H_2O-free, Air-Liquide). The argon balanced reaction feeds contain 20 vol % O_2; based on their HCl content containing 10 vol % and 20 vol
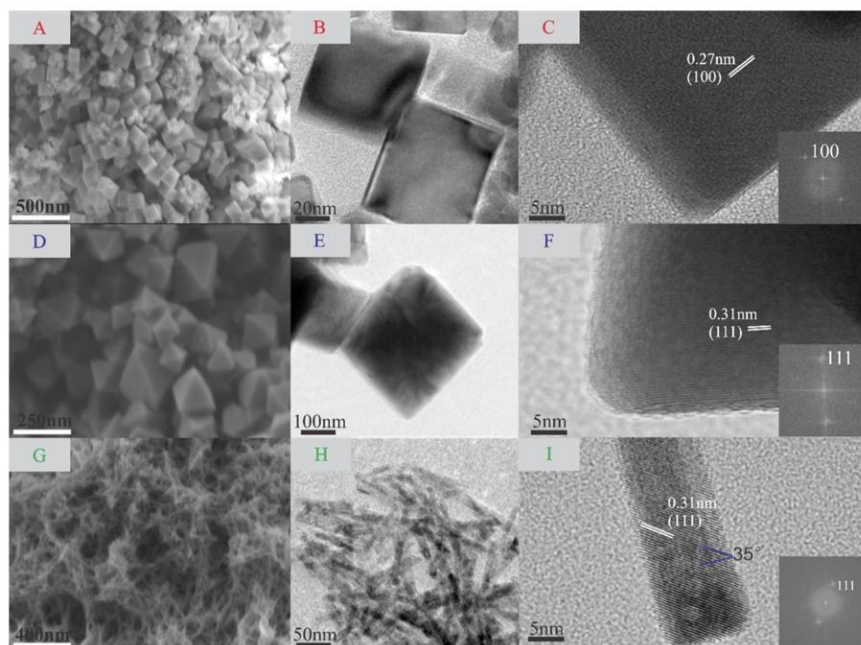
Figure 1. SEM images (A,D,G), TEM images (B,E,H) and high-resolution TEM images (C,F,I) of the as-prepared shape controlled CeO_2 particles: (A+B+C) cubes; (D+E+F) octahedrons; (G+H+I) rods. Inset of (C+F+I): fast Fourier transformation (FFT) pattern of the particle.

% HCl, these reaction feeds are called "mild" and "harsh", respectively. The total volumetric flow rate for the reaction was set to 15 SCCM (mL min^{-1} at standard temperature and pressure). For the catalytic tests, typically 20 mg of ceria material was supported between quartz wool wads in the reactor tube. The furnace was heated to 430 °C with a rate of 10 K/min and held for 1–8 h under the reactant stream. Only after the reaction temperature had been reached in Ar atmosphere, the catalyst was exposed to the O_2 and HCl reaction mixture.

The oxygen storage capacity (OSC) reactor is a stainless steel tube (i.d. 4 mm, length 60 mm) connected to the rest of equipment by stainless steel leads (i.d. 1.6 mm) via Swagelok tube fittings.[28,29] The OSC reactor was heated to 430 °C (at the rate of 10 K/min). Carbon monoxide (Praxair, quality 4.7) was used as the reducing agent. The catalyst sample was dried in static air at 120 °C for 5 h, and 25 mg of it was loaded into the reactor, supported between quartz wool wads. To determine the plain oxygen storage capacity (OSC), i.e. the most active oxygen species in a sample, the stream selector was switched to CO for 2 s (0.067 mL STP of CO), then pure Ar was fed for 80 s, and the stream selector was switched to O_2 for 2 s (0.067 mL STP of O_2). The amount of adsorbed oxygen corresponds to the OSC. To determine complete oxygen storage capacity (OSCc) nine sequential CO pulses 10 s each (0.33 mL STP of CO each) were applied, separated by 60 s pauses when only Ar were fed. Subsequently, five 2 s pulses of oxygen are fed, separated by 80 s pauses in pure Ar. The total amount of oxygen absorbed is considered to be the OSCc.

3. RESULTS

3.1. Characterization before the Reaction. In Figure 1, we show SEM and TEM images of the as-prepared shape-controlled CeO_2 particles. The nanocubes reveal a regular shape with edge lengths in the range of 30–50 nm (cf. Figure 1A,B). The determined d-spacing derived from high-resolution TEM of 0.27 nm is consistent with the layer spacing in (100) orientation (cf. Figure 1C).

The regularity of the octahedral particles can be best seen in SEM images, rather than in TEM images (cf. Figure 1D,E), with edge lengths ranging from 100 to 150 nm. From the observed spacing of 0.31 nm in the high-resolution TEM image we infer that these particles expose preferentially (111) facets (cf. Figure 1F).

The nanorods exhibit an average length of 200–250 nm and a width of approximately 10 nm (cf. Figure 1H). According to high-resolution TEM, the observed spacing in the entire rod corresponds to the (111) lattice plane (cf. Figure 1I). The orientation of these interferences is rotated 35° relatively to the surface. Therefore, based on the cubic geometry, the surfaces expose (110) lattice planes, which is in accordance with current literature[8] (cf. Figure 1I and cf. Figure S1A,B). The inset shows the FFT of the rods and strongly supports the impression of nearly perfect crystallinity as only the (111) point pattern is observed. We also observe nanorods exposing the (100) surface (cf. Figure S1C), which is also in agreement with previous studies in which the surface termination in CeO_2 nanorods is still under discussion.[30–32] TEM analyses on several particles indicate that the large majority of these particles exhibit (110) surfaces, but based on FFT, we find that also (100) planes have

Table 1. Characterization of the Shape-Controlled Nanoparticles after Preparation and before HCl Oxidation Reaction

	BET surface area ($m^2 g^{-1}$)	XPS Ce^{3+} (%)	particle size (nm)	OSC $\mu mol(O)/g$ ($\mu mol(O)/m^2$)	OSCc $\mu mol(O)/g$ ($\mu mol(O)/m^2$)
rods	77	23	$10 \times 200-250$	56 (0.73)	156 (2.02)
cubes	22	21	$30-50$	10 (0.45)	102 (4.64)
octahedrons	6	20	$100-150$	3 (0.5)	57 (9.5)

to be present in some cases. However, the corresponding coherent areas cannot directly be detected in the TEM image. These findings are fully consistent with previous studies.[15,24]

From TEM studies, we infer that the predominantly exposed facets of the octahedrons, rods, and cubes are oriented along (111), (110), and (100) facets, respectively, consistent with previous studies.[8,33]

From Rietveld analyses of the XRD data (cf. Figure S2), all three sorts of nanoparticles are inferred to be phase-pure indicating CaF_2 structure, and the average particle size is found to be 30 nm (cubes), 87 nm (octahedrons), and 15 nm (rods); recall that XRD overemphasizes large particles. Physisorption experiments reveal BET surface areas of $22 m^2/g$ (cubes), $6 m^2/g$ (octahedrons), and $77 m^2/g$ (rods) (cf. Table 1). These values are broadly compatible with the average particle size estimated by TEM.

The XPS survey spectrum (shown in Figure S4A) of the as-prepared CeO_2 nano-octa shows only spectral features that are assigned to Ce, O, and C; carbon is likely coming from contamination of the nanoparticles when exposed to ambient atmosphere. In order to quantify the concentration of Ce^{3+} in the surface selvedge region (about 3–4 nm thick) we applied photoelectron emission of the Ce 3d.[34–42] These Ce 3d spectra (shown in Figure S3) are quite complex with ten spectral features, whose interpretation is traced to many-body effects.[43,44] Six of them denoted by v, v″, v‴, u, u″, and u‴ in black are assigned to Ce^{4+}, while the four other peaks v_0, v′, u_0, and u′ in orange belong to Ce^{3+}.[25] From the reference spectrum of Ce_2O_3 (shown in Figure S5) the energetic positions of Ce^{3+}, the area ratios and fwhm (full width at half maximum) among the Ce^{3+} related peaks can be determined first and then be utilized in the fitting procedure of Ce 3d spectra of shape-controlled CeO_2 particles. The Ce^{3+} concentration is about 20–23% of all the Ce atoms with only minor variations among the three morphologies. More specifically, the observed order of Ce^{3+} concentrations are rods (23%) > cubes (21%) > octahedrons (20%), although the observed differences are close to the accuracy limits of this method. The determined Ce^{3+} concentrations (cf. Table 1) agree quite well with those reported in the literature.[45,46]

Closely related with the concentration of Ce^{3+} is the oxygen storage capacity (OSC). Within the Kröger–Vink notation, the oxygen incorporation is given by $2Ce^{3+} + V_O^{\circ\circ} + 1/2O_2 \rightarrow O_O^x + 2Ce^{4+}$, where V_O are oxygen vacancies and O_O^x denotes O^{2-} on regular anionic positions. The plain OSC varies quite substantially among the three morphologies (cf. Table 1). However, the plain OSC normalized to the BET surface area is about 0.5–0.7 $\mu mol(O)/m^2$ irrespective of the crystal shape; the highest OSC/BET value is found for rods consistent with the highest Ce^{3+} concentration. This finding is consistent with the view that the plain OSC is a surface property. Quite in contrast, the complete OSC (OSCc) is a bulk property and accordingly these values scatter much less among the three morphologies.

The OSC value of nanocubes (10 $\mu mol(O)/g$) fits quite well to literature values[47] (12 $\mu mol(O)/g$), while our OSC value of

nanorods (56 $\mu mol(O)/g$) is much higher than the value for nanorods in this study (18 $\mu mol(O)/g$). The OSC value for CeO_2 powder is 392 $\mu g(O)/g$.[6] This value translates to 24.5 $\mu mol(O)/g$, which is in reasonable agreement with our values in Table 1. A recent study[23] used thermogravimetric analysis (TGA) for the OSC measurements of nanocubes. The reduction in TGA was performed with a Ar/H_2 mixture for 30 min, so that OSCc values rather than plain OSC values have been determined. We would like to note that OSC and OSCc values can be either normalized to the mass or to the surface area. The previously published value[23] of 6.8 $\mu mol(O)/m^2$ agrees reasonably well with our value of 4.6 $\mu mol(O)/m^2$.

We need to emphasize that the protocols for OSC experiments differ quite substantially among the various research groups, thus rendering a direct comparison with literature values difficult. The derived OSC/BET and OSC values in Table 1 are compatible with the formation energy for oxygen vacancy: 3.3 eV (111), 2.69 eV (110), and 2.97 eV (100).[17]

3.2. Activity Experiments: HCl Oxidation Reaction. The activity experiments are summarized in Figure 2. The reactor is brought first to its nominal reaction temperature of 430 °C in pure Ar flow of 15 sccm. At $t = 0$ s, the Ar flow is
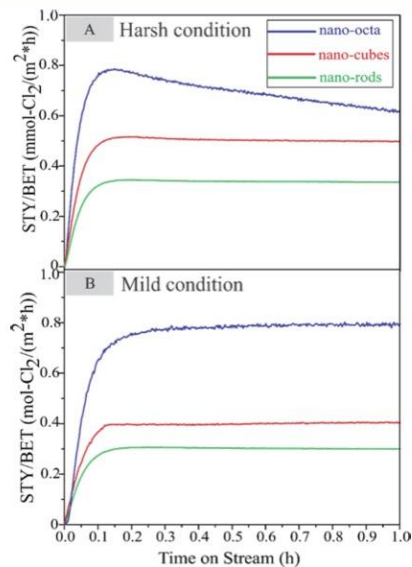

Figure 2. Space time yield (STY) per BET surface area of molecular chlorine in the HCl oxidation reaction is shown for the shape-controlled CeO_2 nanoparticle (octahedrons, cubes, and rods). The temperature during the reaction was 430 °C. (a) harsh reaction conditions: $Ar:HCl:O_2 = 6:2:2$ and (b) mild reaction conditions: $Ar:HCl:O_2 = 7:1:2$ and a flow rate of 15 sccm.

switched to the reaction mixture (harsh: Ar:HCl:O$_2$ = 6:2:2, mild: Ar:HCl:O$_2$ = 7:1:2), and the space time yield (STY) is measured online by UV−vis and normalized to the BET surface area in Figure 2; the original STY data are presented in the SI (Figure S6).

The induction period lasts 10−15 min until the reactor reaches steady-state conditions. Under harsh and mild reaction conditions, the order in activity is octahedrons > cubes > rods. Except for the octahedrons under harsh conditions, the Deacon reaction reaches steady state after the induction period and is stable over time on stream. For the case of octahedral and harsh conditions, a clear deactivation is evident that is not terminated after 1 h.

In Figure 3 we summarize the activity experiments for various temperatures and reaction mixtures. From the *T*-
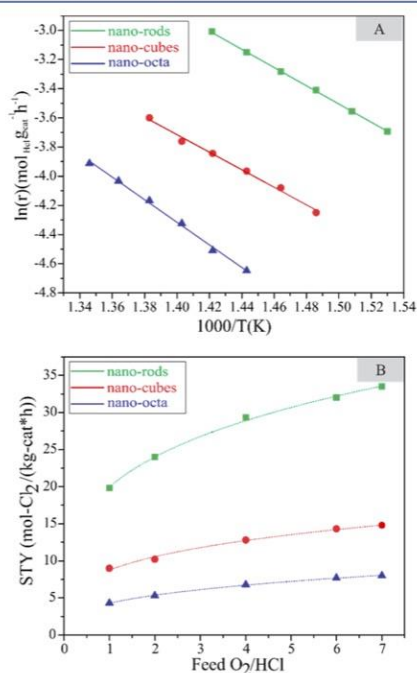
Figure 3. (A): ln *r* (reaction rate of HCl) as a function of 1/*T* for mild reaction conditions (O$_2$:HCl:Ar = 2:1:7) at different temperature. (B): STY versus feed of O$_2$/HCl ratio at 430 °C for shape-controlled CeO$_2$ nanoparticles (octahedrons, cubes and rods). Reaction condition: 10% HCl and 10−70% O$_2$ balanced in Ar and the total flow rate was fixed at 15 sccm/min. The fitting curves shown are derived according to the Arrhenius equation (A) and to a power law (B: dotted line)).

dependent activity data shown as Arrhenius plots (Figure 3A) we determine the apparent activation energies for the three morphologies. It turns out the apparent activation energy of the octahedrons (65 kJ/mol) is the highest, while the apparent activation energies of cubes and rods are practically identical (50−52 kJ/mol) (cf. Table 2).

These values can be utilized as benchmarks for future microkinetic modeling of the HCl oxidation reaction over

Table 2. Apparent Activation Energies and Reaction Orders for the HCl Oxidation over Various Shape-Controlled CeO$_2$ Nanoparticles

	nanorods	nanocubes	nano-octa
apparent activation energy (kJ/mol)	52.0 ± 0.4	50.0 ± 2.0	65.0 ± 1.8
oxygen order	0.26	0.27	0.32

CeO$_2$ since the surface termination of the three kinds of nanoshaped CeO$_2$ particles is dominated by a well-defined facet; we need to remind that the shape of nanorods might be a combination of (110) and (100) facets. The experiments for determining the reaction order are shown in Figure 3B. For all three particles shapes, the STY increases with increasing oxygen concentration, revealing reaction orders in the range of 0.26 to 0.32. Both the apparent activation energies and the reaction order in oxygen are compiled in Table 2.

3.3. Stability Experiments: HCl Oxidation Reaction. The stability of CeO$_2$-based catalyst is affected by bulk chlorination.[6,28] In the following we focus on the reaction-induced chlorination of the catalysts under two specific reaction conditions, namely, "harsh" and "mild" when the reaction mixture is Ar:HCl:O$_2$ = 6:2:2 and HCl:O$_2$ = 7:1:2, respectively, with a flow rate of 15 sccm.

We start these investigations by comparing XRD experiments before and after Deacon reaction (cf. Figure 4). Clearly, under mild reaction conditions none of the morphologies forms crystalline hydrated CeCl$_3$, while under harsh reaction condition both cubes and octahedrons reveal a high degree of chlorination already after 1h on reactant stream.

The most surprising results is, however, that the rods are stable even under harsh reaction conditions. In order to ensure that this stability is not due to a too short reaction time of 1 h, we prolonged the time on stream for harsh reaction conditions up to 8 h. The evolution of the XRD scans is compiled in Figure 5, revealing no signature of crystalline bulk chlorination.

In order to quantify the concentration of Ce^{3+} and that of chlorine accommodated in the surface region after Deacon reaction under harsh and mild conditions, we performed XPS experiments of all three shaped-controlled nanoparticles (cf. Figure 6). The survey spectrum of nano-octahedrons after harsh condition (cf. Figure S4B) indicates only C, Ce, Cl, and O species. From XRD experiments, we know already that nanocubes and nano-octa form crystalline CeCl$_3$*nH$_2$O after harsh Deacon reaction conditions. Therefore, we measured an additional Ce 3d reference spectrum of pure CeCl$_3$ to determine the energetic positions Ce^{3+} due to bulk chloride formation (shown in Figure S5). The spectral features of Ce^{3+} in CeCl$_3$ are shifted to higher BE compared to Ce^{3+} of Ce$_2$O$_3$, consistent with a previous study.[39] The Ce^{3+} peaks from CeCl$_3$ are labeled by v_0^{Cl}, v'_{Cl}, u_0^{Cl}, and u'_{Cl} in magenta. With both reference spectra (Ce$_2$O$_3$ and CeCl$_3$), the Ce 3d spectra of the shape-controlled CeO$_2$ nanoparticles after harsh Deacon reaction were fitted (cf. Figure 6). Under mild reaction conditions, the ratio of Cl to Ce (Cl/Ce) is 10%, 11%, 15% for rods, cubes, and octahedrons, respectively. These values are low enough to be explained by near-surface rather than crystalline bulk chlorination and therefore are compatible with corresponding XRD data and their Rietveld refinements, in that the XRD patterns are predominantly determined by the bulk part of the particles. The very same trend of the Cl concentration is observed for the Ce^{3+} concentration. In comparison with the
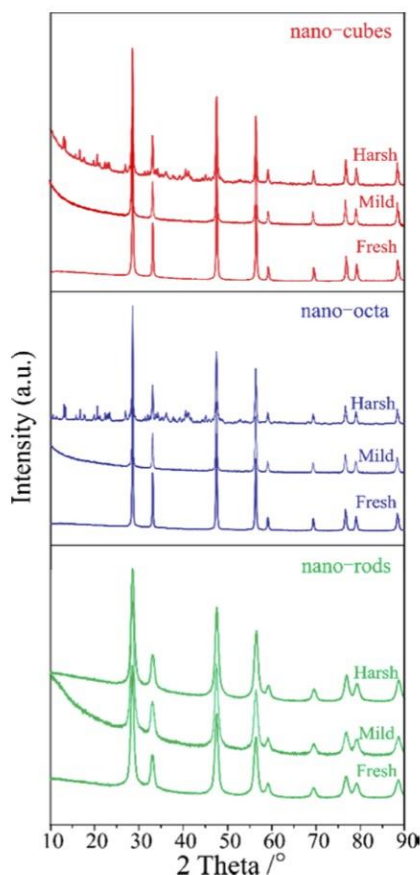
Figure 4. XRD scans after Deacon reaction under harsh and mild conditions in comparison with the freshly prepared samples. Blue: octahedrons, red: cubes, green: rods.
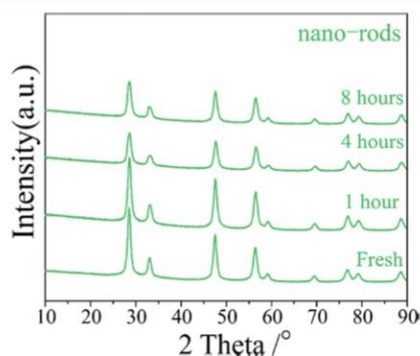

Figure 5. XRD scans of CeO_2 nanorods after running the Deacon reaction under harsh conditions for various reaction times up to 8 h.

freshly prepared particles (cf. Table 1), the Ce^{3+} concentration of all morphologies has slightly increased after HCl oxidation reaction under mild conditions (Table 3).

Under harsh reaction conditions, the situation changes dramatically. The chlorine uptake of cubes and octahedrons is increased by a factor of 7 and 10, respectively. From the estimated ratio of Cl to Ce, we conclude that CeO_2 cubes and octahedrons are partially transformed to $CeCl_3$. These findings agree well with the fraction of hydrated $CeCl_3$ determined from XRD, providing 34% and 11% of hydrated $CeCl_3$ for CeO_2 octahedrons and cubes, respectively. Under harsh reaction conditions, the chlorine uptake of rods is only increased from 10% to 19%, which is consistent CeO_2 nanorods being still mainly surface chlorinated or the additional chlorine penetrates the surface region of CeO_2 rods without affecting the stability of the rods.

The chlorination of CeO_2 after the Deacon reaction under harsh and mild conditions is accompanied by an increase in the Ce^{3+} concentration. This observation is due to the reduction of CeO_2 (Ce^{4+}) into $CeCl_3$ (Ce^{3+}), but it is difficult to understand when Cl accommodation takes place only at the surface or in oxygen vacancies. In this case, we would anticipate a reduction of Ce^{3+} concentration. However, besides Cl^-, also H^+ is adsorbing on the surface and water is formed as a byproduct in the Deacon process. In this way, lattice oxygen of CeO_2 can be removed by water formation/desorption or replaced by chlorine adsorption. Therefore, CeO_2 may be chemically reduced during the Deacon reaction, consistent with an increasing Ce^{3+} concentration.

In Figure 7 we summarize the TEM experiments of the shape-controlled CeO_2 nanoparticles after Deacon reaction under mild and harsh reaction conditions. For mild reaction conditions the TEM images of the three morphologies of CeO_2 nanoparticles do not reveal any sign of transformation or corrosion along with the chlorination, which is fully consistent with XRD (Figure 4) and XPS data (Figure 6). These TEM images look actually quite similar to those shown in Figure 1 for the freshly prepared shape-controlled CeO_2 nanoparticles, while after harsh reaction conditions, TEM images of both cubes and octahedrons change considerably. In this case, the nanoparticles lose their well-defined shape and deposits with less-defined morphology adhere to the facets of cubes and octahedrons (indicated by ellipses in Figure 7). We assume that this shapeless material is likely to be hydrated $CeCl_3$, as inferred from detailed Rietveld analyses of the XRD data and consistent with the dramatic increase in the Cl concentration observed in XPS experiments.

For the nanocubes, we can recognize in TEM that the shape of the cubes is largely destroyed, the smooth facets are roughened, and the averaged particle size increases from 50 to 70 nm. Formerly sharp corners become rounded as marked by the red squares in Figure 7. For the nano-octahedrons, we encounter the same phenomenon as with nanocubes: the well-defined shape of some of the octahedrons is lost, and straight facets become considerably roughened. This change in morphology of the octahedrons becomes even more apparent in SEM micrographs (cf. Figure S7), indicating severe sintering of the particles.

For the nanorods, we cannot observe any morphological changes in the TEM images (cf. Figure 7E,F). However, it seems in TEM that the rods become shorter after reaction consistent with the observed decrease in diffraction intensity after reaction in Figure 5. Consistent with the XRD data in
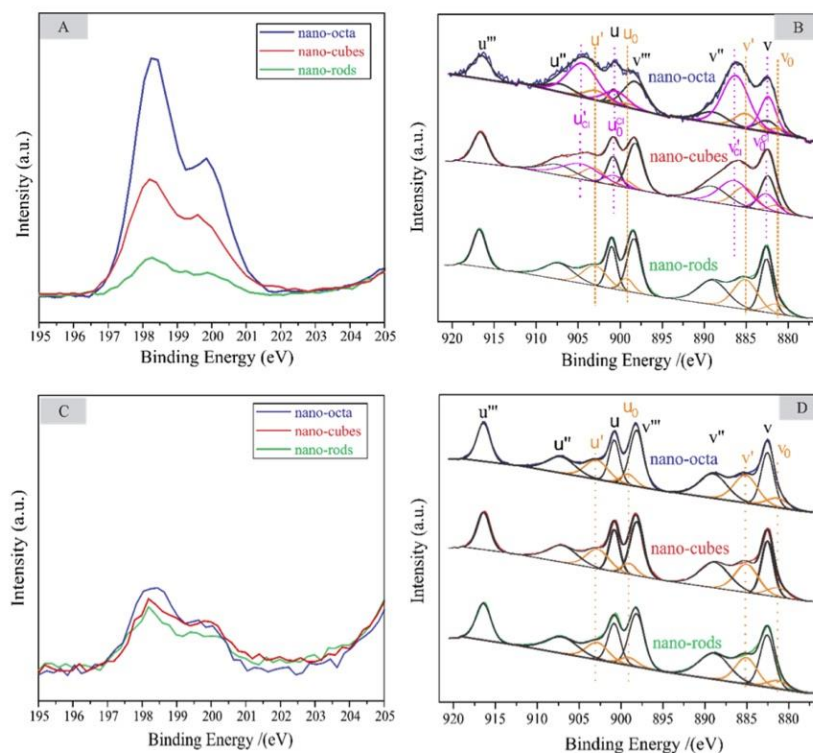
Figure 6. XPS spectra of Cl 2p and Ce 3d of shaped-controlled CeO_2 nanoparticle (octahedrons, cubes and rods). (A) and (B) are Cl 2p and Ce 3d spectra, respectively, after Deacon reaction under harsh condition. (C) and (D) are Cl 2p and Ce 3d spectra respectively after Deacon reaction under mild condition. The Ce^{3+} related features in Ce 3d originating in Ce_2O_3 and $CeCl_3$ environment are given in orange and magenta, respectively.

Table 3. Summary of the XPS Experiments[a]

		rods	cubes	octahedrons
fresh sample	$Ce^{3+}/(Ce^{3+}+Ce^{4+})$	23%	21%	20%
mild condition	$Ce^{3+}/(Ce^{3+}+Ce^{4+})$	24%	28%	29%
	Cl/Ce	10%	11%	15%
harsh condition	$Ce^{3+}/(Ce^{3+}+Ce^{4+})$	30%	49% $(18^{①}+31^{②})$%	67.0% $(12^{①}+55^{②})$%
	Cl/Ce	19%	85%	150%

[a]Concentrations of Cl and Ce^{3+} of the fresh sample and the sample after harsh and mild HCl oxidation reaction for 1 h on stream at 430°C. ① and ② Ce^{3+} originating from the Ce_2O_3 and $CeCl_3$, respectively.

Figure S, we conclude that no chlorination of the CeO_2 nanorods has taken place.

4. DISCUSSION

4.1. HCl Oxidation: Activity of Shape-Controlled CeO_2 Particles. There are two principal ways to quantify activity. Either one uses the space time yield (STY) which quantifies the amount of produced chlorine in mole per time and relates this quantity to the total mass of the catalyst. The STY neglects the dependence of the activity on the surface area. Alternatively, one can employ a measure of activity that is referenced against the total surface area (BET area), for instance STY/BET area.

This activity measure (over)emphasizes the importance of the surface area.

For the case of shape-controlled CeO_2 nanoparticles, the gravimetric activity (STY) of the rods is much larger than that of the cubes and this again is larger than the activity of the octahedrons (cf. Figure S2). However, the BET surface area follows the same trend as the STY: rods (110) > cubes (100) > octahedrons (111) irrespective of the chosen reactant mixture (mild versus harsh). This may provide good reasoning for quantifying the activity by STY/BET area instead of STY. The activity with respect to the BET surface area can be envisioned as the inherent activity of the particles and is justified as long as the activity is dominated by surface processes. The surface-normalized STY of the particles the activity runs in the
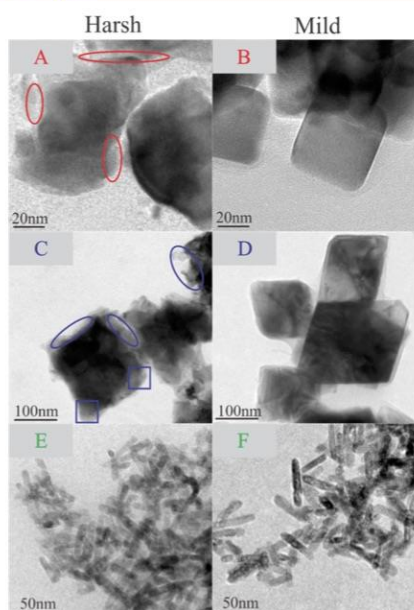
Figure 7. TEM images of shape-controlled CeO_2 nanoparticles after running the Deacon reaction under mild and harsh conditions. A/B cubes, C/D octahedrons, and E/F rods. A,C,E show the nanoparticles after harsh conditions and B,D,F present the nanoparticles after mild conditions.

following order: octahedrons (111) > cubes (100) > rods (110) (cf. Figure 2).

Both activity orderings are somehow surprising as the facets with the highest surface energy, namely (100), is not identified with that of the highest activity; the surface energies of these bulk-truncated orientations are 0.69 J/m^2 (111), 1.04 J/m^2 (110), and 1.41 J/m^2 (100).[17−19] However, a comparison with the surface energies is likely to be too simplistic for two reasons. First, the surface energies are calculated for bulk-truncated (1×1) surface terminations, although for instance the (100) facet is known to reconstruct with an unknown surface structure.[17] Second, under HCl oxidation reaction conditions, the stability of the facets in terms of surface energies may change due to Cl and H adsorption.

From the activity experiments in Figure 2, no activity loss is observed for all three morphologies under mild reaction conditions. Quite in contrast, under harsh reaction conditions, octahedral particles deactivate during the Deacon reaction, while cubes and rods reveal stable activity.

The activity of CeO_2 in oxidation catalysis is frequently attributed to the oxygen storage capacity (OSC).[48−53] In the following, we discuss this correlation for the case of the Deacon reaction. There are two extremes to quantify the OSC: Either one measures the plain OSC that corresponds to the surface contribution of oxygen storage capacity, or one considers the complete OSC (OSCc), i.e. the oxygen storage capacity of the whole material that approximates a bulk property. If the surface reaction is much slower than the exchange of oxygen vacancies from the bulk of the particle to the surface, then OSCc is a

suitable measure for the comparison of activity with oxygen storage capacity. In case the reaction rate is much faster than the exchange process of oxygen vacancies from the particles' interior, plain OSC is the proper quantity to which the activity should be compared.

In Figure 8 OSC and activity data are compared for each particle morphology. In order to be consistent with the
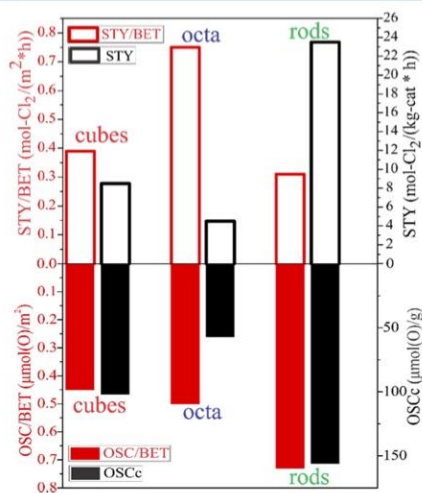

Figure 8. Comparison of oxygen storage capacity with activity in the Deacon process under mild conditions and $T = 703$ K for shape-controlled CeO_2 nanoparticles.

underlying physical chemistry, the STY needs to be compared with OSCc (black in Figure 8) while that of the STY/BET to the OSC/BET (red in Figure 8). There is no clear correlation between OSC/BET (filled red bars) and STY/BET (open red bars) in Figure 8, but the STY (open black bars) follows quite closely the OSCc (filled black bars). This latter correlation may provide evidence that the OSCc affects the activity of CeO_2 in the Deacon process as already suggested by Amrute et al. for CeO_2 powder.[6] The O^{2-} diffusion coefficient at 430 °C, the chosen reaction temperature in the Deacon process, is about 10^{-15} m^2/s.[54,55] This value translates into a diffusion of oxygen ions of roughly 30 nm per second so that the time scale for exchanging surface and bulk oxygen is of the same order of magnitude as the inverse turnover frequency derived from STY/BET (about 1 s^{-1}). Therefore, oxygen vacancies from the bulk of the nanoscaled CeO_2 particles can contribute significantly to the catalyzed HCl oxidation reaction.

In order to compare the activity data of shape-controlled CeO_2 particles with those acquired in Pérez-Ramírez group, we convert the STY values in corresponding conversion values (cf. Table 4). The HCl conversion of CeO_2 powder published by Amrute et al.[6] is 25% at the same reaction temperature and the same ratio of $Ar:HCl:O_2 = 7:1:2$ as in the present study (mild reaction conditions). Considering the weight hourly space velocity (WHSV) values of 33.2 mL/(g·min), the conversion reported by Amrute et al.[6] translates roughly to 11% for WHSV of 75 mL/(g*min) as used in our experiments. This value of Amrute et al. matches quite well our average value of HCl

Table 4. HCl Conversion over Shape-Controlled CeO$_2$ Nanoparticles under Harsh (Ar:HCl:O$_2$ = 6:2:2) and Mild (Ar:HCl:O$_2$ = 7:1:2) Reaction Conditions at 703 K[a]

HCl conversion	nanorods	nanocubes	nano-octa
harsh	13%	5.5%	2%
mild	23.5%	8.5%	4.5%

[a]The weight hourly space velocity WHSV value is 75 mL/(g·min).

conversion (Table 4). The STY of CeO$_2$ powder[6] turned out to be 11.1 mol-Cl$_2$/ (kg-cat·h), while our STY values are 25, 8.5, and 4.0 mol-Cl$_2$/ (kg-cat·h) for rods, cubes, and octahedrons, respectively. Also the average STY values agree remarkable well between these studies.

The greatest advantage of using shape-controlled CeO$_2$ nanoparticles in catalysis research is that we can correlate the activity (and also stability) to the specific surface structure (facet orientation), thus allowing for structure−activity (stability) correlations. For the case of octahedrons, the particles expose preferentially facets with (111) orientation. The surface structure of the autocompensated (111) surface is likely to be bulk-truncated, thus being able to validate a proposed reaction mechanism by Amrute et al.[6] For the cases of cubes and rods, the situation is more involved than with octahedrons. The (100) facets are likely to undergo surface reconstructions,[56,57] whose atomic structure is unknown. For the CeO$_2$ rods, even the orientation of the exposing facets is under discussion. Most of the studies conclude that rods expose preferentially (110) facets, which is concluded from the layer spacing derived from Figure 1. However, a recent TEM study[32] showed that the side walls of the rods are indeed oriented along the crystallographic (110) direction, but the surface restructures and exposes preferentially (111) microfacets in a sawtooth fashion.

For the three morphologies we performed formal kinetics experiments, i.e., we determined the apparent activation energy and reaction order for the HCl oxidation reaction under mild conditions; note that only under mild conditions all three morphologies were stable. Independent of the morphology of the nanoparticles, the reaction order in oxygen is positive, i.e., with increasing oxygen partial pressure also the conversion increases being consistent with previous experiments for CeO$_2$ powder.[6] The highest reaction order in oxygen is found for octahedrons (0.32) predominantly exposing (111) facets. The reaction orders of rods (0.26) and cubes (0.27) are practically identical.

The apparent activation energies of rods (52 kJ/mol) and cubes (50 kJ/mol) are virtually identical and quite different from that obtained for the octahedrons exposing preferentially (111) facets (65 kJ/mol). From the apparent activation energies, the reaction mechanisms of HCl oxidation over rods and cubes are considered similar, while the reaction mechanism may be different for octahedrons.

4.2. HCl Oxidation: Stability of Shape-Controlled CeO$_2$ Particles. TEM, XRD, and XPS indicate clearly that under mild reaction conditions none of the studied morphologies (cubes, octahedrons, rods) form (crystalline) CeCl$_3$. This result is consistent with corresponding studies of CeO$_2$ powder and CeO$_2$ nanofibers,[6,27] suggesting that the oxygen concentration in the feed plays a key role for suppressing bulk chlorination of the CeO$_2$.

Under harsh reaction conditions both cubes and octahedrons undergo severe bulk-chlorination already after 1 h on stream as evidenced by TEM, XRD, and XPS. Quantitative Rietveld refinement of the XRD data reveals that the degree of chlorination depends on the orientation: 11% of CeO$_2$ cubes and even 34% of hydrated CeO$_2$ octahedrons are transformed to CeCl$_3$. These values fit remarkably well to the observed chlorination in XPS and can be visualized in TEM micrographs. Octahedrons are the least stable CeO$_2$ morphology, although both the surface energy of (111) facets and the total surface area are the lowest among the three studied morphologies.

XPS provides quantitative information about surface Cl concentration. It turns out that also under mild Deacon conditions the CeO$_2$ particles are covered by chlorine. Referencing the chlorine signal to the Ce 3d peak intensity results in Cl coverages of about one monolayer that can readily be accommodated on the surface of the nanoparticles and in O vacancies of the particles. Quite in contrast, in partial bulk chlorination of CeO$_2$, the Cl 2p signal in XPS is much higher, consistent with XRD results (formation of crystalline hydrated CeCl$_3$). A recent Prompt Gamma Activation Analysis (PGAA) study of CeO$_2$ powder[7] indicated that chlorine is able to penetrate the bulk structure under oxidizing reaction conditions (O$_2$:HCl= 9:1, T = 703 K) occupying the O-vacancy positions without forming hydrated CeCl$_3$. Our XPS study is consistent with this interpretation.

The most surprising result of our stability study is that rods are strikingly stable under harsh reaction conditions. Even if we increase the reaction time by a factor of 8, no chlorination is discernible in XRD. The BET surface area of rods is highest and still corrosion is lowest. Therefore, the observed stability in the Deacon reaction is envisioned as an intrinsic property of the CeO$_2$ rods.

The thermodynamics of the chlorination of CeO$_2$ is essentially a bulk property and therefore independent of the surface orientation. The varying degree of chlorination of the shape-controlled CeO$_2$ nanoparticles must therefore result from the kinetics of the chlorination process, more precisely from surface kinetics. From the TEM images we can conclude that the chlorination process of CeO$_2$ proceeds via nucleation and growth: CeO$_2$ is corroded very likely starting from the step edges and the released Ce atoms that nucleate to form CeCl$_3$ on the CeO$_2$ particle surface which subsequently grows in size.

In order to explain the orientation-dependent chlorination of CeO$_2$ particles, the kinetics needs to be different on the different three facets. It may be that the CeO$_2$ rods can form a self-protecting surface chloride, similar to the case of RuO$_2$(110).[58] A recent paper by Yang and co-workers demonstrated that the rods undergo a surface reconstruction, exposing (111) oriented microfacets.[32] Whether this reconstruction is stabilized also under HCl oxidation reaction is not known, but from the observed stability and reactivity of the rods, which is clearly different from that of (111) oriented octahedrons, we infer that the surface termination of rods should be different from that of octahedrons.

The main conclusion is that besides oxygen concentration in the gas feed the shape and therefore the exposing facets of the CeO$_2$ particles determine its stability against bulk chlorination.

5. CONCLUSIONS

From TEM studies, we infer that the predominantly exposed facets of the octahedrons, rods, and cubes are oriented along (111), (110) and (100) facets, respectively. These shape-controlled CeO$_2$ particles were employed in the catalytic oxidation of HCl (Deacon process) under mild and harsh

reaction conditions to address shape-selective activity and stability. It turns out that both activity and stability are structure-sensitive that is not reconciled with corresponding surface energies and the formation energies of O-vacancies. Using space time yield (STY) as a measure of activity, the rods are the most active particles, followed by the cubes and finally the octahedrons. This very same trend has also been observed for the complete oxygen storage capacity (OSCc), indicating a correlation between the observed activity STY and the OSCc.

All particle morphologies studied are stable under mild Deacon reaction conditions (Ar:HCl:O_2 = 7:1:2). Under harsh reaction conditions (Ar:HCl:O_2 = 6:2:2), only the rods are stable, while cubes and octahedrons form crystalline bulk hydrated $CeCl_3$. Accordingly, the stability of the shape-controlled CeO_2 particles is shown to be facet-depending as well: The rods exposing facets preferentially oriented in (110) direction are much more stable than octahedrons and cubes with preferential (111) and (100) facets, respectively.

In general, it has been observed that the activity of a catalyst material for the Deacon process is anticorrelated with its stability: the higher the activity, the lower the stability. This behavior is not encountered with shape-controlled CeO_2 particles. CeO_2 rods reveals the highest activity per gram (STY) and the highest stability.

We studied the formal kinetics of the HCl oxidation reaction over shape-controlled CeO_2 particles. The reaction orders in oxygen of all three morphologies are positive: rods (0.26), cubes (0.27), and octahedrons (0.32). The apparent activation energies are about 50−52 kJ/mol for cubes and rods, while that for octahedrons is substantially higher, namely, 65 kJ/mol. These kinetic experiments on shape-controlled CeO_2 particles may serve as benchmarks for (future) microkinetic modeling based on first-principles, thus allowing us to deepen our understanding of the underlying reaction mechanism.

■ ASSOCIATED CONTENT

ⓢ Supporting Information

The Supporting Information is available free of charge on the ACS Publications website at DOI: 10.1021/acscatal.7b01618.

HR-TEM of the as-prepared CeO_2 nanorods, indicating (100) and (111) facets; XRD scans of the as-prepared shape-controlled CeO_2 particles, XPS spectra and their deconvolution of Ce 3d of as prepared shape-controlled CeO_2 particles, XPS survey spectra of as-prepared CeO_2 nano-octahedrons and CeO_2 nan-octahedrons after harsh Deacon reaction, XPS reference spectra of Ce_2O_3 and $CeCl_3$, STY in the HCl oxidation reaction using shape-controlled CeO_2 particles, SEM micrographs of CeO_2 nano-octadedrons after Deacon reaction under harsh conditions (PDF)

■ AUTHOR INFORMATION

Corresponding Authors

*E-mail: herbert.over@phys.chemie.uni-giessen.de.
*E-mail: Bernd.Smarsly@phys.Chemie.uni-giessen.de.
*E-mail: ylguo@ecust.edu.cn.

ORCID ⊙

Bernd M. Smarsly: 0000-0001-8452-2663
Herbert Over: 0000-0001-7689-7385

Notes

The authors declare no competing financial interest.

■ REFERENCES

(1) Hisham, M. W. M.; Benson, S. W. *J. Phys. Chem.* **1995**, *99*, 6194−6198.
(2) Pérez-Ramírez, J.; Mondelli, C.; Schmidt, T.; Schlüter, O. F. K.; Wolf, A.; Mleczko, L.; Dreier, T. *Energy Environ. Sci.* **2011**, *4*, 4786−4799.
(3) Seki, K. *Catal. Surv. Asia* **2010**, *14*, 168−175.
(4) Over, H.; Schomäcker, R. *ACS Catal.* **2013**, *3*, 1034−1046.
(5) Feng, K. K.; Li, C. W.; Guo, Y. L.; Zhan, W. C.; Ma, B. Q.; Chen, B. W.; Yuan, M. Q.; Lu, G. Z. *Appl. Catal., B* **2015**, *164*, 483−487.
(6) Amrute, A. P.; Mondelli, C.; Moser, M.; Novell-Leruth, G.; López, N.; Rosenthal, D.; Farra, R.; Schuster, M. E.; Teschner, D.; Schmidt, T.; Pérez-Ramírez, J. *J. Catal.* **2012**, *286*, 287−297.
(7) Farra, R.; Eichelbaum, M.; Schlögl, R.; Szentmiklósi, L.; Schmidt, T.; Amrute, A. P.; Mondelli, C.; Pérez-Ramírez, J.; Teschner, D. *J. Catal.* **2013**, *297*, 119−127.
(8) Mai, H. X.; Sun, L. D.; Zhang, Y. W.; Si, R.; Feng, W.; Zhang, H. P.; Liu, H. C.; Yan, C. H. *J. Phys. Chem. B* **2005**, *109*, 24380−24385.
(9) Zhou, K. B.; Wang, X.; Sun, X. M.; Peng, Q.; Li, Y. D. *J. Catal.* **2005**, *229*, 206−212.
(10) Tana; Zhang, M. L.; Li, J.; Li, H. J.; Li, Y.; Shen, W. J. *Catal. Today* **2009**, *148*, 179−183.
(11) Wu, Z. L.; Li, M. J.; Overbury, S. H. *J. Catal.* **2012**, *285*, 61−73.
(12) Qiao, Z. A.; Wu, Z. L.; Dai, S. *ChemSusChem* **2013**, *6*, 1821−1833.
(13) Mann, A. K. P.; Wu, Z. L.; Calaza, F. C.; Overbury, S. H. *ACS Catal.* **2014**, *4*, 2437−2448.
(14) Huang, W. X.; Gao, Y. X. *Catal. Sci. Technol.* **2014**, *4*, 3772−3784.
(15) Hu, Z.; Liu, X. F.; Meng, D. M.; Guo, Y.; Guo, Y. L.; Lu, G. Z. *ACS Catal.* **2016**, *6*, 2265−2279.
(16) Capdevila-Cortada, M.; Garcia-Melchor, M.; López, N. *J. Catal.* **2015**, *327*, 58−64.
(17) Mullins, D. R. *Surf. Sci. Rep.* **2015**, *70*, 42−85.
(18) Ganduglia-Pirovano, M. V.; Hofmann, A.; Sauer, J. *Surf. Sci. Rep.* **2007**, *62*, 219−270.
(19) Paier, J.; Penschke, C.; Sauer, J. *Chem. Rev.* **2013**, *113*, 3949−3985.
(20) Nolan, M.; Parker, S. C.; Watson, G. W. *Surf. Sci.* **2005**, *595*, 223−232.
(21) Capdevila-Cortada, M.; López, M. *Nat. Mater.* **2017**, *16*, 328−334.
(22) Aneggi, E.; Wiater, D.; de Leitenburg, C.; Llorca, J.; Trovarelli, A. *ACS Catal.* **2014**, *4*, 172−181.
(23) Vile, G.; Colussi, S.; Krumeich, F.; Trovarelli, A.; Pérez-Ramírez, J. *Angew. Chem., Int. Ed.* **2014**, *53*, 12069−12072.
(24) He, J. L.; Xu, T.; Wang, Z. H.; Zhang, Q. H.; Deng, W. P.; Wang, Y. *Angew. Chem., Int. Ed.* **2012**, *51*, 2438−2442.
(25) Burroughs, P.; Hamnett, A.; Orchard, A. F.; Thornton, G. *J. Chem. Soc., Dalton Trans.* **1976**, *17*, 1686.
(26) Romeo, M.; Bak, K.; El Fallah, J.; Le Normand, F.; Hilaire, L. *Surf. Interface Anal.* **1993**, *20*, 508−512.

(27) Kanzler, Ch.; Urban, S.; Zalewska-Wierzbicka, K.; Hess, F.; Rohrlack, S. F.; Wessel, C.; Ostermann, R.; Hofmann, J. P.; Smarsly, B. M.; Over, H. ChemCatChem 2013, 5, 2621−2626.

(28) Möller, M.; Over, H.; Smarsly, B. M.; Tarabanko, N.; Urban, S. Catal. Today 2015, 253, 207−218.

(29) Möller, M.; Urban, S.; Cop, P.; Weller, T.; Ellinghaus, R.; Kleine-Boymann, M.; Fiedler, C.; Sann, J.; Janek, J.; Chen, L. M.; Klar, P. J.; Hofmann, D. M.; Philipps, J.; Dolcet, P.; Gross, S.; Over, H.; Smarsly, B. M. ChemCatChem 2015, 7, 3738−3747.

(30) Ta, N.; Liu, J.; Chenna, S.; Crozier, P. A.; Li, Y.; Chen, A. L.; Shen, W. J. J. Am. Chem. Soc. 2012, 134, 20585−20588.

(31) Agarwal, S.; Zhu, X.; Hensen, E. J. M.; Mojet, B. L.; Lefferts, L. J. Phys. Chem. C 2015, 119, 12423−12433.

(32) Yang, C. W.; Yu, X. J.; Heissler, S.; Nefedov, A.; Colussi, S.; Llorca, J.; Trovarelli, A.; Wang, Y. M.; Wöll, C. Angew. Chem., Int. Ed. 2017, 56, 375−379.

(33) Huang, W. X. Acc. Chem. Res. 2016, 49, 520−527.

(34) Piumetti, M.; Bensaid, S.; Fino, D.; Russo, N. Appl. Catal., B 2016, 197, 35−46.

(35) Zhang, G. J.; Shen, Z. R.; Liu, M.; Guo, C. H.; Sun, P. C.; Yuan, Z. Y.; Li, B. H.; Ding, D. T.; Chen, T. H. J. Phys. Chem. B 2006, 110, 25782−25790.

(36) Henderson, M. A.; Perkins, C. L.; Engelhard, M. H.; Thevuthasan, S.; Peden, C. H. F. Surf. Sci. 2003, 526, 1−18.

(37) Pfau, A.; Schierbaum, K. D. Surf. Sci. 1994, 321, 71−80.

(38) Gunnarsson, O.; Schonhammer, K. Phys. Rev. B: Condens. Matter Mater. Phys. 1983, 28, 4315−4341.

(39) Suzuki Takehiko Ishii, S.; Sagawa, T. J. Phys. Soc. Jpn. 1974, 37, 1334−1340.

(40) Montemor, M. F.; Simões, A. M.; Carmezim, M. J. Appl. Surf. Sci. 2007, 253, 6922−6931.

(41) Turczyniak, S.; Greluk, M.; Slowik, G.; Gac, W.; Zafeiratos, S.; Machocki, A. ChemCatChem 2017, 9, 782−797.

(42) Mullins, D. R.; Overbury, S. H.; Huntley, D. R. Surf. Sci. 1998, 409, 307−319.

(43) Kotani, A.; Jo, T.; Parlebas, J. C. Adv. Phys. 1988, 37, 37−85.

(44) Le Normand, F.; El Fallah, J.; Hilaire, L.; Légaré, P.; Kotani, A.; Parlebas, J. C. Solid State Commun. 1989, 71, 885−889.

(45) Torrente-Murciano, L.; Gilbank, A.; Puertolas, B.; Garcia, T.; Solsona, B.; Chadwick, D. Appl. Catal., B 2013, 132−133, 116−122.

(46) Wang, L.; Wang, Y. F.; Zhang, Y.; Yu, Y. B.; He, H.; Qin, X. B.; Wang, B. Y. Catal. Sci. Technol. 2016, 6, 4840−4848.

(47) Wang, F.; Li, C. M.; Zhang, X. Y.; Wei, M.; Evans, D. G.; Duan, X. J. Catal. 2015, 329, 177−186.

(48) Trovarelli, A. Catal. Rev.: Sci. Eng. 1996, 38, 439−520.

(49) Campbell, C. T.; Peden, C. H. F. Science 2005, 309, 713−714.

(50) Montini, T.; Melchionna, M.; Monai, M.; Fornasiero, P. Chem. Rev. 2016, 116, 5987−6041.

(51) Capdevila-Cortada, M.; Vile, G.; Teschner, D.; Pérez-Ramírez, J.; Lopez, N. Appl. Catal., B 2016, 197, 299−312.

(52) Idriss, H. Platinum Met. Rev. 2004, 48, 105−115.

(53) Nanda, R.; Sorensen, J. B. AIChE J. 2010, 56, 1116−1126.

(54) Jasinski, P.; Petrovsky, V.; Suzuki, T.; Anderson, H. U. J. Electrochem. Soc. 2005, 152, J27−J32.

(55) Perkins, C. L.; Henderson, M. A.; Peden, C. H. F.; Herman, G. S. J. Vac. Sci. Technol., A 2001, 19, 1942−1946.

(56) Lin, Y. Y.; Wu, Z. L.; Wen, J. G.; Poeppelmeier, K. R.; Marks, L. D. Nano Lett. 2014, 14, 191−196.

(57) Tinoco, M.; Fernandez-Garcia, S.; Lopez-Haro, M.; Hungria, A. B.; Chen, X. W.; Blanco, G.; Perez-Omil, J. A.; Collins, S. E.; Okuno, H.; Calvino, J. J. ACS Catal. 2015, 5, 3504−3513.

(58) Crihan, D.; Knapp, M.; Zweidinger, S.; Lundgren, E.; Weststrate, C. J.; Andersen, J. N.; Seitsonen, A. P.; Over, H. Angew. Chem., Int. Ed. 2008, 47, 2131−2134.

3.2 Publication 2

The stabilizing effect of water and high reaction temperatures on the CeO$_2$-catalyst in the harsh HCl oxidation reaction

Chenwei Li, Franziska Hess, Igor Djerdj, Guangtao Chai, Yu Sun, Yanglong Guo, Bernd M. Smarsly, Herbert Over

The stabilizing effect of water and high reaction temperatures on the CeO$_2$-catalyst in the harsh HCl oxidation reaction

Check for updates

Chenwei Li [a,b], Franziska Hess [b,c], Igor Djerdj [d], Guangtao Chai [a], Yu Sun [a,b], Yanglong Guo [a,*], Bernd M. Smarsly [b,*], Herbert Over [b,*]

[a] Key Laboratory for Advanced Materials, Research Institute of Industrial Catalysis, School of Chemistry and Molecular Engineering, East China University of Science and Technology, Shanghai 200237, PR China
[b] Physikalisch-Chemisches Institut, Justus Liebig University, Heinrich-Buff-Ring 17, 35392 Giessen, Germany
[c] Dept. of Nuclear Science and Engineering, Massachusetts Institute of Technology, 77 Massachusetts Avenue, Cambridge, MA 02139, USA
[d] Department of Chemistry, Josip Juraj Strossmayer University of Osijek, Cara Hadrijana 8/a, HR-31000 Osijek, Croatia

ABSTRACT

We studied the stability of CeO$_2$ nano-cubes with preferentially (1 0 0)-oriented facets in the HCl oxidation reaction (Deacon process) for various reaction temperatures and the addition of small concentrations of water in the gas feed. For a reaction mixture HCl:O$_2$ = 1:2 we find that CeO$_2$ is substantially chlorinated below 380 °C, revealing a low catalytic activity. At 390 °C both the activity and the chlorination degree change abruptly: activity becomes high and chlorination is not detectable by XRD. The experimental results are rationalized by a kinetic model which allows us to study catalyst chlorination as a function of temperature and gas feed composition. The model predicts that chlorination sets in at the inlet of the catalyst bed and propagates then slowly along the catalyst bed towards the reactor outlet to fully chlorinate the CeO$_2$ catalyst bed. This process has been confirmed by a dedicated experiment employing two separate catalyst layers, where only the first layer is shown to be chlorinated while exposed to the Deacon gas feed. Our model attributes the excessive chlorination at the reactor inlet to the absence of H$_2$O in the gas feed, as the formation of H$_2$O by the reaction of HCl with CeO$_2$ is the prevailing driving force for catalyst chlorination. When running the Deacon process at 375 °C, the chlorination of CeO$_2$ nano-cubes is efficiently suppressed by the addition of 1% water to the reaction mixture. This extrinsic stabilization of oxide catalysts towards chlorination by water is a general concept, which may enable the identification of new oxide materials that have previously been ruled out as Deacon catalysts due to their low stability under reaction conditions.

© 2017 Elsevier Inc. All rights reserved.

1. Introduction

With the Deacon process molecular chlorine can be recovered from toxic HCl waste [1,2]. Besides chlorine also water is produced according to the overall reaction $2\,HCl + \frac{1}{2}\,O_2 \rightarrow Cl_2 + H_2O$; $\Delta_r H = -59$ kJ/mol. The original Deacon catalyst [3] was based on CuO/CuCl$_2$ that suffers most notably from low stability due to formation of volatile Cu-chloride species at reaction temperatures above 400 °C. Most other transition metal oxides undergo chlorination under Deacon conditions in a similar fashion and consequently have been ruled out as potential Deacon catalysts [4–6]. The Deacon reaction over CuO/CuCl$_2$ is considered to consist of two

consecutive solid-state reactions of the catalyst material, namely firstly the exothermic chlorination of CuO with the release of the byproduct H$_2$O and secondly an endothermic re-oxidation of the chlorinated catalyst [7–9], during which the desired product Cl$_2$ is released.

Recently, CeO$_2$ was proposed as a stable and active Deacon catalyst [10–14]. Under oxidizing reaction conditions the catalyst is stable, while under HCl-rich reaction conditions the oxide can readily transform to CeCl$_3$·nH$_2$O [13]. Since catalyst stability is a key issue in the Deacon process, chlorination of CeO$_2$ was studied quite intensively by Prompt Gamma-Ray Activation Analysis (PGAA) [15,16], and a correlation between structure and activity was disclosed: the higher the chlorination degree of CeO$_2$ the lower the catalytic activity. The corrosion of CeO$_2$-based catalysts is sensitive to how the plug flow reactor is shut down. In case the temperature is lowered under reaction conditions corrosion in the

form of chlorination of CeO_2 was found to be much more severe than in case where the reactor was cooled down in an inert gas atmosphere [17]. In addition, the stability of CeO_2 depends also critically on the surface orientation, with CeO_2 nano-rods preferentially oriented in (1 1 0) direction, turning out to be the more stable in comparison to cubes and octahedrons being oriented in (1 0 0) and (1 1 1) direction, respectively [18].

The present study addresses the stability of CeO_2 under Deacon conditions with the goal to rationalize and predict chlorination as a function of reactor parameters by combining experiments with a simple theoretical model of catalyst chlorination. To visualize morphological changes indicating (reversible) phase transformations, we employ shape-controlled CeO_2 nano-cubes [19]. These particles expose preferentially {1 0 0} facets of CeO_2, while the actual surface termination due to reconstruction is largely unknown [20] and affected by entropy contributions [21]. These particles feature sharp and well-defined edges that are extremely prone to transformation, resulting in pronounced rounding-off when exposed to the corrosive Deacon reactants. With transmission electron microscopy (TEM) we follow the degradation of single CeO_2 nanoparticles after Deacon reaction for various reaction conditions. Since the resulting hydrated Ce-trichloride is crystalline, the degree of chlorination can be quantified by Rietveld analyses of X-ray diffraction (XRD) data of the catalyst after reaction. The key finding is that the leading driving force for catalyst chlorination at dry conditions and temperatures typically employed in the Deacon is the formation of H_2O that is associated with the reaction of HCl with the oxide. Adding a small amount of H_2O to the gas stream essentially removes the driving force for chlorination, resulting in enhanced catalyst activity due to complete suppression of $CeCl_3$ formation.

2. Experimental section

The CeO_2 nano-cubes were prepared using a previously published hydrothermal method [19,22]. The Ce-containing solution (0.434 g $Ce(NO_3)_3 \cdot 6H_2O$ in 2.5 mL of deionized water) was added dropwise into a NaOH solution (4.8 g NaOH in 17.5 mL of deionized water) placed in Teflon liner under stirring for 30 min at room temperature. The Teflon liner was then tightly sealed in a stainless steel autoclave, keeping the temperature at 100 °C for 24 h. Next, the fresh precipitates were separated by centrifugation, subsequently washed by deionized water and ethanol several times, followed by drying at 80 °C in air overnight. Finally, the samples were calcined at 600 °C (heating rate 5 K/min) for 6 h in a muffle oven. The calcination temperature of 600 °C was chosen high enough to suppress further temperature-induced sintering of the particles during the Deacon reaction.

The catalytic tests of the CeO_2 nano-cubes were carried out in a fixed bed flow reactor at ambient pressure. The homemade design of the reactor set up [23] includes the gas supply, the quartz tube reactor, heated by the furnace, and the UV/Vis spectrometer for analytic chlorine quantification. The flow of gases, supplied by AirLiquide (HCl 4.5, O_2 4.8 and Ar 5.0), was controlled by digital mass flow controllers (MKS Instruments 1179B). Prior to feeding into the reactor, Ar was dried using a water absorption cartridge (ALPHAGAZ™ purifier H_2O-free, AirLiquide). The reaction gas feed was controlled at the ratio of Ar:HCl:O_2 = 7:1:2 and the total volumetric flow rate was set to 15 cm³STPmin⁻¹ (sccm). For the catalytic tests, typically 20 mg ceria material was supported between quartz wool wads in the reactor tube. The furnace was heated to 250–430 °C with a rate of 10 K/min and kept for 1–24 h under the reactant stream. The catalyst was only exposed to the O_2 and HCl reaction feeds after the intended catalyst bed temperature had been reached in Ar atmosphere. The product composition was analyzed in a Z-shaped flow cell, combined with

a fiber-optic UV–Vis spectrometer (Ocean Optics USB4000 with a DH-2000-BAL light source). The absorbance at a wavelength of λ_{max} = 329 nm (absorption maximum of chlorine) is proportional to the chlorine space-time yield (STY).

The catalytic test with 1% of water of the CeO_2 nano-cubes was conducted at 350 °C and 375 °C. Moreover, an additional flow of Ar, which passes through deionized water (denoted as 'Ar (humid)', was introduced into the reactor. The reaction feeds were controlled at the ratio of Ar (humid): Ar: HCl: O_2 = 5:2:1:2 so that 1% water was introduced into the reactant stream by its saturated vapor pressure.

Structural information of the catalyst is gained by X-ray diffraction (XRD) which is conducted in Θ-2Θ geometry on a Panalytical X'Pert PRO diffractometer with a Cu K_α source (40 kV, 40 mA). Rietveld analysis was carried out by using the FullProf program (Version 2.05).

Transmission electron microscopy (TEM) was performed with a FEI TF20 electron microscope operated at 200 kV. The sample was ultrasonically suspended in the ethanol solvent, and one or two droplets of this slurry were deposited on a copper grid.

3. Results and discussion

In Fig. 1 Deacon experiments on the stability of CeO_2 against bulk $CeCl_3$ formation at various temperatures with fixed gas feed
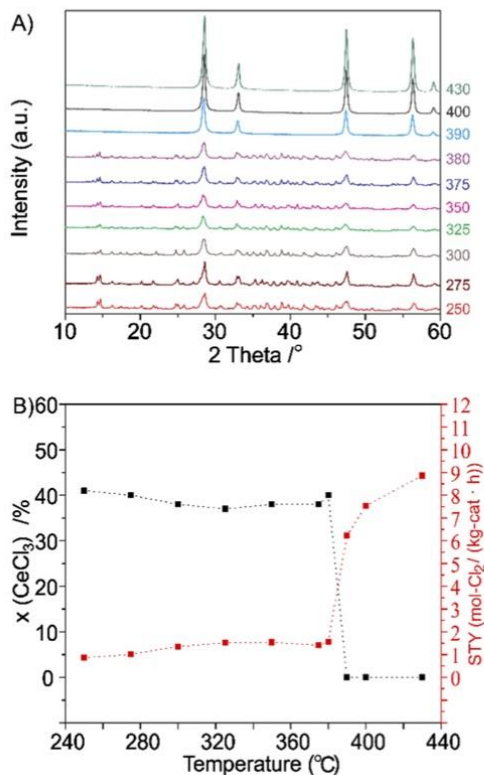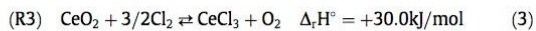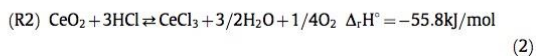

Fig. 1. (A) XRD scans after 24-hour Deacon reaction under different temperature of CeO_2 nano-cubes. (B) Chlorination degree $x(CeCl_3)$ and steady Space-time-yield (STY) versus reaction temperature at a gas feed of Ar:HCl:O_2 = 7:1:2 (so-called mild condition) and a flow rate of 15 sccm.

in a flow reactor reveal a surprising behavior. The catalyst was held 24 h on reaction stream until steady state was accomplished. In Fig. 1a we present XRD data for increasing reaction temperatures from 250 to 430 °C. Below 380 °C bulk-chlorination of CeO_2 is clearly detectable in the two-theta scans, indicating the formation of crystalline $CeCl_3 \cdot 6H_2O$. From Rietveld analysis, we derived the concentration of $CeCl_3 \cdot 6H_2O$ to be 38% ± 3% independent of the reaction temperature up to 380 °C (cf. Fig. 1b). In previous studies the oxychlorination of CeO_2 has shown to be an important process to stabilize Ce^{3+} [24]. However, our Rietveld analysis clearly excludes the formation of CeOCl consistent with the instability of CeOCl under HCl oxidation reaction conditions [25]. At 390 °C (and above) bulk chlorination is abruptly suppressed. Consistent with suppressed chlorination, the activity increases steeply at temperatures higher that 390 °C. Keeping the same HCl:O_2 ratio of 1:2 throughout, the activity is strictly correlated to the degree of bulk-chlorination: the lower the degree of chlorination the higher the activity.

These stability results are paralleled by activity measurements in terms of space time yield (STY) at steady state in the temperature range of 250 °C to 430 °C as summarized in Fig. 1b. The activity is very low in the temperature range from 250 °C to 380 °C due to chlorination of CeO_2. The residual activity slightly increases with temperature and reflects the Deacon activity of $CeCl_3 \cdot nH_2O$. We may recall the initial-state activity of the CeO_2 samples is considerably higher and dies out rapidly as shown in Fig. S1. The STY curves in Fig. S1 allow us to follow the chlorination rate of CeO_2 *operando* by the initially linear decrease of catalyst activity as a function of time, which stabilizes to a constant steady-state level when chlorination terminates. The chlorination rate of CeO_2, reflected by the slope in the linear segment, decreases with temperature at 300 °C and above. When conducting these temperature-dependent chlorination experiments, it is important to wait long enough to achieve steady state reaction conditions: if the reaction time is too short (e.g. 1 h) then bulk-chlorination of CeO_2 is not observed at higher temperatures for kinetic reasons (cf. Fig. S2). Since the total chlorination degree is only 38%, we presume core-shell particles comprising of a $CeCl_3$ shell and a CeO_2 core.

As evident from Fig. 1b, chlorination occurs only at temperatures lower than 380 °C under the conditions employed in our experiments. To rationalize these results, we first consider possible reactions by which chlorination of CeO_2 can occur including their reaction enthalpies at standard conditions (298 K, 10^5 Pa):

(R1) $CeO_2 + 4HCl \rightleftharpoons CeCl_3 + 2H_2O + 1/2Cl_2$ $\Delta_r H° = -84.4 \text{kJ/mol}$ (1)

(R2) $CeO_2 + 3HCl \rightleftharpoons CeCl_3 + 3/2H_2O + 1/4O_2$ $\Delta_r H° = -55.8 \text{kJ/mol}$ (2)

(R3) $CeO_2 + 3/2Cl_2 \rightleftharpoons CeCl_3 + O_2$ $\Delta_r H° = +30.0 \text{kJ/mol}$ (3)

From the free reaction enthalpies, we conclude that chlorination must proceed via reactions (R1) and (R2), while reaction (R3) should dominate the re-oxidation process. The thermodynamic parameters employed for these calculations are listed in

the ESI. Both (R1) and (R2) are exothermic so that increasing the temperature shifts both these equilibria to the CeO_2 side, consistent with the experimentally observed temperature dependency of chlorination depicted in Fig. 1b. Reaction (R3) is endothermic but also endotropic so that its equilibrium is never on the product side in the temperature range studied here, and it will almost exclusively contribute to re-oxidation of the catalyst.

The transition temperature found in our experiments strongly depends on the reaction parameters, and thus gives no direct information about the thermodynamics of these coupled reactions. In order to understand the influence of reaction parameters on the catalyst chlorination, we established a simple kinetic model employing the chlorination/dechlorination reactions (R1)-(R3) shown in Fig. 2a. The full details of the model are given in the ESI, but the approach and main results are described briefly in the following.

CeO_2 can be transformed into $CeCl_3$ by three different reaction paths, each featuring different reaction products and educts. Since the reactions depend on gas phase species, we expect different reactions to dominate the chlorination and dechlorination, depending on the reaction temperature, $p(O_2)/p(HCl)$ ratio, and the conversion level of the Deacon reaction. The chlorination reaction (R1) (which is the most favorable one under standard conditions) is exothermic and exotropic under standard conditions (reaction enthalpies and entropies are provided in the ESI), so that the equilibrium is on the $CeCl_3$ side at low temperature and shifts to the CeO_2 side with increasing temperature. The transition between these regimes can be inferred by the zero-point of the Gibbs enthalpy, which occurs around 230 °C under standard conditions. However, the conditions in our reactor are far away from standard conditions, most notably due to the absence of H_2O and Cl_2 at low conversion, and furthermore, reactions (R2) and (R3) and their backward reactions can also occur. For example, the forward reaction of (R1) could be combined with the backward reaction of (R3) to give the Mars-van-Krevelen-type Deacon reaction shown in Fig. 2b. We devise a steady-state kinetic model for the coupling of (R1)-(R3), using the equilibrium constants (K1)-(K3) and K_{Deacon}, which can be readily calculated from thermodynamic data. The model requires two additional parameters which are fitted to the experimental results in Fig. 1B as detailed in Section S 2.3 in the ESI. We emphasize, however, that none of the qualitative aspects discussed here, such as the influence of temperature, and reactant gas feed, are affected by the choice of these parameters. Based on the final parameters compiled in Table S2 this model allows for detailed modeling of chlorination along the catalyst bed, taking into account temperature and reactant gas feed. For example, the computed degree of chlorination of CeO_2 is shown as a function of the reaction temperature in Fig. S5. We observe a smooth transition from $CeCl_3$ towards CeO_2 in the temperature region of 250–430 °C that agrees qualitatively with the experimental data in Fig. 1B. The actual temperature dependence of the chlorination degree is discussed in more detail in Section S 2.5 of the supporting material.

Another important feature of the reaction system is that at the inlet of the catalyst bed, neither water nor chlorine is present in
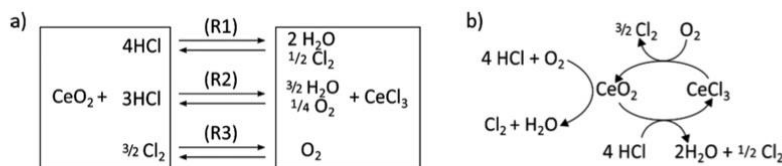

Fig. 2. (a) Coupling of chlorination/dechlorination reactions (R1)-(R3). (b) Coupling of solid-state reactions (R1) and (R3) with the HCl oxidation catalyzed by pure CeO_2.

47

appreciable concentrations in the reaction mixture, which has consequences for the chlorination process of CeO_2. Assuming that H_2O and Cl_2 are present as impurities (10 ppm), we can estimate the free reaction enthalpy. Under standard conditions $\Delta_r G^0(R1) = +29.8$ kJ/mol, but for $a(H_2O) = a(Cl_2) = 10^{-5}$, $\Delta_r G(R1) = -71.6$ kJ/mol. This means that there is a strong driving force to form water at the reactor inlet. This drives in turn the catalyst chlorination, a process that diminishes rapidly along the catalyst bed. Assuming a conversion of 1.5%, for instance, the free reaction enthalpy at the reactor outlet is $\Delta_r G(R1) = +52.1$ kJ/mol, thus the chlorination equilibrium is far on the CeO_2 side. A more detailed discussion of these processes is given in the ESI. Assuming that the HCl conversion increases linearly along the catalyst bed, we can roughly estimate the chlorination of CeO_2 along the catalyst bed as summarized in Fig. 3. The total chlorination degree is obtained by integrating along the length of the catalyst bed up to the experimentally measured conversion degree. Under dry conditions (black curve in Fig. 3), 85% of the catalyst are chlorinated close to the reactor inlet. Along the catalyst bed the chlorination degree decreases to 40% at the reactor outlet in case the reactor operates at 5% conversion. From our simulation, we infer that the chlorination decreases mainly due to the formation of H_2O in the Deacon reaction, which substantially reduces the driving force for (R1) and (R2), as discussed above.

Our model predicts therefore that the chlorination degree should be higher at the reactor inlet than at the outlet. This finding motivated us to design a dedicated experiment in which the CeO_2 catalyst bed is split into two segments separated by quartz wool. The first part of the catalyst should be prone to chlorination (due to missing water), while the second part should be stabilized by the water formed in the first catalyst layer. Indeed, this behavior is experimentally observed. XRD data in Fig. S3 indicate clearly that CeO_2 is chlorinated in the first layer for mild HCl oxidation conditions at 350 °C, while the second layer does not undergo chlorination, thus confirming a fundamental feature of our chlorination model.

Similarly, we can computationally examine the effect of adding water to the gas feed on the chlorination (red curve in Fig. 3). The model predicts that just 1% of H_2O added to the gas feed will almost entirely suppress catalyst chlorination, irrespective of the Deacon conversion in the reactor. Humid conditions are typically avoided in Deacon reactors due to enhanced metal (tubing) corrosion by HCl. However, we find the opposite to happen for the CeO_2 catalyst because H_2O is the secondary product formed when an oxide is chlorinated by HCl, and H_2O formation is the dominating driving force for chlorination under dry conditions.

To verify the proposed catalyst stabilization by water directly, we introduced purposely 1% water into the reaction mixture and
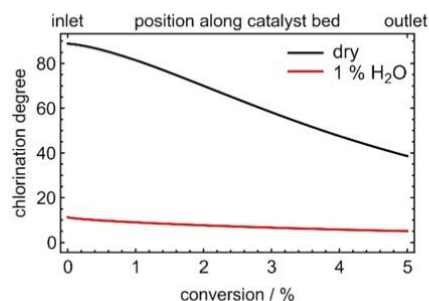
compared stability and activity with those of the same catalyst but without water. The experiments are compiled in Figs. 4 and S4. The initial catalyst activity (Fig. 4A) is slightly reduced by water compared to the water-free measurement (black curve). In the steady state, the overall activity under humid conditions surpasses the activity under dry conditions. However, the sample in H_2O-free environment shows the typical deactivation due to chlorination, while the activity stabilizes without discernible chlorination under humid conditions. This conclusion is corroborated by XRD experiments (cf. Fig. 4B). While the catalyst undergoes massive chlorination without water in the reaction mixture, no $CeCl_3$ is detectable under humid conditions. This behavior can also be visualized by employing TEM (Fig. 4C,D). Without water in the reaction mixture, severe morphological changes of the CeO_2 nano-cubes appear in that the smooth facets of the cubes become roughened and the particles starts to sinter. In addition, shapeless material is formed that likely is assigned to $CeCl_3$. From TEM it seems that the particles are largely covered by $CeCl_3$, possibly blocking the contact between the gas phase and the CeO_2 surface, thus suppressing chlorination beyond 40%. The addition of 1% of water stabilizes the catalyst to a point where even the edges that usually undergo rounding-off under Deacon conditions first [18] remain sharp. This suggests that the chlorination itself (forward reaction (R1)-(R3)) seems to be suppressed and no changes in catalyst particle morphology are discerned from the TEM images, rather than simply promoting re-oxidation (backward reactions (R1)-(R3)) which would round off the edges regardless of final chlorination degree.

From these results, we expect that the chlorination of CeO_2 occurs predominantly at the reactor inlet (where no or very little water is present under dry conditions). However, chlorination can affect the entire catalyst bed, as $CeCl_3$ formed by chlorination of CeO_2 is much less active than CeO_2 in the Deacon process, resulting in reduced water production the chlorinated layer. The chlorination thus propagates slowly along the catalyst bed towards the outlet.

4. Conclusions

Variation of the reaction temperature has a complex impact on the activity and the stability of the CeO_2 catalyst in the HCl oxidation reaction that needs to be taken into account in the implementation of the technical Deacon process. Higher temperatures will increase the conversion first for kinetic reasons but at higher temperatures the equilibrium conversion decreases because the Deacon reaction is exothermal with an equilibrium constant close to 1. However, the chosen reaction temperature has equally strong influence on the stability of the CeO_2 catalyst. For a reaction mixture of HCl:O_2 = 1:2 above 390 °C CeO_2 is stable and active, while it undergoes severe chlorination and deactivation at temperatures lower than 380 °C. The optimum temperature window (depending on the reaction feed) is 400–430 °C combining high stability with high catalytic activity and sufficiently high equilibrium conversion.

The stability findings presented in this paper will have strong implications on the performance and the operation of a Deacon flow reactor employing CeO_2-based catalysts:

(i) Chlorination takes place preferentially at the inlet of the catalyst bed (when no or little water is present) and may propagate slowly along the catalyst bed towards the reactor outlet.
(ii) One should never switch off the reactor by reducing the reaction temperature under the reaction mixture, because chlorination of CeO_2 is thermodynamically favored at low temperatures.
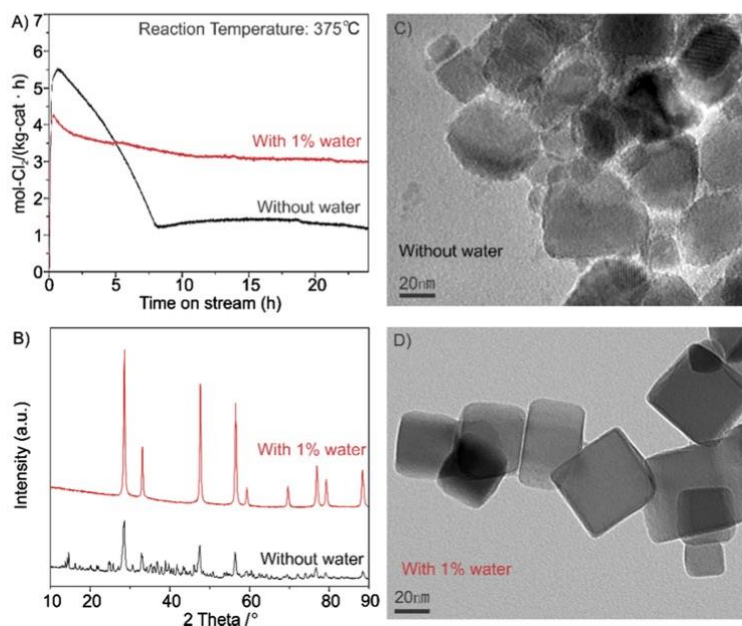

Fig. 3. Chlorination degree of CeO_2 along the catalyst bed (reflected by conversion) at 350 °C under mild conditions without and with 1% water, as modeled by our non-equilibrium approach.

48

Fig. 4. (A) Space time yield (STY) of molecular chlorine in the HCl oxidation reaction using CeO_2 nano-cubes under different feed gas (without water and with 1% water) under mild conditions at 375 °C. (B) XRD scans of the CeO_2 nano-cubes after mild condition with different feed gas (without water and with 1% water). (C) and (D) TEM images of CeO_2 nano-cubes after mild condition with different feed gas (without water and with 1% water).

(iii) Little water in the reaction feed improves the resistance of CeO_2 based catalysts against bulk chlorination with only little degradation of the activity.

The stabilization of oxides by H_2O in the Deacon reaction should prevail for other oxides as well, as H_2O formation upon chlorination by HCl is a common feature of oxide chlorination processes. Previous catalyst screenings have ruled out materials that form volatile chlorides as potential Deacon catalysts due to permanent catalyst deactivation, similar to the $CuO/CuCl_2$ system. The extrinsic suppression of chlorination by H_2O addition may stabilize some of these materials that have previously been ruled out by stability considerations, possibly leading to the discovery of new active Deacon catalysts.

We are convinced that these considerations and the presented theoretical concept may also help to tackle stability problems of other heterogeneously catalyzed oxidation reactions over oxide catalysts, in particular partial oxidation reactions, where water is formed as the byproduct. The addition of the byproduct to the reaction mixture may help to stabilize the catalyst and higher reaction temperatures may push the catalyst towards a stable regime.

Acknowledgement

Appendix A. Supplementary material

Supplementary data associated with this article can be found, in the online version, at https://doi.org/10.1016/j.jcat.2017.11.019.

References

[1] J. Pérez-Ramírez, C. Mondelli, T. Schmidt, O.F.K. Schlüter, A. Wolf, L. Mleczko, T. Dreier, Energy Environ. Sci. 4 (2011) 4786–4799.
[2] H. Over, R. Schomäcker, ACS Catal. 3 (2013) 1034–1046.
[3] H. Deacon, U.S. Patent 165 (1875) 6802.
[4] M. Hammes, M. Valtchev, M. Roth, K. Stöwe, W. Maier, Appl. Catal. B-Environ. 132–133 (2013) 389–400.
[5] M. Moser, C. Mondelli, A.P. Amrute, A. Tazawa, D. Teschner, M.E. Schuster, A. Klein-Hoffman, N. López, T. Schmidt, J. Pérez-Ramírez, ACS Catal. 2 (2013) 2813–2822.
[6] A.P. Amrute, F. Krumeich, C. Mondelli, J. Pérez-Ramírez, Chemical Science. 4 (2013) 2209–2217.
[7] M.W.M. Hisham, S.W. Benson, J. Phys. Chem. 99 (1995) 6194–6198.
[8] J.A. Allen, J. Appl. Chem (London) 12 (1962) 406.
[9] K.K. Feng, C.W. Li, Y.L. Guo, W.C. Zhan, B.Q. Ma, B.W. Chen, M.Q. Yuan, G.Z. Lu, Appl. Catal. B: Environ 164 (2015) 483–487.
[10] A. Hagemeyer, P. Trübenbach, C.W. Rieker, M. Wünsch, O. Watzenberger, EP Patent 0761594-A1, assigned to BASF Aktierngesellschaft, 1997.
[11] G. Lee, S.W. Lee, I. Sohn, Y.C. Kwon, J. Song, C.-S. Son, WO2009035234-A2, assigned to Hanwha chemical corporation, 2009.
[12] A. Wolf, L. Mleczko, O.F. Schlüter, S. Schubert, WO2010133313-A1, assigned to Bayer Material, Science (2010).
[13] A.P. Amrute, C. Mondelli, M. Moser, G. Novell-Leruth, N. López, D. Rosenthal, R. Farra, M.E. Schuster, D. Schuster, T. Schmidt, J. Pérez-Ramírez, J. Catal. 286 (2012) 287–297.
[14] M. Moser, C. Mondelli, T. Schmidt, F. Girgsdies, M.E. Schuster, R. Farra, L. Szentmiklósi, D. Teschner, J. Pérez-Ramírez, Appl. Catal. B 132–133 (2013) 123–131.

[15] R. Farra, M. Eichelbaum, R. Schlögl, L. Szentmiklósi, T. Schmidt, A.P. Amrute, C. Mondelli, J. Pérez-Ramírez, D. Teschner, J. Catal. 297 (2013) 119–127.

[16] R. Farra, M. Garcia-Melchor, M. Eichelbaum, M. Hashagen, W. Frandsen, J. Allan, F. Girgsdies, L. Szentmiklósi, N. Lopez, D. Teschner, Promoted Ceria: a strucutral, catalytic, and computational study, ACS Catal. 3 (2013) 2256–2268.

[17] M. Möller, H. Over, B.M. Smarsly, N. Tarabanko, S. Urban, Catal. Tod. 253 (2015) 2017–2218.

[18] C.W. Li, Y. Sun, I. Djerdj, P. Voepel, C. Sack, T. Weller, R. Ellinghaus, J. Sann, Y.L. Guo, B. Smarsly, H. Over, ACS Catal. 7 (2017) 6453–6463.

[19] H.X. Mai, L.D. Sun, Y.W. Zhang, R. Si, W. Feng, H.P. Zhang, H.C. Liu, C.H. Yan, J. Phys. Chem. B. 109 (2005) 24380–24385.

[20] D.R. Mullins, Surf. Sci. Rep. 70 (2015) 42–85.

[21] M. Capdevila-Cordata, N. López, Nat. Mat. 16 (2017) 328–334.

[22] J. He, T. Xu, Z. Wang, Q. Zhang, W. Deng, Y. Wang, Angew. Chem. Int. Ed. 51 (2012) 2438–2442.

[23] Ch. Kanzler, S. Urban, K. Zalewska-Wierzbicka, F. Hess, S.F. Rohrlack, C. Wessel, R. Ostermann, J.P. Hofmann, B.M. Smarsly, H. Over, Chem Cat. Chem. 5 (2013) 2621–2626.

[24] J. C. Conesa, M. Fernandez-Garcia, A. Martinez-Arias, in Catalysis by Ceria and related Materials, ed. By A. Trovarelli, 2002, 169-216.

[25] R. Farra, F. Girgsdies, W. Frandsen, M. Hashagen, R. Schlögl, D. Teschner, Catal. Lett. 143 (2013) 1012–1217.

3.3 Article 3 (to be submitted)

Catalytic HCl Oxidation Reaction:
Stabilizing Effect of Zr-Doping on CeO$_2$ Nano-Rods

Chenwei Li, Yu Sun, Igor Djerdj, Joachim Sann, Pascal Voepel, Pascal Cop, Felix M Badaczewski, Yanglong Guo, Bernd M. Smarsly, Herbert Over

Catalytic HCl Oxidation Reaction:

Stabilizing Effect of Zr-Doping on CeO$_2$ Nano-Rods

Chenwei Li[a,b], Yu Sun[a,b], Igor Djerdj[c], Joachim Sann[b], Pascal Voepel[b], Pascal Cop[b], Felix M Badaczewski[b], Yanglong Guo[a,*], Bernd M. Smarsly[b,*], Herbert Over[b,*]

a) Key Laboratory for Advanced Materials, Research Institute of Industrial Catalysis, School of Chemistry and Molecular Engineering, East China University of Science and Technology, Shanghai 200237, PR China
b) Physikalisch-Chemisches Institut, Justus Liebig University, Heinrich-Buff-Ring 17, 35392 Giessen, Germany
c) Department of Chemistry, J. J. Strossmayer University of Osijek, Ulica cara Hadrijana 8/a, HR-31000 Osijek, Croatia

* *Corresponding authors:* E-mail: herbert.over@phys.chemie.uni-giessen.de;
Bernd.Smarsly@phys.Chemie.uni-giessen.de; ylguo@ecust.edu.cn

Abstract:

Mixed Ce$_{1-x}$Zr$_x$O$_2$ nano-rod particles with Zr doping levels of up to 20% were exposed to Deacon reaction mixtures with high HCl concentration at a reaction temperature of 430°C and post analyzed by x-ray diffraction (XRD), transmission electron microscopy (TEM), and x-ray photoelectron spectroscopy (XPS). Pure CeO$_2$ nano-rods are shown to suffer from bulk-chlorination of the catalyst for reaction mixtures HCl:O$_2$ >2 that is accompanied by dramatic activity losses. CeCl$_3$x6H$_2$O is formed via nucleation and growth forming large single crystalline particles. For a reaction mixture of HCl:O$_2$=2.5:1, already 5% Zr doping suffices to stabilize Ce$_{1-x}$Zr$_x$O$_2$ nano-rods against bulk chlorination. Yet, the chlorine concentration of Ce$_{1-x}$Zr$_x$O$_2$ nano-rods as quantified by XPS is too high to be solely ascribed to on-surface chlorine. The incorporation of Cl into the surface-near region is corroborated by XPS experiments after oxygen plasma treatment. For even more harsh reaction conditions HCl:O$_2$=3:1 none of the Ce$_{1-x}$Zr$_x$O$_2$ nano-rods were stable at 430°C. However, reaction temperature of 500°C enables even CeO$_2$ nano-rods to be stable under such harsh reaction conditions.

Keywords: Deacon process, stability, CeO$_2$, nano-rods, Zr-doping

1. Introduction

The heterogeneously catalyzed gas-phase oxidation of HCl to Cl_2 (Deacon process) is an ideal and energy-efficient way to recycle the HCl waste [1, 2], which is an inevitable by-product generated in chlorine-related chemical process such as polyurethanes, polycarbonates, and chlorinated polypropylene. However, severe stability issues of the catalysts had prevented the industrialization for 140 years until 1999 when Sumitomo Chemical developed a catalyst based on RuO_2 supported on rutile-TiO_2, featuring remarkably high activity combined with long-term stability [3]. Nevertheless, the high and fluctuating market price of ruthenium may limit large-scale application of the Sumitomo process calling for other cost-effective catalyst to replace the RuO_2-based catalysts [4-6].

CeO_2 has been proposed as a promising catalyst material for the HCl oxidation, and it was suggested that oxygen storage capacity (OSC) and catalytic activity are interrelated [7]. However, CeO_2 suffers from bulk chlorination under harsh reaction condition (HCl excess) at 430℃ accompanied by a loss of catalytic activity. Farra et al. found with Prompt Gamma-Ray Activation Analysis (PGAA) that chlorination of CeO_2 is correlated with catalytic activity: the more the $CeCl_3$ formed during the Deacon reaction the lower the reactivity [8, 9]. Recently, it was found that the catalytic stability of pure CeO_2 in the Deacon reaction against chlorination depends sensitively on the exposed facets of the particles. The highest stability against bulk chlorination was encountered with (110) facets preferentially exposed by nano-rods [10].

It is well-documented that incorporating isovalent metal cations, such as Zr^{4+}, into the CeO_2 lattice could strongly facilitate its redox properties and the exchange of oxygen [11-14]. Zr^{4+} doping has also shown to be a feasible strategy to improve the catalytic stability in the Deacon process [9, 15, 16]. For polycrystalline mixed oxide $Ce_{1-x}Zr_xO_2$ nanofibers [15], 20% Zr doping is required to stabilize the fiber structure on the mesoscale, while 10% of Zr suffices already to prevent bulk chlorination according to XRD data.

Previously Zr doped CeO_2 single-crystalline nano-rods were successfully synthesized for Zr concentration up to 20% and applied to various catalytic reactions, including styrene epoxidation [17], CO oxidation [18], catalytic reduction of NO [14], and ethanol reforming reaction [19].

To deepen our microscopic understanding on the stabilizing effect of Zr^{4+} we need to control the morphology and the exposed facets of single crystalline $Ce_{1-x}Zr_xO_2$ particles. In doing so, we synthesized $Ce_{1-x}Zr_xO_2$ nano-rods (x=0-0. 2) by a hydrothermal method and investigated them in

the Deacon reaction under various reaction conditions, i.e., different ratio of HCl to O_2 in feed gas and reaction temperature. Both Oxygen storage capacity (OSC) and complete oxygen storage capacity (OSCc) are evaluated for fresh materials and correlated with the catalytic activity. X-ray diffraction (XRD), X-ray photoelectron spectroscopy (XPS), and transmission electron microscopy (TEM) are employed for the catalysts characterization before and after Deacon reaction in order to study the changes of the nano-rods in terms of crystallinity, composition, and morphology and correlate them to the catalytic activity.

2. Experimental Details

$Ce_{1-x}Zr_xO_2$ nano-rods were synthesized by a previously published hydrothermal method [20, 21]. Take $Ce_{0.8}Zr_{0.2}O_2$ nano-rods as an example. The mixed Ce/Zr solution (0.8 mmol $Ce(NO_3)_3*6H_2O$+0.2mmol $ZrO(NO_3)_3*nH_2O$ +2.5 mL deionized water) was first dropped into a NaOH solution (4.8 g NaOH+17.5mL deionized water) placed in Teflon liner and stirred for 30 minutes. The Teflon liner was then placed inside the autoclave keeping the temperature at 100°C for 24h. Next, the precipitates were separated by centrifugation and subsequently washed by deionized water and ethanol several times, followed by drying at 80°C in air overnight. Finally, the samples were calcined at 600°C for 6 h in a muffle oven (heating rate of 5K/min). The calcination temperature of 600°C was chosen to be high enough to suppress the further temperature-induced sintering of the particles during the Deacon reaction.

Transmission electron microscopy (TEM) was performed on a Philipps CM30 instrument operated at 300 kV. Copper mesh grids were used for the sample preparation. The sample was ultrasonically suspended in the ethanol solvent, and one or two droplets of this slurry were deposited on a copper grid.

The activity data were normalized to the surface area, measured by N_2 and krypton physisorption (BET) (AUTOSORB-6; Quantachrome, Boynton Beach, USA) at 77 K.

Structural information of the catalyst is gained by X-ray diffraction (XRD) which is conducted in Θ-2Θ geometry on a Panalytical X'Pert PRO diffractometer with a Cu K_α source (40 kV, 40 mA). Rietveld analysis was carried out by using the FullProf program (Version 2.05).

X-ray photoemission spectroscopy (XPS) experiments (PHI VersaProbe II) were performed with a photon energy of 1486.6 eV (monochromatized Al-K_α line) and the x-ray spot size of ~200 µm with an excitation power of ~50 W to quantify the concentration of Zr, Ce and Cl in the near-

surface region of the nano-rod particles. For quantifying the Zr surface concentration the Zr3d spectrum is referenced against the Ce4d rather than to Ce3d spectrum to allow for similar kinetic energies of both emitted photoelectrons (Zr3d, Ce3d). Typical error bars for quantification data of concentration ratios are 10% relative. Charging of the sample was compensated by a flow of electrons with energies of about 1 eV and Ar^+ ions of about 10 eV. The survey spectra were taken with an analyzer pass energy of 93.9 eV and a step size of 0.8 eV while the detail spectra were acquired with a pass energy of 23.5 eV and a step size of 0.2 eV. The chamber pressure was ~10^{-6} Pa during the measurement and all spectra were taken at room temperature. The XPS data were analyzed with CasaXPS Version 2.3.17. For some samples a plasma cleaning procedure (GV10x Downstream Asher from ibss Group) was applied, for which the samples were exposed to an air plasma for 20 minutes. The plasma is created by an inductively coupled RF field (75 W).

The catalytic tests of $Ce_{1-x}Zr_xO_2$ nano-rods were conducted in a fixed bed flow reactor at ambient pressure. The homemade design of reactor set up [22] includes the gas supply, the quartz tube reactor, heated by the furnace, and the UV/Vis spectrometer for analytic chlorine quantification. The flow of gases, supplied by AirLiquide (HCl 4.5, O_2 4.8 and Ar 5.0), were controlled by digital mass flow controllers (MKS Instruments 1179B). Prior to feeding into the reactor, Ar was dried using a water absorption cartridge (ALPHAGAZ^{TM} purifier H_2O-free, AirLiquide).The reaction temperature is computer-controlled. The product composition was analyzed in a Z-shaped flow cell, combined with a fiber-optic UV–Vis spectrometer (Ocean Optics USB4000 with a DH-2000-BAL light source). The absorbance at a wavelength of λ_{max} = 329 nm (absorption maximum of chlorine) is proportional to the chlorine space time yield (STY) and can be quantified by calibration against KI titration. The argon balanced reaction feeds contained 10 vol% O_2 and varying HCl contents from 20 vol.%, 25 vol.% to 30 vol.% balanced by Ar. The total volumetric flow rate for the reaction was set to 15 $cm^3STPmin^{-1}$ (sccm). For the catalytic tests, typically 20 mg ceria material was supported between quartz wool wads in the reactor tube. The furnace was heated to mostly 430°C (and once 500°C) with a rate of 10 K/min and held for 24 h under reactant stream. The catalyst was only exposed to the O_2 and HCl mixture after the reaction temperature had been reached in Ar atmosphere.

The oxygen storage capacity (OSC) reactor is a stainless steel tube (i.d. 4 mm, length 60 mm) connected to the rest of equipment by stainless steel leads (i.d. 1.6 mm) via Swagelok tube fittings [23, 24]. The OSC reactor was heated to 430°C (at the rate of 10 K/min); this temperature

was chosen to compare OCS/OCSc with activity data at the same temperature. Carbon monoxide (Praxair, quality 4.7) was used as the reducing agent. Typically, 25mg dried catalyst sample was loaded into the reactor, supported between quartz wool wads. To determine the plain oxygen storage capacity (OSC), i.e. the most active oxygen species in the near-surface region of the sample, the stream selector was switched to CO for 2 s (0.067 mL STP of CO), then for 80 s pure Ar was fed, and the stream selector was switched to O_2 for 2 s (0.067 mL STP of O_2). The amount of adsorbed oxygen corresponded to the OSC. To determine complete oxygen storage capacity (OSCc) nine sequential CO pulses 10 s each (0.33 mL STP of CO each) were applied, separated by 60 s when pure Ar was fed. Subsequently, five 2 s pulses of oxygen were fed, separated by 80 s periods when only Ar was fed. The total amount of oxygen absorbed defines the OSCc that approaches oxygen storage capacity of the bulk nano-rod.

3. Results and Discussion

3.1 Characterization of the as-prepared catalysts

In **Figure 1** we show XRD patterns of freshly prepared $Ce_{1-x}Zr_xO_2$ nano-rods for various Zr concentrations. The diffraction peaks of all the catalysts belong to the cubic fluorite structure of CeO_2 (JCPDS NO. 34-0394). In none of the samples XRD peaks indexed to ZrO_2 are detected, even for doping concentration of Zr^{4+} reaching 20 mol%, indicating phase-pure solid solution of $Ce_{1-x}Zr_xO_2$. As shown in the inset of **Figure 1**, the (331) diffraction peak gradually shifts towards higher diffraction angles with increasing Zr^{4+} concentration, reflecting the known lattice contraction by Zr incorporation. The lattice parameter, calculated by Rietveld refinement, are 0.54123nm, 0.54069nm, 0.54048nm, and 0.53892nm (**cf. Table 1**) for CeO_2, $Ce_{0.98}Zr_{0.02}O_2$, $Ce_{0.95}Zr_{0.05}O_2$, and $Ce_{0.8}Zr_{0.2}O_2$, respectively. Similar contractions have been reported for $Ce_{1-x}Zr_xO_2$ powder samples and summarized in the Vegard plot [25, 26]. The observed reduction of the lattice parameter is caused by the lattice contraction induced by the replacement of Ce^{4+} (0.097nm) by slightly smaller Zr^{4+} (0.084nm). These findings indicate that Zr is successfully doped into the CeO_2 lattice in agreement with the previously study [17]. Simultaneously to the lattice contraction, the incorporation by Zr^{4+} also reduce the crystalline size, calculated by Rietveld refinement, from 8.5 nm for CeO_2 nano-rods to 6.9 nm for $Ce_{0.8}Zr_{0.2}O_2$ nano-rods (**cf. Table 1**). For polycrystalline $Ce_{1-x}Zr_xO_2$ nanofibers the decrease of particle size was even more pronounced [15].

Physisorption experiments reveal BET surface areas of 90 m^2/g, 86 m^2/g, 92 m^2/g, and 80 m^2/g for CeO_2, $Ce_{0.98}Zr_{0.02}O_2$, $Ce_{0.95}Zr_{0.05}O_2$, and $Ce_{0.8}Zr_{0.2}O_2$, respectively **(cf. Table 1)**. Practically, the BET surface of all studied nano-rod samples is 86±6 m^2/g, thus allowing for a direct comparison of activity (STY) and OSC data without normalization to the BET surface area.
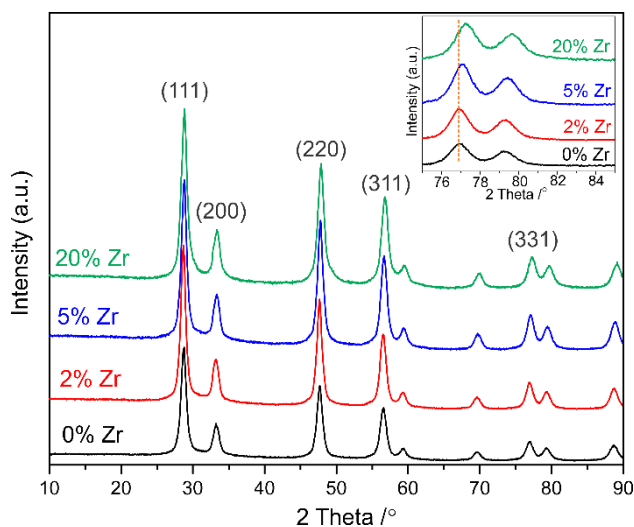

Figure 1: XRD 2θ-scans of the as-prepared $Ce_{1-x}Zr_xO_2$ nano-rods (x=0 to 0.2). Inset: magnified 2θ-scan around the (331) reflection in order to emphasize the shift of diffraction angle θ to higher values.

Figure 2 shows TEM images of the as-prepared $Ce_{1-x}Zr_xO_2$ nano-rods. All of them exhibit rod-shaped morphology with a mean diameter of 7.5±0.5 nm (**cf. Figure.S1**), which is consistent with the crystalline size estimated by Rietveld refinement of XRD data. The average length of the pure CeO_2 nano-rods is around 200 nm, which has already been reported in our previous study **[10]**. However, with increasing Zr concentration decreases the average length of nano-rods remarkably to 150nm, 80nm and 50nm for $Ce_{0.98}Zr_{0.02}O_2$, $Ce_{0.95}Zr_{0.05}O_2$, and $Ce_{0.8}Zr_{0.2}O_2$ nano-rods, respectively. This observation does not conflict with XRD since XRD is mainly sensitive to the thickness of the nano-rods but not to their lengths.
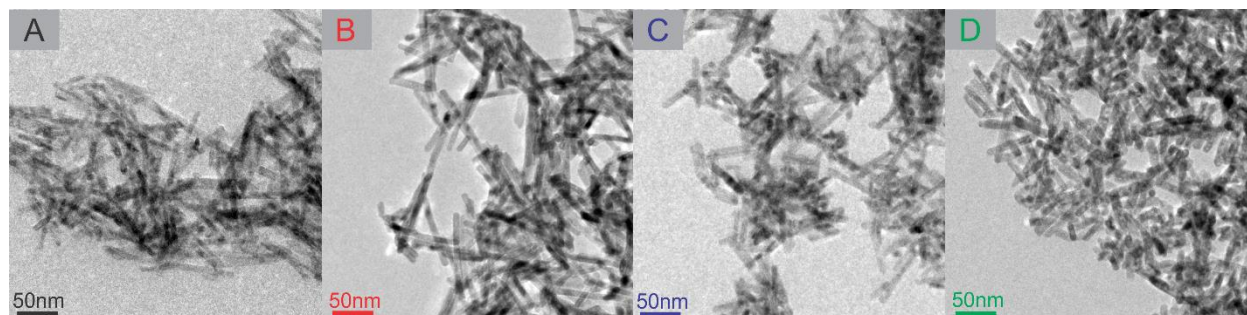
Figure 2: TEM images of as-prepared $Ce_{1-x}Zr_xO_2$ nano-rods. A): CeO_2, B): $Ce_{0.98}Zr_{0.02}O_2$, C): $Ce_{0.95}Zr_{0.05}O_2$, D): $Ce_{0.8}Zr_{0.2}O_2$.

OSC and OSCc, representing the ability of oxygen storage/release that is considered to play a key role for the activity of several oxidation reaction, are summarized in **Figure 3**. As the Zr content increases from 0% to 20%, the plain oxygen-storage capacity (OSC) keeps almost constant at 63 ± 3 $\mu mol(O)/g$ (**cf. Table 1**) which may be attributed to the constant BET surface area and a comparable O vacancy concentration at the surface. The found OSC values are in broad agreement with those of a previous study on polycrystalline $Ce_{1-x}Zr_xO_2$ nanofibers [23]. For instance, $Ce_{0.8}Zr_{0.2}O_2$ nanofibers showed OSC value at 50 $\mu mol(O)/g$, while the as-prepared $Ce_{0.8}Zr_{0.2}O_2$ nano-rods reveals 66 $\mu mol(O)/g$ for the OSC [23].
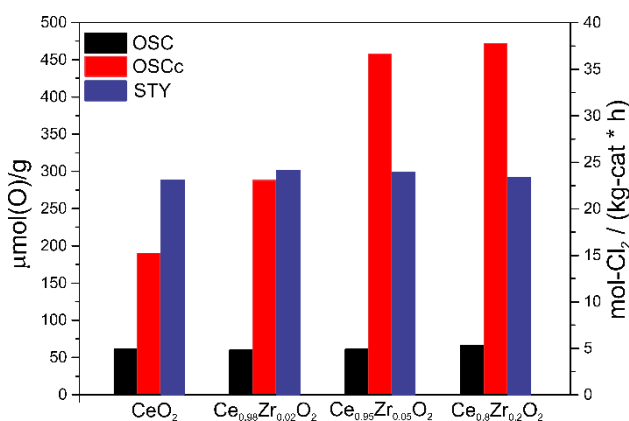
Figure 3: Plain oxygen-storage capacity, complete oxygen-storage capacity (OSC and OSCc, respectively) of the as-prepared $Ce_{1-x}Zr_xO_2$ nano-rods in comparison with their catalytic activity under mild condition (Ar:HCl:O_2 = 7:1:2).

Quite in contrast to the OSC, the complete oxygen-storage capacity (OSCc) increases from 188 $\mu mol(O)/g$ (0%Zr) to 286 $\mu mol(O)/g$ (2% Zr), and further to 458 $\mu mol(O)/g$ 5% Zr doping. The trend in OSCc fits quite well to a previous study on mixed nanofibers [15] and other studies from

the literatures **[27, 28]**. The main reason for the higher OSCc is seen in the lowering the activation energy for oxygen-ion diffusion and O vacancy formation due to the substitution of Ce^{4+}(0.097nm) by Zr^{4+}(0.084nm) **[27]**. However, the OSCc could only be improved very little (472 μmol(O)/g) when Zr doping is further increased to 20%, indicating that already for 5% Zr doping the whole bulk of the particle is participating in the OSCc.

A direct comparison with activity in **Figure 3** reveals that the STY values of $Ce_{1-x}Zr_xO_2$ nano-rods under mild reaction conditions are practically independent of the Zr concentration, similar to the BET surface are and the OSC.

We would like to notice that most of the reported OSC values in literatures are frequently OSCc values since Ar/H_2 mixture as reduction gas are employed for quite long time periods (minutes) rather than short pulses (1~2s). The published protocols for OSC measurements differ quite substantially among various research studies, thus impairing a direct comparison with literature values. These uncertainties in the OSC/OSCc determination call for harmonization of the experimental procedure.

Table 1. Characterization of the as-prepared $Ce_{1-x}Zr_xO_2$ nano-rods

	Surface area (m^2g^{-1})	Lattice Parameter $(nm)^a$	Crystalline Size $(nm)^a$	Surface atomic ratio $Zr/(Zr+Ce)^b$	OSC μmol(O)/g	OSCc μmol(O)/g
CeO_2	90	0.54123	8.5	0	61	188
$Ce_{0.98}Zr_{0.02}O_2$	86	0.54069	8.0	1.7%	60	288
$Ce_{0.95}Zr_{0.05}O_2$	92	0.54048	7.5	3.4%	61	458
$Ce_{0.8}Zr_{0.2}O_2$	80	0.53892	6.9	17.0%	66	472

a: determined by Rietveld refinement. b: determined by XPS.

In order to quantify the concentration of Zr^{4+} in the surface region, we conducted XPS experiments of as-prepared $Ce_{1-x}Zr_xO_2$ nano-rods. From the Zr 3d and Ce 4d spectra shown in **Figure S2** the atomic ratio of Zr/(Zr+Ce) is determined as 0, 1,7%, 3.4% and 17.0% for CeO_2, $Ce_{0.98}Zr_{0.02}O_2$, $Ce_{0.95}Zr_{0.05}O_2$, and $Ce_{0.8}Zr_{0.2}O_2$ respectively, thus being reconciled with the bulk stoichiometries. Obviously, no substantial segregation of Zr towards the surface nor dissolution of Zr into the bulk is observed.

3.2 Activity/Stability Experiment: HCl Oxidation Reaction

The activity experiments are summarized in **Figure 4**. The reactor is heated up to the reaction temperature of 430 °C in pure Ar flow of 15 sccm. Subsequently, the Ar flow is switched to the actual reaction mixture feeds (Ar:HCl:O_2=7:2:1 or Ar:HCl:O_2=6.5:2.5:1 or Ar:HCl:O_2=6:3:1) for 24 hours, and the space time yield (STY) is measured online by UV-vis spectroscopy. For a reaction condition of Ar:HCl:O_2=7:2:1 (cf. **Figure 4A**), pure CeO_2 nano-rods reveal a substantial decrease in activity during the first 5h on stream, and the activity keeps slowly decreasing during the residual reaction time. Consistent with XRD experiments we presume that part of CeO_2 suffer from crystalline bulk chlorination $CeCl_3*nH_2O$. Next, $Ce_{0.98}Zr_{0.02}O_2$ nano-rods are exposed to the same reaction condition, with the results that steady-state of STY is reached after 2h. This experiments indicate that 2% Zr^{4+} doping is sufficient to maintain catalytic stability of CeO_2 in terms of activity under the reaction condition of Ar:HCl:O_2=7:2:1. Undoubtedly, $Ce_{0.95}Zr_{0.05}O_2$ and $Ce_{0.8}Zr_{0.2}O_2$ nano-rods are also stable under this reaction condition, showing the comparable activity.

We performed also activity experiments under even more harsh condition, Ar:HCl:O_2=6.5:2.5:1 (cf. **Figure 4B**). Obviously, pure CeO_2 nano-rods are unstable, however, the activity curve looks quite different from the one shown in **Figure 4A**. The STY drops continuously during the first 8h on stream, The residual activity at steady state is likely due to $CeCl3*nH_2O$, consistent with the literature **[8, 29]**. For the $Ce_{0.98}Zr_{0.02}O_2$ nano-rods, the activity decreases much more slowly than for pure CeO_2 without reaching steady-state condition even after 24h, likely due to bulk chlorination of the CeO_2 (compare XRD experiments in **Figure 5**). This result indicate that 2% Zr^{4+} doping is not sufficient to stabilize the Ce-based against bulk chlorination under this harsh reaction condition. Therefore, we measured the activity of $Ce_{0.95}Zr_{0.05}O_2$ and $Ce_{0.8}Zr_{0.2}O_2$ nano-rods under the same reaction condition. Both samples show stable activity and high steady STY with $Ce_{0.8}Zr_{0.2}O_2$ being little more active than $Ce_{0.95}Zr_{0.05}O_2$. Thus 5% (20%) Zr^{4+} doping could not only stabilize the Ce-based catalyst against deactivation, but also improves the activity under the more harsh reaction condition (Ar:HCl:O_2=6.5:2.5:1).
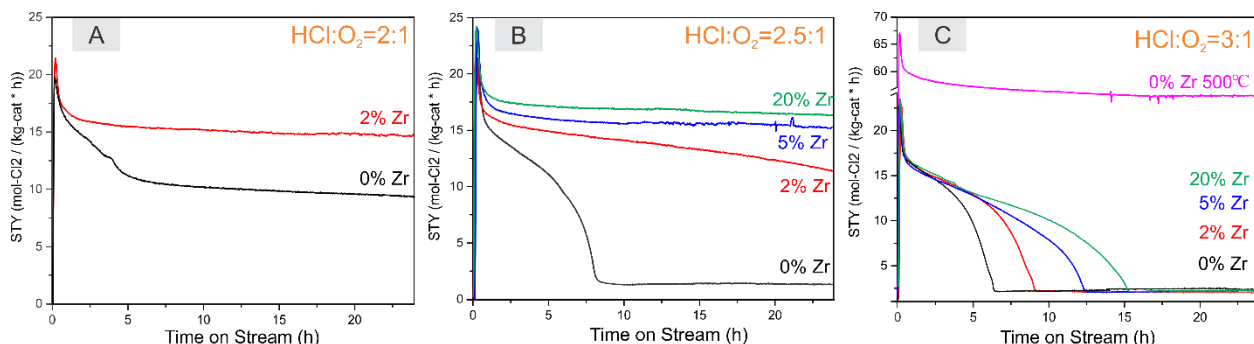
Figure 4: Space time yield (STY) per gram of molecular chlorine in the HCl oxidation is shown for the $Ce_{1-x}Zr_xO_2$ nano-rods (x=0.02~0.2). The reaction temperature during the reaction was 430°C and 500°C. A) reaction condition: Ar:HCl:O_2 = 7:2:1, B) reaction condition: Ar:HCl:O_2 = 6.5:2.5:1 and C) reaction condition: Ar:HCl:O_2 = 6:3:1 and a total flow rate of 15sccm.

With the purpose of testing the limitation of the improved stability by Zr^{4+} doping, we exposed the $Ce_{1-x}Zr_xO_2$ nano-rods to even more harsh reaction condition Ar:HCl:O_2=6:3:1 (cf. **Figure 4C**). All of the tested catalysts deactivated down to the activity level associated with $CeCl_3*nH_2O$. However, the time interval for full deactivation of $Ce_{1-x}Zr_xO_2$ nano-rods strongly depends on the concentration x of doped Zr^{4+}: the higher the Zr^{4+} concentration the longer full deactivation takes. Last, pure CeO_2 nano-rods are exposed to Ar:HCl:O_2=6:3:1 reaction mixture, this time however with higher reaction temperature of 500°C. Compare to pure CeO_2 nano-rods and reaction temperature of 430°C, the original STY and steady state STY is increased by a factor of 3 and 25, respectively. No deactivation is encountered, indicating a stable catalyst under this reaction condition. From these results, we conclude that higher reaction temperature efficiently improve the stability of pure CeO_2, even under extremely harsh reaction condition, consistent with previously studies **[8, 29]**.

The main conclusion drawn from the activity experiments are that besides low HCl concentration (equal to high oxygen concentration) in the feed gas also high reaction temperature and doping of Zr^{4+} into the CeO_2 nano rod lattice efficiently improve the catalytic stability against deactivation.

3.3 Characterization of $Ce_{1-x}Zr_xO_2$ nano-rods after the catalytic tests

According to our previous study, the stability of CeO_2 based catalyst was directly influenced by bulk chlorination, with the crystalline $CeCl_3*nH_2O$ forming during catalytic testing **[10, 29]**. In **Figure 5**, we present XRD data of $Ce_{1-x}Zr_xO_2$ nano-rods after Deacon reaction under various conditions for which the activity data are shown in **Figure 4**. For the pure CeO_2 nano-rods,

$CeCl_3*6H_2O$ reflections are detected in XRD for all reaction mixtures, evidencing bulk chlorination and explaining the deactivation of the catalysts. The degree of bulk-chlorination increases with the increasing HCl concentration. For a reaction mixture of $Ar:HCl:O_2 = 7:2:1$ (430°C) 2%Zr doping suffices to suppress bulk chlorination (**Figure 5A**). For $Ar:HCl:O_2 = 6:3:1$ at 430°C all $Ce_{1-x}Zr_xO_2$ nano-rods form massive bulk-chloride after 24h on stream (**Figure 5C**), fully compatible with the activity data of **Figure 4C**.

For gaining a deeper insight into the stabilizing effect of Zr^{4+} doping, reaction induced changes for $Ar:HCl:O_2 = 6.5:2.5:1$ at 430°C (cf. **Figure 4B**) are investigated by XRD (**Figure 5B**), XPS and TEM (**Figure 6**). Under this reaction condition both pure CeO_2 and $Ce_{0.98}Zr_{0.02}O_2$ suffer from severe bulk-chlorination after 24h on stream. Quantitative Rietveld refinement of the XRD data reveals that the chlorination degree is strongly dependent on the concentration of Zr^{4+} doping: 70% of pure CeO_2 nano-rods are transformed to $CeCl_3*6H_2O$ and the chlorination degree decrease to 11% for $Ce_{0.98}Zr_{0.02}O_2$. Obviously, 2% Zr^{4+} efficiently decrease the chlorination rate, but is unable to fully suppress bulk chlorination. These degrees of bulk-chlorination fit well to the measured near-surface chlorination by XPS (cf. **Table 2**) with Cl/(Ce+Zr)=190% and 60% for pure CeO_2 and $Ce_{0.98}Zr_{0.02}O_2$, respectively.
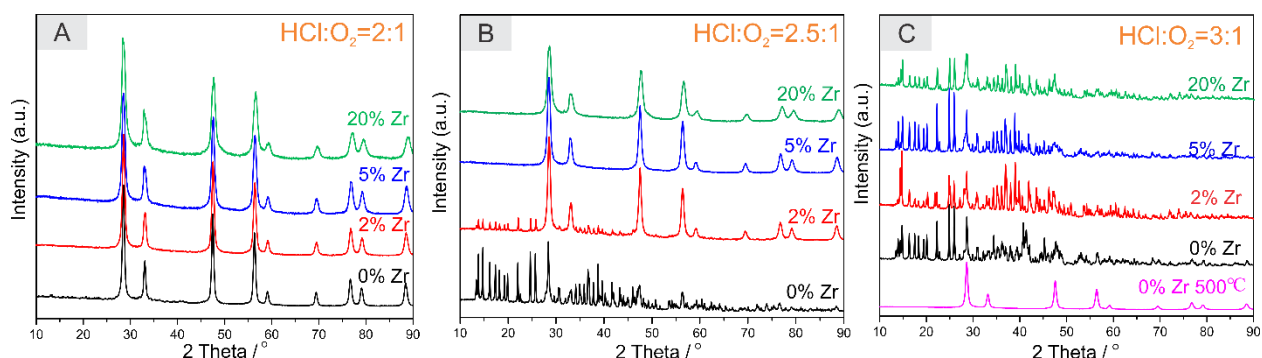
Figure 5: XRD scans of $Ce_{1-x}Zr_xO_2$ nano-rods after Deacon reaction under different reaction condition. Black: CeO_2, red: $Ce_{0.98}Zr_{0.02}O_2$, blue: $Ce_{0.95}Zr_{0.05}O_2$, magenta: $Ce_{0.8}Zr_{0.2}O_2$, magenta: CeO_2 under reaction temperature at 500°C.

Doping of 5%Zr and 20%Zr both stabilizes CeO_2 nano rods against bulk chlorination. Nevertheless XPS indicates near-surface chlorination of Cl/(Ce+Zr)=23% for both $Ce_{0.95}Zr_{0.05}O_2$, and $Ce_{0.8}Zr_{0.2}O_2$ nano-rods. It seems that this surface Cl concentration is self-limiting beyond a Zr^{4+} doping of 5% and is slightly higher than that expected values from on-surface Cl only (about 10-15%). Quite in contrast to bulk chlorination, surface chlorination is not associated with a loss in

catalytic activity. However, near-surface chlorination will defines the catalytically active phase which is different from the original $Ce_{1-x}Zr_xO_2$ nano-rods with their (110) facets. Besides near-surface chlorination, also the surface Zr concentration slightly increases as revealed by the Zr/(Zr+Ce) ratio of $Ce_{1-x}Zr_xO_2$ nano-rods after the Deacon reaction (cf. **Table 2**). May be this enrichment of Zr is induced by surface Ce-chloride formation.

Table 2. Characterization of the $Ce_{1-x}Zr_xO_2$ nano-rods after Deacon reaction under the reaction condition of Ar:HCl:O$_2$ = 6.5:2.5:1.

	Crystalline Size(nm) [a]	Surface atomic ratio Zr/(Zr+Ce) [b]	Surface atomic ratio Cl/(Ce+Zr) [b]	X CeCl$_3$*nH$_2$O [a]	Surface atomic ratio Cl/O [b]
CeO_2	15.5&89.3[c]	0	190%	70%	360%
$Ce_{0.98}Zr_{0.02}O_2$	11.1&60.8[c]	2.4%	60%	11%	75%
$Ce_{0.95}Zr_{0.05}O_2$	10.0	4.3%	23%	0	16%
$Ce_{0.8}Zr_{0.2}O_2$	7.2	22.8%	23%	0	17%

a: determined by Rietveld refinement. b: determined by XPS. c: crystalline size of $CeCl_3$*6H$_2$O. Crystalline Size (nm) were determined by Rietveld refinement for the two different phases.

In order to discriminate between on-surface Cl and Cl in the surface region, we performed the following XPS experiment before and after using an air plasma source for cleaning the surface of the nano-rod powders after Deacon reaction (cf. **Figure S3**). The air plasma removes preferentially adsorbed species. For pure CeO_2 nano-rods after Deacon reaction under Ar:HCl:O$_2$ = 6:3:1 and a reaction temperature of 500 °C the Cl/Ce ratio is 9.2% that is reduced to Cl/Ce=0% upon plasma treatment. This experiment indicates that Cl exists likely only in the form of on-surface Cl on CeO_2 nano-rods. Next we studied the chlorine concentration of $Ce_{0.8}Zr_{0.2}O_2$ nano-rods after Deacon reaction under Ar:HCl:O$_2$ = 6.5:2.5:1 and a reaction temperature of 430 °C. The Cl/(Ce+Zr) ratio was 22% that is reduced to Cl/(Ce+Zr)=10% after plasma treatment. From this experiment we infer that a substantial part of the chlorine (about half) is hosted in the surface near region below the surface. We presume that in all cases (cf. **Table 3**) where the Cl/(Ce+Zr) concentration is significantly above 10%, Cl is accommodated in the surface near region below the surface.

For a reaction temperature of 500°C, XRD (cf. **Figure 5C**) indicates that pure CeO_2 nano-rods are stable even under very harsh reaction conditions consistent with the activity data in **Figure 4C**. The particle size derived from XRD data is 12.7 nm, being significantly larger than the 8.5 nm of particles size for the fresh catalysts. With TEM, we can clearly observe that the nano-rods are still intact, although their width have increased and their lengths is reduced (cf. **Figure S4**).

In **Figure 6** we summarize our results from TEM characterizations of the $Ce_{1-x}Zr_xO_2$ nano-rods in order to visualize the morphological changes of the sample after Deacon reaction under more harsh conditions (Ar:HCl:O_2=6.5:2.5:1). For pure CeO_2 nano rods dramatic changes are observed. The rod morphology transforms to cubic and cuboid structure (cf. **Figure 6A**). Since most of the CeO_2 is transformed to Ce-chloride (70%), the cuboids in TEM may be assigned to crystalline $CeCl_3*6H_2O$ that is also compatible with its space group of P2/n. The average particle size observed in TEM agrees reasonably well with the derived particle size of about 70nm from XRD. For the $Ce_{0.98}Zr_{0.02}O_2$, we can recognize in TEM (cf. **Figure 6B**) that the shape of rods is almost not affected, however, the width of the rods are slightly larger with an average value of 10.8 nm (cf **Figure S5A**). Also visible in TEM are small cuboids which can be ascribed to the 11% crystalline $CeCl_3*nH_2O$ that was derived from the XRD data. For $Ce_{0.95}Zr_{0.05}O_2$, the nano-rods (cf. **Figure 6C**), showing an average width of 9.7nm (cf. **Figure S5B**), are slightly broader than the fresh ones, but particles with cuboid shape are not observed. Both observations are reconciled with the XRD data (cf. **Figure 5B**) that show no crystalline $CeCl_3*6H_2O$ formation but a slight increase in the particle size. For $Ce_{0.8}Zr_{0.2}O_2$, we cannot observe any morphological alterations in the TEM images (cf. **Figure 6D, 2D**), consistent with the unchanged crystalline size (cf. **Tables 1,2)** and the non-presence of crystalline $CeCl_3*6H_2O$ in the XRD data (cf. **Figure 5B**), clearly indicating structural stability.

Altogether, we conclude from TEM and XRD that the stability of the $Ce_{1-x}Zr_xO_2$ nano-rods runs in the following order: $Ce_{0.8}Zr_{0.2}O_2 > Ce_{0.95}Zr_{0.05}O_2 > Ce_{0.98}Zr_{0.02}O_2 > CeO_2$ nano-rods.
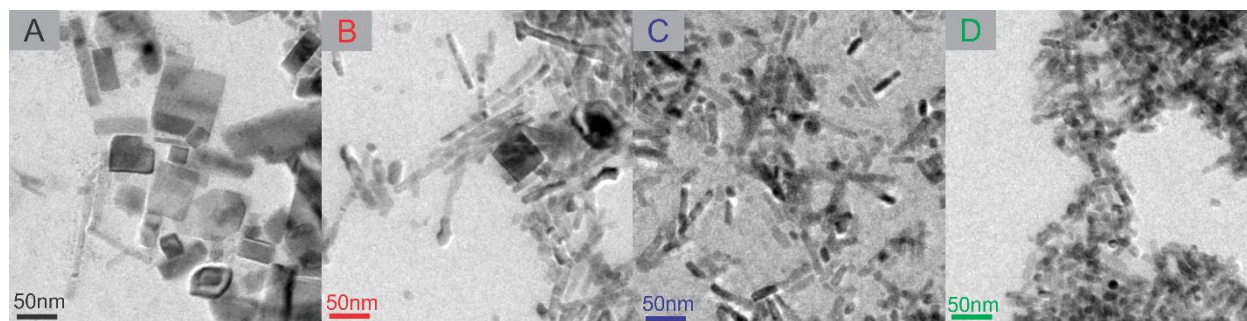
Figure 6: TEM images of $Ce_{1-x}Zr_xO_2$ nano-rods after Deacon reaction Ar:HCl:O_2 = 6.5:2.5:1. A): CeO_2, B): $Ce_{0.98}Zr_{0.02}O_2$, C): $Ce_{0.95}Zr_{0.05}O_2$, D): $Ce_{0.8}Zr_{0.2}O_2$.

From TEM we conclude that the crystalline $CeCl_3*6H_2O$ phase is formed by nucleation and growth of separate particles. Exposure of $Ce_{1-x}Zr_xO_2$ nano rods to a harsh reaction mixture leads

to corrosion of the nano-rods and the formation of a volatile molecular $CeCl_3$ species. In turn, the molecular CeCl3 nucleates and grows with cuboid shape. This process is particularly evident for pure CeO_2 nano-rods, but this process is equally observed for $Ce_{0.98}Zr_{0.02}O_2$. For $Ce_{0.98}Zr_{0.02}O_2$ and $Ce_{0.95}Zr_{0.05}O_2$ there is another process evident in TEM, namely the swelling of the nano rods. There are two ways of explanation. Either $CeCl_3*6H_2O$ covers the $Ce_{1-x}Zr_xO_2$ nano rods, or chlorine penetrates the surface near region thereby increasing the layer spacings. Covering of $CeCl_3*6H_2O$ would reduce the Zr concentration in XPS that is not observed. Therefore, we favor swelling of the nano-rods by the chlorine penetration into deeper layers.

In order to clarify the chlorination degree of $Ce_{0.95}Zr_{0.05}O_2$ as a function of reaction time ($Ar:HCl:O_2 = 6:3:1$ at 430°C) we took XRD after 0.5, 2, 4, 8, 12, 18, 24h on stream (cf. **Figure 7A**). The chlorination degree is quantified by Rietveld refinements of the XRD data and presented in **Figure 7B**. Below 2h there is almost no bulk chlorination discernible (induction period), while from 2h to 18h, the concentration of $CeCl_3*nH_2O$ (chlorination degree) increases strongly from 5% to 79% and finally saturates at 80±1%. This chlorination behavior is reminiscent of a nucleation and growth mode, where during the induction period critical nuclei are formed which then can grow further in size until most of the CeO_2 is transformed to $CeCl_3*nH_2O$.
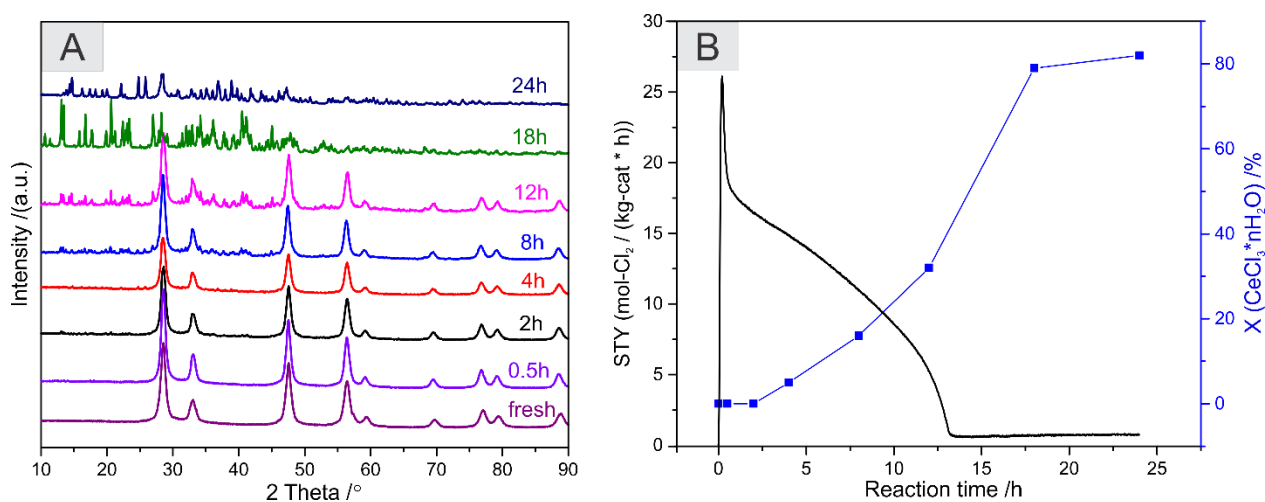

Figure 7: A): XRD scans of $Ce_{0.95}Zr_{0.05}O_2$ nano-rods after Deacon reaction under reaction condition of Ar:HCl:O2 = 6:3:1 at 430°C for different reaction time (from 0 to 24h). B): chlorination degree x(CeCl3*nH2O) versus reaction time.

4. Conclusion

From XRD and TEM we infer that the solid solutions of $Ce_{1-x}Zr_xO_2$ in the form of nano-rods are successfully synthesized. These $Ce_{1-x}Zr_xO_2$ nano-rods were employed in the Deacon reaction under different reaction condition. Both activity and stability are closely related to the HCl to O_2 ratio in the reaction mixture, the reaction temperature and the doping concentration of Zr^{4+}. Excess oxygen in the reaction mixture will improve the catalytic stability against bulk chlorination. High reaction temperature increases both catalytic stability and activity. Doping Zr^{4+} strongly improves the stability of CeO_2 against bulk chlorination during the reaction.

Pure CeO_2 nano-rods have shown to suffer from bulk-chlorination of the catalyst for all reaction mixtures $HCl:O_2 > 2$ that is accompanied by dramatic activity losses. However, for a reaction mixture of $HCl:O_2 = 2.5:1$, already 5% Zr doping suffices to stabilize $Ce_{1-x}Zr_xO_2$ nano-rods against bulk chlorination. For even more harsh reaction conditions $HCl:O_2 = 3:1$ none of the $Ce_{1-x}Zr_xO_2$ nano-rods were stable at a reaction temperature of 430°C. Increasing the reaction temperature to 500°C enables even pure CeO_2 nano-rods to be stable under such harsh reaction conditions.

The corrosion process of $Ce_{1-x}Zr_xO_2$ nano-rods via bulk-chlorination destroys the nano-rod structure (TEM) and leads to the formation of crystalline $CeCl_3 x 6H_2O$ with low catalytic activity (TEM, XRD). This bulk-chlorination process proceeds via nucleation and growth (TEM and XRD) which is likely to be mediated by a volatile molecular precursor species such as $CeCl_3$. But even bulk stable $Ce_{1-x}Zr_xO_2$ catalysts reveal enhanced surface chlorination (XPS) and an increase in the width of the nano-rods (TEM, XRD). Utilizing oxygen plasma treatment, Cl2p XPS provides evidence for chlorine incorporation into deeper layers in the near surface region of $Ce_{1-x}Zr_xO_2$. The surface chlorine enriched $Ce_{1-x}Zr_xO_2$ may be even considered as the catalytically active phase in the Deacon reaction.

Reference:

[1]. M.W.M. Hisham, S.W. Benson, J. Phys. Chem. 99 (**1995)** 6194

[2]. J. Perez-Ramirez, C. Mondelli, T. Schmidt, O.F.K. Schlüter, A. Wolf, L. Mleczko, T. Dreier, Energy Environ. Sci. 4 (**2011**) 4786-4799

[3]. K. Seki, Catal. Surv. Asia. 14 (**2010**) 168-175

[4]. M. Hammes, M. Valtchev, M. B. Roth, K. Stöwe, W. F. Maier, Appl. Catal. B: Environ 131-133 (**2013)** 389-400

[5]. H. Over, R. Schomäcker, ACS Catal. 3 (**2013**) 1034-1046

[6]. K.K. Feng, C.W. Li, Y.L. Guo, W.C. Zhan, B.Q. Ma, B.W. Chen, M.Q. Yuan, G.Z. Lu, Appl. Catal. B: Environ 164 (**2015**) 483-487

[7]. A.P. Amrute, C. Mondelli, M. Moser, G. Novell-Leruth, N. López, D. Rosenthal, R. Farra, M.E. Schuster, D. Schuster, T. Schmidt, J. Pérez-Ramírez, J. Catal. 286 (**2012**) 287-297

[8]. R. Farra, M. Eichelbaum, R. Schlögl, L. Szentmiklósi, T. Schmidt, A.P. Amrute, C. Mondelli, J. Pérez-Ramírez, D. Teschner, J. Catal. 297 (**2013**) 119-127

[9]. R. Farra, M. Garcia-Melchor, M. Eichelbaum, M. Hashagen, W. Frandsen, J. Allan, F. Girgsdies, L. Szentmiklósi, N. Lopez, D. Teschner, ACS Catal. 3 (**2013**) 2256–2268

[10] C.W. Li, Y. Sun, I. Djerdj, P. Voepel, C. Sack, T. Weller, R. Ellinghaus, J. Sann, Y.L. Guo, B. Smarsly, H. Over, ACS Catal. 7 (**2017)** 6453-6463

[11]. E. Aneggi, C. Leitenburg, J. Llorca, A. Trovarelli, Catal. Tod. 197 (**2012**) 119-126

[12]. T. Montini, M. Melchionna, M. Monai, P. Fornasiero, Chemical. Reviews. 116 (**2016**) 5987-6041

[13]. I. Atribak, A. Bueno-López, A. García-García, J. Catal. 259 (**2008**) 123-132

[14]. P. Maitarad, D.S. Zhang, R.H. Gao, L.Y. Shi, H.R. Li, L. Huang, T. Rungrotmongkol, J.P. Zhang, J. Phys. Chem. C. 117 (**2013**) 9999-10006

[15]. S. Urban, N. Tarabanko, C.H. Kanzler, K. Zalewska-Wierzbicka, R. Ellinghaus, S. F. Rohrlack, L. Chen, P.J. Klar, B.M. Smarsly, H. Over, Catal Lett 143 (**2013**) 1362-1367

[16]. Z.Y. Fei, X.X. Xie, Y. Dai, H.Y. Liu, X. Chen, J.H. Tang, M.F. Cui, X. Qiao, Ind. Eng. Chem. Res. 53 (2014) 19438-19445

[17]. X. Liu, J. Ding, X. Lin, R.H. Gao, Z.H. Li, W.L. Dai, Appl. Catal. A: General. 503 (**2015**) 117-123

[18]. A. Chen, Y. Zhou, N. Ta, Y. Li, W.S. Shen, Catal.Sci.Technol. 5 (**2015**) 4184-4192

[19]. W. Chen, K. Chen, M. Wang, S. Weng, C. Lee, M. C. Lin, Chem.Commun. 46 (**2010)** 3286-3288

[20]. H. Mai, L. Sun, Y. Zhang, R. Si, W. Feng, H. Zhang, H. Liu, C. Yan, J. Phys. Chem. B. 109 (**2005**) 24380-24385

[21]. J. He, T. Xu, Z. Wang, Q. Zhang, W. Deng, and Y. Wang, Angew. Chem. Int. Ed. 51 (**2012**) 2438-2442

[22]. Ch. Kanzler, S. Urban, K. Zalewska-Wierzbicka, F. Hess, S.F. Rohrlack, C. Wessel, R. Ostermann, J.P. Hofmann, B.M. Smarsly, H. Over, Chem Cat. Chem. 5 (**2013**) 2621-2626.

[23]. M. Möller, H. Over, B.Smarsly, N. Tarabanko, S. Urban, Catal. Tod. 253 (**2015**) 2017-218.

[24]. M. Möller, S. Urban, P. Cop, T. Weller, R. Ellinghaus, M. Kleine-Boymann, C. Fiedler, J. Sann, J. Janek, L. Chen, P. J. Klar, D. M. Hofmann, J. Philipps, P. Dolcet, S. Gross, H. Over, and B. M. Smarsly, Chem Cat. Chem. 7 (**2015**) 3738-3747.

[25]. W. T. Gibbons, L. J. Venstrom, R. M. De Smith, J. H. Davidson, G. S. Jackson, Phys.Chem.Chem.Phys 16 (**2014**) 14271-14280

[26]. M. Epifani, T. Andreu, S. Abdollahzadeh-Ghom, J. Arbiol, J. Morante, Adv. Funct. Mater. 22 (**2012**) 2867-2875

[27]. A. Trovarelli, F. Zamar, J. Llorca, C. Leitenburg, G. Dolcetti, J.T. Kiss, J. Catal. 169 (**1997)** 490-502.

[28]. P. Fornasiero, R. Di Monte, G. Ranga Rao, J. Kaspar, S. Meriani, A. Trovarelli, M. Graziani, J. Catal. 151 (**1995)** 168-177.

[29]. C.W. Li, F. Hess, I. Djerdj, G.T. Chai, Y. Sun, Y,L. Guo, B. Smarsly, H. Over, J. Catal. 357 (**2018)** 257-262.

4. Conclusion and Outlook

This PhD project aimed at a deeper understanding of the three main issues in the Deacon reaction with Ce-based catalysts: (i) The influence of facet orientation on the activity and stability of nanocrystalline CeO_2 for HCl oxidation reaction under different reaction conditions ($HCl:O_2 = 1:2/1:1$). (ii) The effect of reaction temperature and water on the catalytic stability of CeO_2 nano-cubes for Deacon reaction. (iii) Stabilizing effect of Zr-doping on CeO_2 nano-rods for HCl oxidation reaction under harsher conditions ($HCl:O_2 > 2$). In order to clarify these issues, shape-controlled CeO_2 nano-particles (namely, nano-rods, nano-cubes, and nano-octahedrons) and additionally Zr doped CeO_2 nano-rods were synthesized. These were investigated for the catalytic performance in a self-designed fixed-bed reactor.

The shape-controlled CeO_2 nano-particles (rods, cubes, and octahedrons), exposing preferentially (110), (100), and (111) facets respectively, were successfully prepared and then employed in catalytic oxidation of HCl under 'mild' ($Ar:HCl:O_2 = 7:1:2$) and 'harsh' ($Ar:HCl:O_2 = 6:2:2$) conditions, respectively. The results turned out that the activity is structure-sensitive. The nano-rods having the highest surface area show the highest STY, followed by nano-cubes and finally octahedrons. However, this activity trend is not consistent with the corresponding surface energies with a stability ordering of (111) > (110) > (100). After reaction under 'mild' conditions, all three different nano-particles still show a crystalline phase with an unchanged morphology. However, under 'harsh' reaction conditions, solely nano-rods are stable, while nano-cubes and nano-octahedrons form crystalline hydrated $CeCl_3$ and their specific morphologies are partly destroyed. Concluding, the catalytic stability is facet-depending as well: (110) facets preferentially exposed by nano-rods are much more stable than (100) and (111) facets, preferentially exposed by nano-cubes and nano-octahedrons respectively. CeO_2 nano-rods are showing the highest STY and highest stability as well.

The reaction temperature has a strong impact on the catalytic activity and stability of CeO_2 in the HCl oxidation reaction. CeO_2 nano-cubes with preferentially (100) facets orientation were employed for HCl oxidation under 'mild' conditions at different reaction temperatures. Above 390 °C, the catalyst is stable and active, while it suffers severe chlorination and deactivation at temperatures below 380 °C. The thermodynamic model of the chlorination process indicates: (1)

Chlorination of CeO_2 is thermodynamically favored at a low reaction temperatures, which is consistent with the experimental results of this work. Thus, one should never shut down the reactor by reducing the reaction temperature under the reaction mixture, which is very important for the industrial Deacon process. (2) Chlorination takes place preferentially at the inlet of the catalyst bed and propagates slowly along the catalyst bed towards the reactor outlet. A double layer experiment has been designed, and the results show that the catalyst in the inlet layer suffers more chlorination than the catalyst in the outlet layer, thus confirming modeling results. (3) Little water in the reaction feed improves the catalytic stability of CeO_2 against bulk chlorination. A dedicated experiment with 1% water in the reaction feed and another experiment without water for comparison have been performed. The CeO_2 catalyst under the feed mixture with 1% water is stable, while under dry feed it undergoes severe chlorination, strongly confirming the theoretical result of a stabilizing effect by water.

From XRD and TEM meausrements we infer that the $Ce_{1-x}Zr_xO_2$ nano-rods were successfully synthesized. These catalysts were employed in the HCl oxidation reaction under different reaction conditions (10 vol% O_2, 20-30 vol% HCl and balanced in Ar). Both catalytic activity and stability are highly dependent on the HCl to O_2 ratio, the reaction temperature and the doping concentration of Zr^{4+}. Excess oxygen in the reaction feed improves the catalytic stability against bulk chlorination. High reaction temperature increases both activity and stability. Doping Zr^{4+} strongly improves the resistance of $Ce_{1-x}Zr_xO_2$ catalysts against bulk chlorination without any degradation of activity in the HCl oxidation reaction. Pure CeO_2 nano-rods suffer from bulk chlorination for all the reaction mixtures (HCl:O_2 $>$2), and concomitantly, dramatic activity loss. For a reaction feed of Ar:HCl:O_2 = 6.5:2.5:1, already 5 mol% Zr doping suffices to stabilize $Ce_{1-x}Zr_xO_2$ nano-rods against bulk chlorination. However, for an even harsher reaction mixture of Ar:HCl:O_2 = 6:3:1, none of the synthesized $Ce_{1-x}Zr_xO_2$ nano-rods were bulk stable. The corrosion process of $Ce_{1-x}Zr_xO_2$ nano-rods via bulk-chlorination destroys the nano-rod structure and leads to the formation of crystalline $CeCl_3 \cdot 6H_2O$ with low catalytic activity. This bulk-chlorination process proceeds via nucleation and growth which is likely to be mediated by a volatile molecular precursor species such as $CeCl_3$. However, even bulk stable $Ce_{1-x}Zr_xO_2$ nano-rods suffer surface chlorination and an increase in the width of the nano-rods. Utilizing oxygen plasma treatment, Cl2p XPS provided evidence for chlorine incorporation into deeper layers in the near surface

region of $Ce_{1-x}Zr_xO_2$ nano-rods. The surface chlorine enriched $Ce_{1-x}Zr_xO_2$ may be even considered as the catalytically active phase in the Deacon reaction.

Toward further understanding the Ce-based catalyst for the HCl oxidation reaction, the following key questions should be addressed:

1. Why different facet orientations affect the catalytic performance of CeO_2 in HCl oxidation reaction? DFT calculation is demanded to offer specific information, such as adsorption energies for HCl and O_2, desorption energies for Cl_2 and H_2O, and etc., of the different facet orientations at an atomic level.

2. How does the surface chlorination start and is this a self-limiting process as shown for RuO_2? One can stop the reaction under mild condition at different reaction time (i.e. 5min, 15min, 30min, 1h, 4h, 12h, 24h, and 48h). Cl2p spectra of these post-reaction CeO_2 catalysts can be achieved by XPS measurement and the Cl/Ce, representing surface chlorination degree, can be quantified as well. Here, also DFT calculation are useful for providing more details about this process.

3. What are the adsorption sites for HCl/Cl^- on the different CeO_2 surface? In-situ Raman techniques are demanded to monitor the vibration of the bond between different elements. Also, combining the STM, LEED, and DFT techniques can be a promising method for clarifying this question.

4. For the reaction feed of Ar:HCl:O_2 = 6.5:2.5:1, the 5 mol% Zr doping prevents $Ce_{1-x}Zr_xO_2$ nano-rod catalysts from bulk chlorination. The mechanism of this stabilizing effect is highly desirable. TEM-mapping of as-prepared and the post-reaction catalysts are demanded to visualize the Zr and Cl distribution on the $Ce_{1-x}Zr_xO_2$ nano-rod. Thermodynamic calculations of the chlorination process of $Ce_{1-x}Zr_xO_2$ nano-rod can be considered as a promising option for answering this question.

5. Appendix

5.1 Supporting Information of Publication 1

Supporting Information

Shape-Controlled CeO$_2$ Nanoparticles:

Stability and Activity in the Catalyzed HCl Oxidation Reaction

Chenwei Li[a,b], Yu Sun[a], Igor Djerdj[c], Pascal Voepel[b], Carl-Christian Sack[b], Tobias Weller[b], Joachim Sann[b], Rüdiger Ellinghaus[b], Yanglong Guo[a,*], Bernd M. Smarsly[b,*], Herbert Over[b,*]

a) Key Laboratory for Advanced Materials, Research Institute of Industrial Catalysis, School of Chemistry and Molecular Engineering, East China University of Science and Technology, Shanghai 200237, PR China
b) Physikalisch-Chemisches Institut, Justus-Liebig-University, Heinrich-Buff-Ring 17, 35392 Giessen, Germany
c) Department of Chemistry, J. J. Strossmayer University of Osijek, Ulica cara Hadrijana 8/a, HR-31000 Osijek , Croatia

* Corresponding authors: E-mail:
herbert.over@phys.chemie.uni-giessen.de
Bernd.Smarsly@phys.Chemie.uni-giessen.de
ylguo@ecust.edu.cn
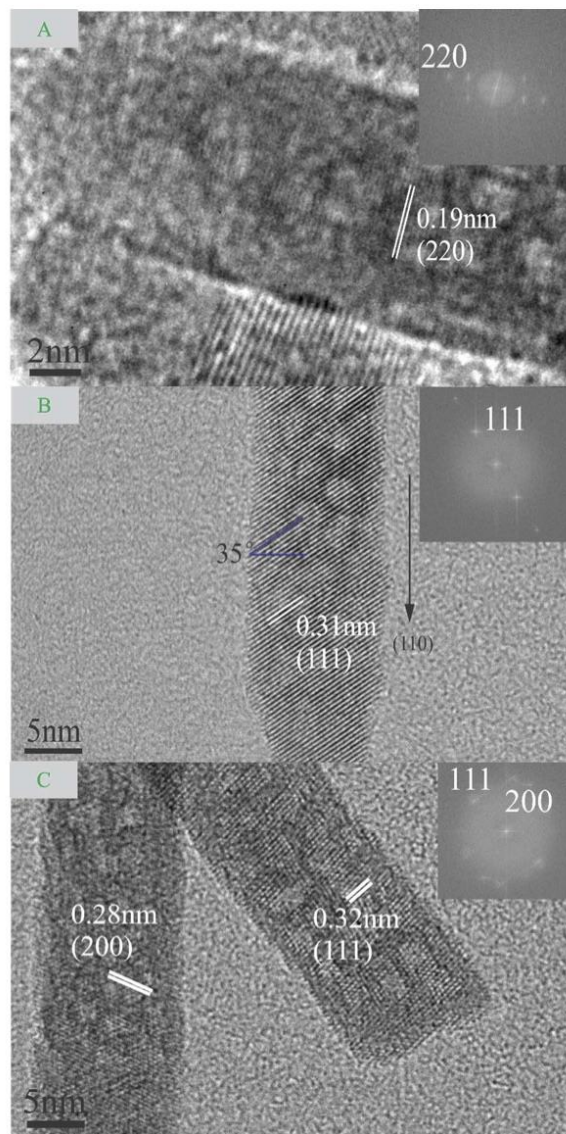
Figure S1：High-resolution TEM images of the as-prepared shape controlled CeO$_2$ nanorods. Inset: Fast Fourier Transformation (FFT) pattern of each particle
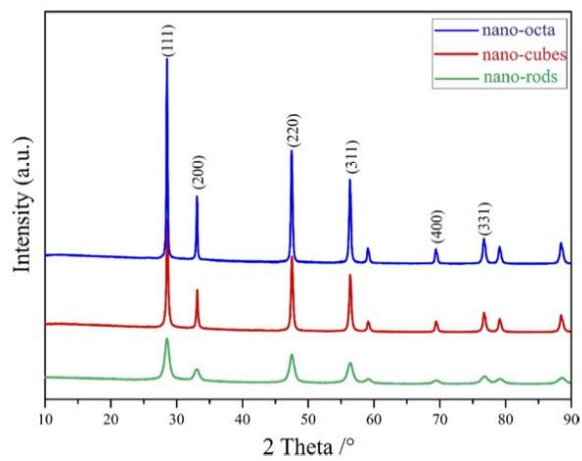
Figure S2: XRD scans of the as-prepared shape controlled CeO_2 particles: (blue) octahedrons; (red) cubes; (green) rods.
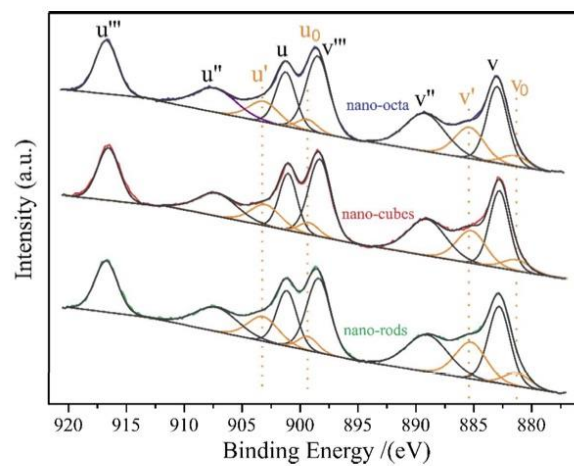
Figure S3: XPS spectra of Ce3d of as-prepared shaped-controlled CeO_2 nanoparticle and their deconvolution into Ce^{3+} and Ce^{4+} related emissions (octahedrons, cubes and rods).
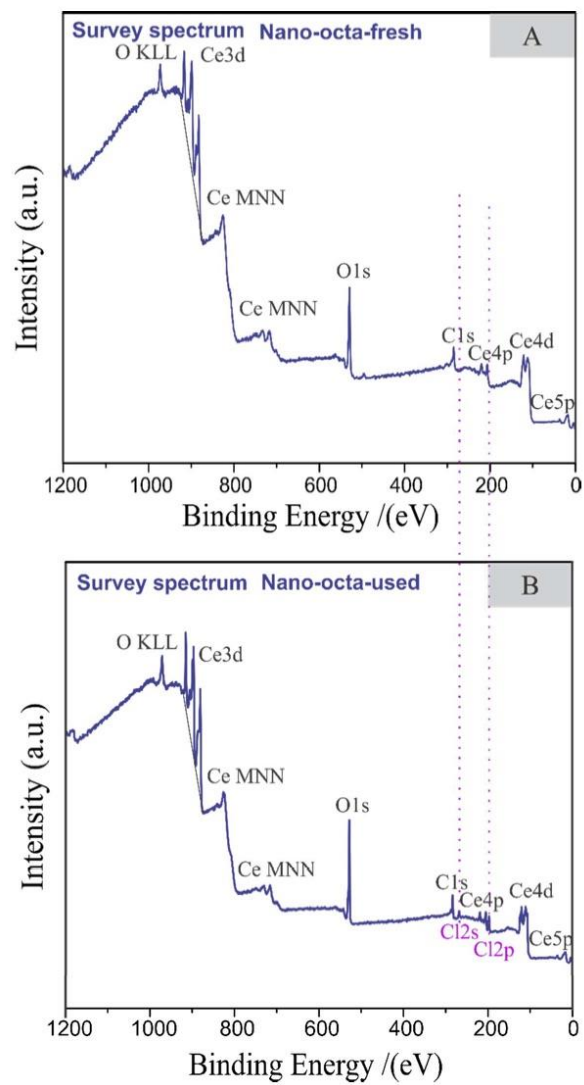
Figure S4: XPS spectra of survey: **A)** as-prepared CeO$_2$ nano-octahedron; **B)** CeO$_2$ nano-octahedron after Deacon reaction of harsh condition.
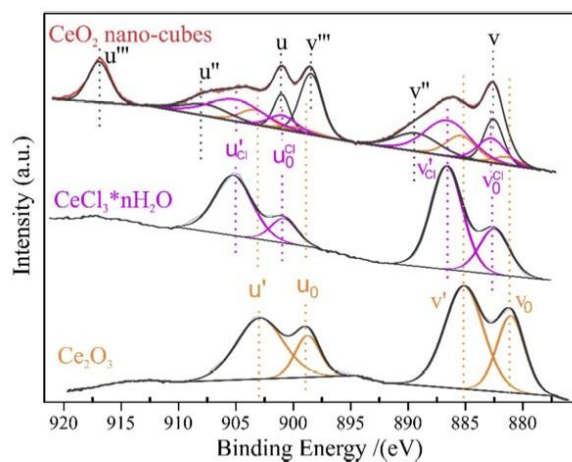
Figure S5: XPS spectra of Ce3d of CeO$_2$ nano-cubes after Deacon reaction under harsh condition. XP reference spectra of pure CeCl$_3$*nH$_2$O and pure Ce$_2$O$_3$ are utilized for the curve fitting of the CeO$_2$ nano-cube spectrum. Details of Ce$_2$O$_3$ reference spectra measurement: Air oxidized Ce foil was evaporated in UHV by an e-beam evaporator on a Ru(0001) single crystal surface up to a film thickness of 3 ML. The XPS measurement was conducted in the same UHV chamber using MgK$_\alpha$ radiation and a Leybold EA 200 analyzer.
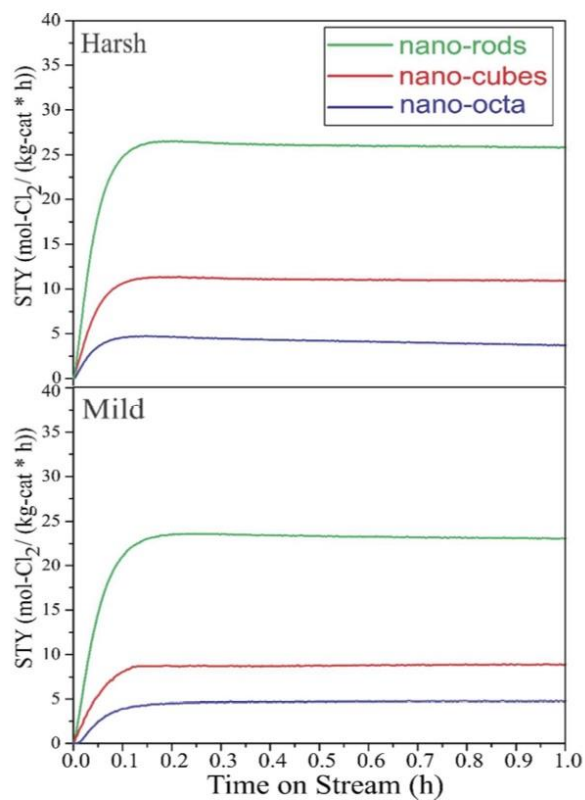
Figure S6: Space time yield (STY) of molecular chlorine in the HCl oxidation reaction using shape-controlled CeO$_2$ nanoparticle (octahedrons, cubes and rods). The temperature during the reaction was T = 430 °C. a) harsh reaction conditions: Ar:HCl:O$_2$=6:2:2 and b) mild reaction conditions: Ar:HCl:O$_2$=7:1:2 and a flow rate of 15 sccm.
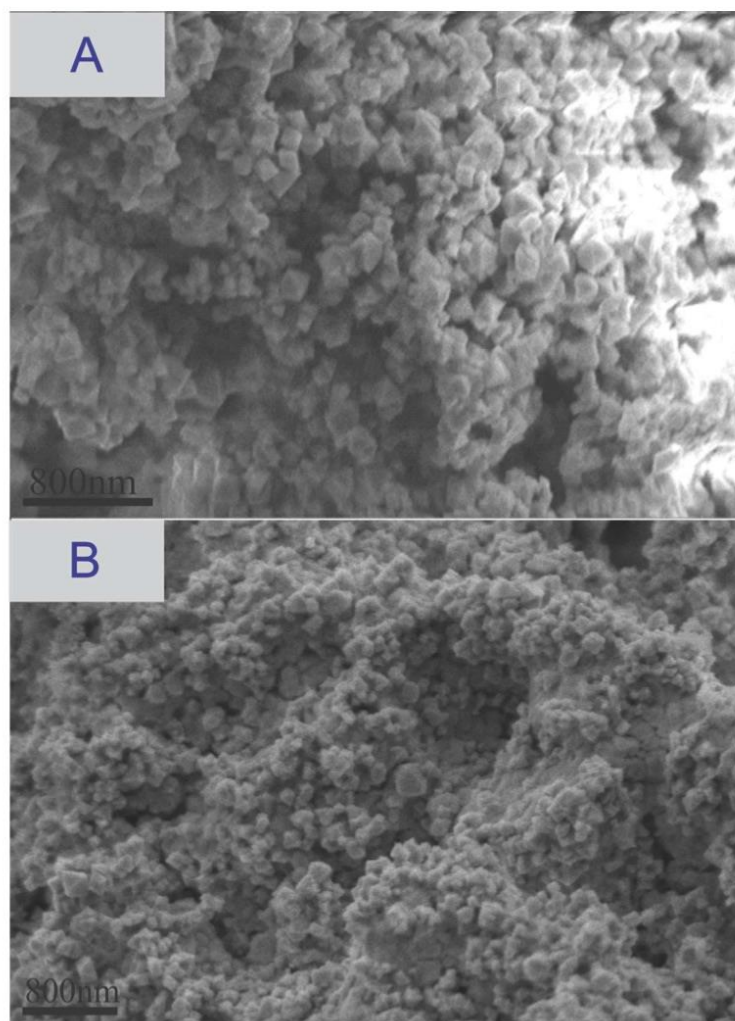
Figure S7: SEM images of the CeO$_2$ nano-octahedrons after the Deacon reaction under harsh condition

5.2 Supporting Information of Publication 2

Supporting Material to „Thermodynamic implications of mixed catalytic cycles on catalyst stability:

The stabilizing effect of water on the CeO$_2$-catalyst in the harsh HCl oxidation reaction"

Chenwei Li[a,b], Franziska Hess[b,c], Igor Djerdj[d], Guangtao Chai[a], Yu Sun[a,b], Yanglong Guo[a,*], Bernd M. Smarsly[b,*], Herbert Over[b,*]

a) Key Laboratory for Advanced Materials, Research Institute of Industrial Catalysis, School of Chemistry and Molecular Engineering, East China University of Science and Technology, Shanghai 200237, PR China

b) Physikalisch-Chemisches Institut, Justus Liebig University, Heinrich-Buff-Ring 17, 35392 Giessen, Germany

c) Dept. of Nuclear Science and Engineering, Massachusetts Institute of Technology, 77 Massachusetts Avenue, Cambridge MA 02139, USA

d) Department of Chemistry, J. J. Strossmayer University of Osijek, Ulica cara Hadrijana 8/a, HR-31000 Osijek , Croatia

Corresponding authors: E-mail:
herbert.over@phys.chemie.uni-giessen.de
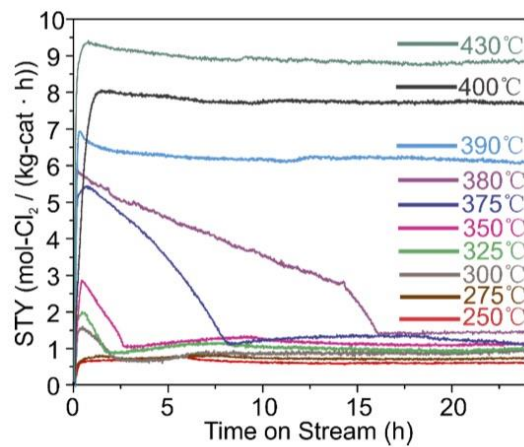Bernd.Smarsly@phys.Chemie.uni-giessen.de
ylguo@ecust.edu.cn

Section S 1: Additional Experiments of the CeO₂ chlorination

Figure S 1: Space time yield (STY) of molecular chlorine in the HCl oxidation reaction using CeO₂ nan-cubes under different temperatures in mild reaction condition (HCl:O₂=1:2).
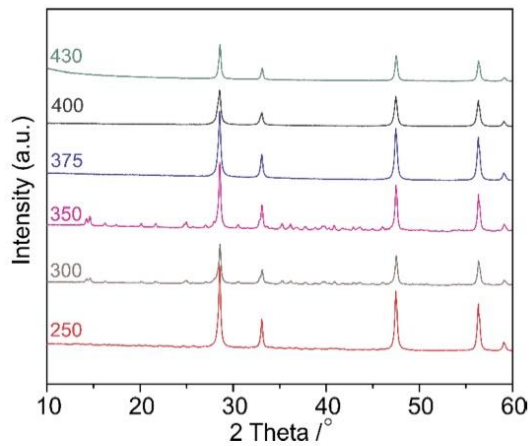

Figure S 2: XRD scans after 1-hour deacon reaction under different temperature in mild reaction condition of CeO₂ nano-cubes.
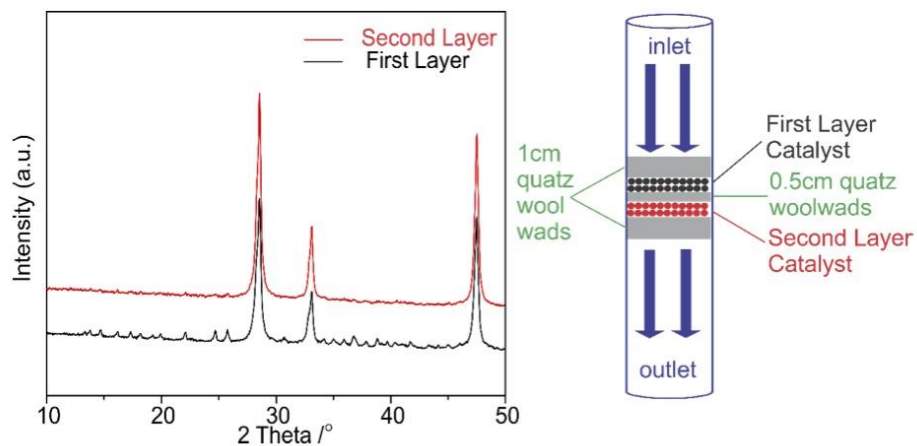
Figure S 3: XRD scans after double layers Deacon reaction under 350 °C in mild reaction condition of the CeO₂ nano-cubes and diagram of the flow reactor with double layers.
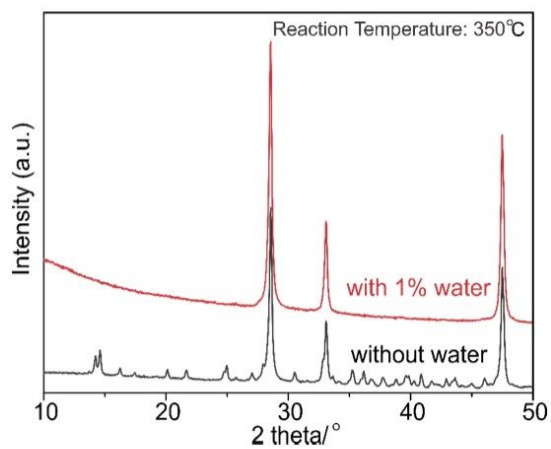

Figure S 4: XRD scans of the CeO2 nano-cubes after 1-hour deacon reaction in mild condition and T=350°C with different feed gas (without water and with 1% water).

The STY values is translated to HCl conversion x$_{HCl}$ by the following formula:

$$X_{HCl} = \frac{2STY \cdot m_{cat} \cdot 22.4e^3}{F_{HCl}}$$

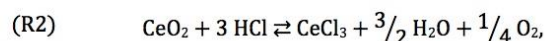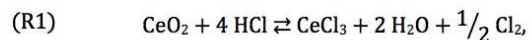Space time yield as STY= mol of Cl₂/(kilogram of catalyst · hour)

X$_{HCl}$: HCl conversion (fixed value)

F$_{HCl}$: Flow of HCl (fixed value)

Section S 2: Thermodynamic modeling of the CeO$_2$ chlorination

Section S 2.1: Chlorination reactions

Two reaction pathways contribute to the chlorination and reoxidation of the CeO$_2$ catalyst under Deacon conditions, as schematically depicted in **Figure 2** (in the main text). Reaction of CeO$_2$ with HCl (R1) produces CeCl$_3$, water and either chlorine or oxygen:
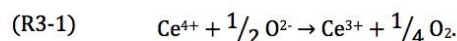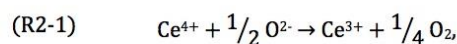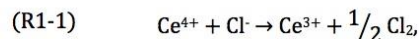
(R1) $CeO_2 + 4\ HCl \rightleftarrows CeCl_3 + 2\ H_2O + {}^{1}/_{2}\ Cl_2,$

(R2) $CeO_2 + 3\ HCl \rightleftarrows CeCl_3 + {}^{3}/_{2}\ H_2O + {}^{1}/_{4}\ O_2,$

while chlorination by Cl$_2$ (R3) produces only O$_2$ and CeCl$_3$:

(R3) $CeO_2 + {}^{3}/_{2}\ Cl_2 \rightleftarrows CeCl_3 + O_2.$
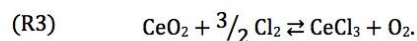
All reactions are reversible as required by thermodynamics, enabling reoxidation either by H$_2$O and Cl$_2$ (forming HCl), by H$_2$O and O$_2$ (also forming HCl) or only by O$_2$ (forming Cl$_2$). Chlorination requires reducing the formal oxidation state of Ce from +IV to +III, the removal of 2 O^{2-} in a molecular form (such as H$_2$O or O$_2$), and finally the incorporation of 3 Cl. In (R1) and (R2), the reduction is achieved by oxidizing 1 Cl- to ${}^{1}/_{2}$ Cl$_2$ or releasing 1 oxide-O^{2-} as ${}^{1}/_{4}$ O$_2$. In both (R1) and (R2), the remaining oxide-O^{2-} are converted to H$_2$O via an acid-base reaction with HCl as a proton donor. In (R3), however, all the oxygen is released as O$_2$ while reducing ${}^{3}/_{2}$ Cl$_2$ to 3 Cl$^-$.

The reactions can thus be decomposed into a redox and an acid-base process. In the redox process, Ce^{4+} is oxidized to Ce^{3+} by either O^{2-} or Cl$^-$:

(R1-1) $Ce^{4+} + Cl^- \rightarrow Ce^{3+} + {}^{1}/_{2}\ Cl_2,$

(R2-1) $Ce^{4+} + {}^{1}/_{2}\ O^{2-} \rightarrow Ce^{3+} + {}^{1}/_{4}\ O_2,$

(R3-1) $Ce^{4+} + {}^{1}/_{2}\ O^{2-} \rightarrow Ce^{3+} + {}^{1}/_{4}\ O_2.$

The remaining oxide-O^{2-} from CeO$_2$ are either converted to water in an acid-base reaction in (R1) and (R2):

(R1-2) $2\ O^{2-} + 4\ HCl \rightarrow 4\ Cl^- + 2\ H_2O,$

(R2-2) ${}^{3}/_{2}\ O^{2-} + 3\ HCl \rightarrow 3\ Cl^- + {}^{3}/_{2}\ H_2O.$
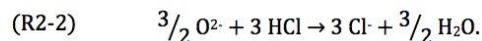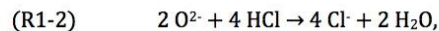
Only in the case of (R3), all oxide-O^{2-} are converted to O$_2$, rather than undergoing an acid-based reaction:

(R3-2) ${}^{3}/_{2}\ O^{2-} + {}^{3}/_{2}\ Cl_2 \rightarrow 3\ Cl^- + {}^{3}/_{4}\ O_2.$
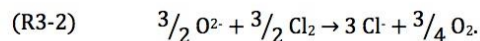
All reactions (R1)-(R3) produce 3 Cl$^-$ which are required for the formation of CeCl$_3$. In addition, either H$_2$O ((R1) and (R2)) or O$_2$ ((R3)) are produced. From chemical intuition, the spontaneous release of O2 to reduce Ce^{4+} to Ce^{3+} (R2-1/R3-1) is considered as unfavorable under Deacon conditions due to an excess of O$_2$ in the gas phase. This reaction

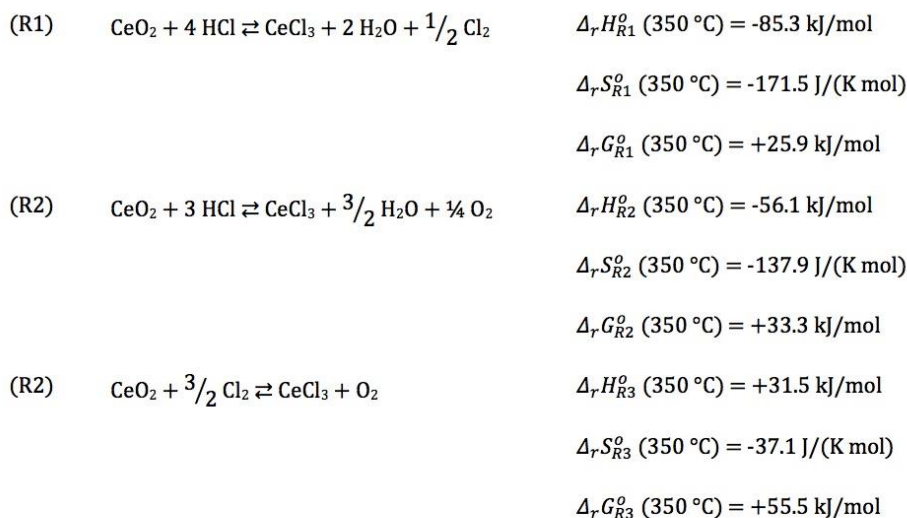does occur when annealing CeO_2 in UHV or under inert gas atmosphere, but not under O_2 atmosphere. However, the reactions R2-2 and R3-2 can provide additional driving forces that can finally tip the chlorination equilibrium depending on the actual conditions. Most notably, R2-2 involves the formation of H_2O which is a very stable product that is not present close to the reactor inlet when dry gas is used for the reaction, and consumes HCl which is amply present in a Deacon reactor. R3-2, on the other hand, consumes Cl_2, which is formed by the Deacon reaction (not being present close to the reactor inlet) and involves the formation of O_2, which is not a stable product and amply present in the reactor under the typically applied oxygen-excess conditions in the Deacon reactor.

Section S 2.2: Free enthalpies of reaction

The above considerations are supported by Gibbs enthalpies that can be computed from the thermodynamic data and formulae given in **Section S 2**. At a typical reaction temperature of 350 °C under standard conditions, i.e., $p_i = p° = 10^5$ Pa = 1000 mbar (with i = HCl, O_2, H_2O, Cl_2) and $a_{CeO_2} = a_{CeCl_3} = 1$:

(R1) $\quad CeO_2 + 4\,HCl \rightleftarrows CeCl_3 + 2\,H_2O + {}^1\!/_2\,Cl_2 \qquad \Delta_r H^o_{R1}$ (350 °C) = -85.3 kJ/mol

$\Delta_r S^o_{R1}$ (350 °C) = -171.5 J/(K mol)

$\Delta_r G^o_{R1}$ (350 °C) = +25.9 kJ/mol

(R2) $\quad CeO_2 + 3\,HCl \rightleftarrows CeCl_3 + {}^3\!/_2\,H_2O + ¼\,O_2 \qquad \Delta_r H^o_{R2}$ (350 °C) = -56.1 kJ/mol

$\Delta_r S^o_{R2}$ (350 °C) = -137.9 J/(K mol)

$\Delta_r G^o_{R2}$ (350 °C) = +33.3 kJ/mol

(R2) $\quad CeO_2 + {}^3\!/_2\,Cl_2 \rightleftarrows CeCl_3 + O_2 \qquad \Delta_r H^o_{R3}$ (350 °C) = +31.5 kJ/mol

$\Delta_r S^o_{R3}$ (350 °C) = -37.1 J/(K mol)

$\Delta_r G^o_{R3}$ (350 °C) = +55.5 kJ/mol

While all Gibbs enthalpies are positive, $\Delta_r G^o_{R1}$ (350 °C) is lower than the other two. At standard partial pressures, the equilibria of all reactions are on the CeO_2 side, as reflected by the equilibrium constants K_{R1}(350 °C) = 8.23·10^{-3}, K_{R2}(350 °C) = 2.08·10^{-3} and K_{R3} (350 °C) = 3.36·10^{-5}.

However, as listed in **Table S 1**, the conditions in our reactor are far from standard conditions. Under oxidizing (so-called "mild") conditions, $p_{in,HCl}$ = 100 mbar and p_{in,O_2} = 200 mbar. H_2O and Cl_2 are considered to be present only as impurities (10 ppm = 10^{-2} mbar) at the reactor inlet, i.e., $p_{in,H_2O} = p_{in,Cl_2}$ = 10^{-2} mbar. The activities of the solids are $a_{CeO_2} = a_{CeCl_3}$ = 1, assuming that the catalyst consists of a heterogeneous mixture of CeO_2 and $CeCl_3$. Using **S 25** yields the corresponding Gibbs enthalpies listed in **Table S 1**. At the reactor inlet, they quite differ from the standard values: $\Delta_r G_{R1}$ (350 °C, p_{in}) = -71.6 kJ/mol, $\Delta_r G_{R2}$ (350 °C, p_{in}) = -25.3 kJ/mol and $\Delta_r G_{R3}$ (350 °C, p_{in}) = +135.7 kJ/mol. The largest contributions here is given by the partial pressures of H_2O and Cl_2 ($\Delta\mu_{dry}(H_2O) = R·T·\log(10^{-5})$ = -59.6 kJ/mol), i.e., the strong deviations between $\Delta_r G°$ and $\Delta_r G$ are caused by the absence of chlorination products.

Table S 1: Overview of partial pressures of different species i used in the calculation under different pressure conditions at 350 °C.

| | | \multicolumn{4}{c}{p / mbar} | | | \multicolumn{3}{c}{$\Delta_r G$ / (kJ / mol)} |
		HCl	O$_2$	H$_2$O	Cl$_2$	R1	R2	R3
standard	$p°$	1000	1000	1000	1000	+25.9	+33.3	+55.5
inlet, dry	$p_{in,i}$	100	200	10^{-2}	10^{-2}	-71.6	-25.3	+135.7
inlet, humid	$p_{in,humid,i}$	100	200	10	10^{-2}	+3.6	+27.7	+135.7
Outlet, dry	$p_{out,i}$	13.5	178.4	43.2	43.2	+78.3	+70.1	+70.4
1.5 % conversion, dry	$p_i(\xi=1.5\%)$	98.5	199.6	0.75	0.75	+52.1	+55.1	+64.1

As outlined above, the absence of H$_2$O (dry conditions) at the reactor inlet drives (R1) and (R2) to the CeCl$_3$ side (as indicated by the negative signs of $\Delta_r G_{R1}$ and $\Delta_r G_{R2}$. Assuming humid conditions at $\approx$ 1 % H$_2$O (relative to total gas feed at 1 bar), i.e., $p_{in,humid,HCl}$ = 10 mbar, raises these Gibbs enthalpies to $\Delta_r G_{R1}$(350 °C, $p_{in,humid,i}$) = +3.8 kJ/mol and $\Delta_r G_{R2}$(350 °C, $p_{in,humid,i}$) = +27.7 kJ/mol, shifting the chlorination equilibrium toward CeO$_2$ already at the reactor inlet. This is due to the increased chemical potential of H$_2$O in the gas feed given by $\Delta\mu_{humid}$(H$_2$O) = $R \cdot T \cdot \log(10^{-2})$ = -11.4 kJ/mol, compared to $\Delta\mu_{dry}$(H$_2$O) = -59. H$_2$O does not participate in (R3), therefore $\Delta_r G_{R3}$ is not affected by adding water to the gas stream.

As evident from **Table S 1**, $\Delta_r G$ can be negative only at the reactor inlet under dry conditions. This means tht "no water" and "a little bit of water" makes a very large difference for the chlorination by HCl by changing the free enthalpy of the chlorination reactions (R1) and (R2) from negative (favored chlorination) to somewhat positive (slightly favored reoxidation). Fortunately, H$_2$O is produced by the Deacon reaction, thus stabilizing CeO$_2$ against bulk chlorination, as evident from $\Delta_r G$ at a conversion ξ = 1.5 % listed in **Table S 1**. Assuming gas phase equilibrium at the reactor outlet (at 350 °C, K_{Deacon} = 24.2) at oxidizing conditions as above yields equilibrium partial pressures $p_{out,HCl}$ = 13.5 mbar, p_{out,O_2} = 178.4 mbar, p_{out,H_2O} = p_{out,Cl_2} = 43.2 mbar, which corresponds to 86.5 % HCl conversion. Under these conditions the free enthalpy for chlorination by HCl is strongly positive for all chlorination reactions, indicating that very little chlorination will take place due to the reduced partial pressure of HCl, high p(O$_2$)/p(Cl$_2$) ratio, and increased partial pressure of H$_2$O.

Chlorination by Cl$_2$ (R3), however, must receive special attention because the conditions at the reactor inlet are unfavorable due to the high excess of O$_2$ and absence of Cl$_2$, giving a strongly positive reaction enthalpy (+135.7 kJ/mol). Since O$_2$ is consumed and Cl$_2$ is produced by the Deacon reaction along the reactor, $\Delta_r G_{R2}$ will decrease downstream to +52.1 kJ/mol when the Deacon reaction is equilibrated. However, the positive sign of $\Delta_r G_{R1}$ (350 °C, p_{out}) indicates that the equilibrium of (R3) is still on the CeO$_2$ side. Since H$_2$O does not participate in reaction (R3), the humidity inside the reactor has no influence on R2. This may lead one to believe that this reaction can be safely neglected. However, including this reaction is crucial because it is the re-oxidation reaction in the ideal Mars-van-Krevelen-type Deacon cycle given in **Figure 2b** (in the main text). Due to its strongly positive reaction enthalpy under all conditions, it strongly contributes to re-oxidation under all conditions, which plays a major role at the reactor inlet under dry conditions, where H$_2$O is absent in the gas feed.

Section S 2.3: Non-equilibrium thermodynamics

The above considerations illustrate that (R1), (R2) and (R3) are competing reactions under the non-equilibrium conditions imposed on the catalyst by the constant feed of fresh reactants. While for (R1) and (R2) the equilibrium can be either on the CeO_2 or the $CeCl_3$ side, for it is always on the CeO_2 side for (R3), which means that (R1) and (R2) are responsible for catalyst chlorination, while (R3) is mainly responsible for re-oxidation. The actual equilibration of the solid phase with the gas phase is prevented in the flow reactor, where the partial pressures of reactants are only a function of the position along the catalyst bed (x) in the steady state, but not a function of time. In order to model the chlorination along the catalyst bed, we established a simple kinetic model as described in the following.

With $k_{f,R1}$ and $k_{r,R1}$, $k_{f,R2}$ and $k_{r,R2}$, and $k_{f,R3}$ and $k_{r,R3}$ denoting the forward and backward rate constants of reactions (R1), (R2) and (R3), the rate of catalyst chlorination can be expressed as the derivative of the mole fractions x_{CeCl_3} by time,

$$\frac{dx_{CeCl_3}}{dt} = -\frac{dx_{CeO_2}}{dt}$$

$$= k_{f,R1} \cdot p_{HCl}^4 \cdot x_{CeO_2} - k_{r,R1} \cdot p_{H_2O}^2 \cdot P_{Cl_2}^{1/2} \cdot x_{CeCl_3} + k_{f,R2} \cdot p_{HCl}^3$$

$$\cdot x_{CeO_2} - k_{r,R2} \cdot p_{H_2O}^{3/2} \cdot P_{O_2}^{1/4} \cdot x_{CeCl_3} + k_{f,R3} \cdot p_{Cl_2}^{3/2} \cdot x_{CeO_2} - k_{r,R3} \cdot P_{O_2}$$

$$\cdot x_{CeCl_3}, \qquad \text{S 1}$$

assuming that the apparent reaction orders are equivalent to the stoichiometric coefficients. This assumption usually proves to be wrong in microkinetics, but since nothing is known about the chlorination kinetics on the microscopic scale, we use the most straightforward approach. In the steady state,

$$\frac{dx_{CeCl_3}}{dt} = 0.$$

Substituting

$$x_{CeO_2} = 1 - x_{CeCl_3} \qquad \text{S 2}$$

in   S 1, and solving for x_{CeCl_3} yields the formal expression

$$x_{CeCl_3}$$

$$= \frac{k_{f,R1} \cdot p_{HCl}^4 + k_{f,R2} \cdot p_{HCl}^3 + k_{f,R3} \cdot p_{Cl_2}^{3/2}}{k_{f,R2} \cdot p_{HCl}^4 + k_{f,R2} \cdot p_{HCl}^3 + k_{f,R3} \cdot p_{Cl_2}^{3/2} - k_{r,R1} \cdot p_{H_2O}^2 \cdot p_{Cl_2}^{1/2} - k_{r,R2} \cdot p_{H_2O}^{3/2} \cdot p_{O_2}^{1/4} - k_{r,R3} \cdot p_{O_2}}, \qquad \text{S 3}$$

which contains the reaction rate constants as unknown parameters. The forward and backward rate constants of reaction j, $k_{f,j}$ and $k_{r,j}$, are connected by the respective equilibrium constants K_j, which can be computed using the thermodynamic data and formulae given in **Section S 2**, using

$$K_j = \frac{k_{f,j}}{k_{r,j}}. \qquad \text{S 4}$$

However, the relationships between the rate constants for different pathways (R1), (R2) and (R3) are unknown, and there exists no formal connection which can be derived from thermodynamics alone. The relationship between $k_{f,R1}$, $k_{f,R2}$ and $k_{f,R3}$ depends on the actual kinetics (mechanism and activation energies) of the three chlorination/re-oxidation reaction pathways. Since the actual kinetics of chlorination and re-oxidation are essentially unknown, we assume that the higher the thermodynamic driving force for the reaction, the faster it will proceed, i.e.,

$$\frac{k_{f,R2}}{k_{f,R1}} = f_2 \frac{K_{R2}}{K_{R1}} \text{ and} \qquad\qquad \text{S 5}$$

$$\frac{k_{f,R3}}{k_{f,R1}} = f_3 \frac{K_{R3}}{K_{R1}}. \qquad\qquad \text{S 6}$$

Since our simulations will be time-independent, the results only depend on the of $k_{f,R2}/k_{f,R1}$ and $k_{f,R3}/k_{f,R1}$. As a reference, $k_{f,R1}$ is set to 1 s^{-1}, so that

$$k_{r,R1} = \frac{1 \text{ s}^{-1}}{K_{R1}}. \qquad\qquad \text{S 7}$$

Combining Eqs.   S 5 and   S 7 to solve for $k_{f,R2}$ and $k_{r,R2}$ gives

$$k_{f,R2} = \frac{K_{R2}}{K_{R1}} f_2 \text{ s}^{-1} \text{ and} \qquad\qquad \text{S 8}$$

$$k_{r,R2} = \frac{k_{f,R2}}{K_{R2}} = \frac{f_2 \text{ s}^{-1}}{K_{R1}}. \qquad\qquad \text{S 9}$$

Similarly,

$$k_{f,R3} = \frac{K_{R3}}{K_{R1}} f_3 \text{ s}^{-1} \text{ and} \qquad\qquad \text{S 10}$$

$$k_{r,R3} = \frac{k_{f,R3}}{K_{R3}} = \frac{f_3 \text{ s}^{-1}}{K_{R1}}. \qquad\qquad \text{S 11}$$

The prefactors f_2 and f_3 are adapted to experimentally determined chlorination degrees under dry conditions (which yields $f_2 \cong 16$ and $f_3 \cong 6.3 \cdot 10^{-2}$). The factors were adapted to reproduce the experimentally observed turning point of the chlorination degree with respect to temperature (**Figure 1b** in the main text) while minimizing the temperature range in which the transition from CeCl$_3$ to CeO$_2$ takes place. The degree of chlorination obtained in the following simulations is determined by these parameters, but we emphasize that the calculated *trends* are not sensitive to f_2 and f_3 and hold for all values of f_2 and f_3. The resulting rate constants for $f_2 \cong 0.1$ and $f_3 \cong 1.6 \cdot 10^{-6}$ at 350 °C are compiled in **Table S 2**.

Table S 2: Compilation of rate constants as applied in our non-equilibrium model.

		formula		value	
i	f_i	$k_{f,i}$	$k_{r,i}$	$k_{f,i}\,/\,s^{-1}$	$k_{r,i}\,/\,s^{-1}$
R1	–	$1\ s^{-1}$	$k_{r,R1} = \dfrac{1\ s^{-1}}{K_{R1}}$	1	64.4
R2	0.1	$k_{f,R2} = \dfrac{K_{R2}}{K_{R1}} f_2\ s^{-1}$	$k_{r,R2} = \dfrac{f_2\ s^{-1}}{K_{R1}}$	$2.0 \cdot 10^{-2}$	6.4
R3	$1.6 \cdot 10^{-6}$	$k_{f,R3} = \dfrac{K_{R3}}{K_{R1}} f_3\ s^{-1}$	$k_{r,R3} = \dfrac{f_3\ s^{-1}}{K_{R1}}$	$2.7 \cdot 10^{-9}$	$1.0 \cdot 10^{-4}$

By substituting $k_{f,i}$ and $k_{r,i}$ as given in

Table S 2 into **S 3**, the mole fraction of $CeCl_3$ in the steady state is given by

$$x_{CeCl_3}$$
$$= \frac{1 \cdot p_{HCl}^4 + \frac{K_{R2}}{K_{R1}} f_2 \cdot p_{HCl}^3 + \frac{K_{R3}}{K_{R1}} f_3 p_{Cl_2}^{3/2}}{1 \cdot p_{HCl}^4 + \frac{1}{K_{R1}} p_{H_2O}^2 \cdot p_{Cl_2}^{1/2} + \frac{K_{R2}}{K_{R1}} f_2 \cdot p_{HCl}^3 + \frac{f_2}{K_{R1}} \cdot p_{H_2O}^{3/2} \cdot p_{O_2}^{1/4} + \frac{K_{R3}}{K_{R1}} f_3\, p_{Cl_2}^{3/2} + \frac{f_3}{K_{R1}} \cdot p_{O_2}} . \qquad \text{S 12}$$

Section S 2.4: Reactor model

In a plug-flow reactor in the steady state, the partial pressures and the catalyst composition are a function of the position along the catalyst bed x, i.e.,

$$x_{CeCl_3}(x) = \left[1 \cdot p_{HCl}^4(x) + \frac{K_{R2}}{K_{R1}} f_2 \cdot p_{HCl}^3(x) + \frac{K_{R3}}{K_{R1}} f_3 p_{Cl_2}^{3/2}(x) \right] \Big/ \Big[1 \cdot p_{HCl}^4(x) +$$
$$\frac{1}{K_{R1}} p_{H_2O}^2(x) \cdot p_{Cl_2}^{1/2}(x) + \frac{K_{R2}}{K_{R1}} f_2 \cdot p_{HCl}^3(x) + \frac{f_2}{K_{R1}} \cdot p_{H_2O}^{3/2}(x) \cdot p_{O_2}^{1/4} + \frac{K_{R3}}{K_{R1}} f_3\, p_{Cl_2}^{3/2}(x) + \frac{f_3}{K_{R1}} \cdot \qquad \text{S 13}$$
$$p_{O_2}(x) \Big]$$

The progress of the Deacon reaction along the catalyst bed is expressed in terms of the HCl conversion as a function of the position, $\xi(x)$. The plug-flow reactor employed in our experiments operates at low HCl conversions ($\xi_{out} < 5\ \%$) using a very small amount of catalyst (20 mg). Due to the low conversion, differential operation can be assumed, which means that the conversion increases linearly along the catalyst bed:

$$\xi(x) = \xi_{out}\, x, \qquad \text{S 14}$$

where x denotes the position along the catalyst bed ($0 \leq x \leq 1$) and ξ_{out} is the final conversion at the reactor outlet. ξ_{out} is quantified experimentally as described in the main text.

Due to the Deacon reaction taking place in the reaction zone of the reactor, the partial pressures of the reactants are a function of the position along the catalyst bed, i.e.,

$$p_{HCl}(x) = p_{in,HCl}\big(1 - \xi(x)\big) = p_{in,HCl}(1 - \xi_{out}\, x), \qquad\qquad \text{S 15}$$

$$p_{O_2}(x) = p_{in,O_2} - \frac{1}{4}\xi(x)p_{in,HCl} = p_{in,O_2} - \frac{1}{4}\xi_{out}\, x\, p_{in,HCl}, \qquad\qquad \text{S 16}$$

$$p_{H_2O}(x) = p_{in,H_2O} + \frac{1}{2}\xi(x)p_{in,HCl} = p_{in,H_2O} + \frac{1}{2}\xi_{out}\, x\, p_{in,HCl},\ \text{and} \qquad\qquad \text{S 17}$$

$$p_{Cl_2}(x) = p_{in,Cl_2} + \frac{1}{2}\xi(x)p_{in,HCl} = p_{in,Cl_2} + \frac{1}{2}\xi_{out}\, x\, p_{in,HCl}. \qquad\qquad \text{S 18}$$

These equations are plugged into **Eq. S 13**, which ultimately yields the chlorination degree $x_{CeCl_3}(x)$ as a function of the position along the catalyst bed.

Experimentally, only the average chlorination degree is determined because the whole sample (20 mg) is taken from the reactor and analyzed by XRD. The mean chlorination degree, $\overline{x_{CeCl_3}}$, is obtained by numerically integrating $x_{CeCl_3}(x)$ over the catalyst bed:

$$\overline{x_{CeCl_3}} = \int_0^1 x_{CeCl_3}(x)dx. \qquad\qquad \text{S 19}$$

In **figure S5** and **Figure 3** we present the model simulations of chlorination of CeO_2 depending on the temperature and the conversion.

Section 2.5: Temperature-dependency of chlorination

The model described in the previous sections was applied to rationalize the observed temperature dependency of the chlorination degree shown in **Figure 1A** in the main text. We observe experimentally that chlorination only occurs at temperatures below 380 °C, but not at temperatures higher than 380 °C. Our simulation at 350 °C under conditions similar to our experiment (**Figure S 5**, black curve) is able to qualitatively reproduce this trend of reducing chlorination degree with increasing temperature. The chlorination degree decreases with temperature because both of the favorable chlorination reactions (R1) and (R2) are exothermic, which shifts the equilibrium of the reactions to the educt (CeO_2) side. Consequentially, the ratio between forward (chlorination) and backward (reoxidation) reactions is shifted backward, reducing in a lowered degree of chlorination in the nonequilibrium steady state with increasing temperature.

Adding 1 % H_2O to the gas stream results in substantial decrease of the chlorination degree at all temperatures. We note that the degree of CeO_2 stabilization is sensitive to the parameter f_2 in our model, so that the effect of adding H_2O may be over- or underestimated in the model. However, adding H_2O *never* leads to increasing chlorination, regardless of parameter choice.
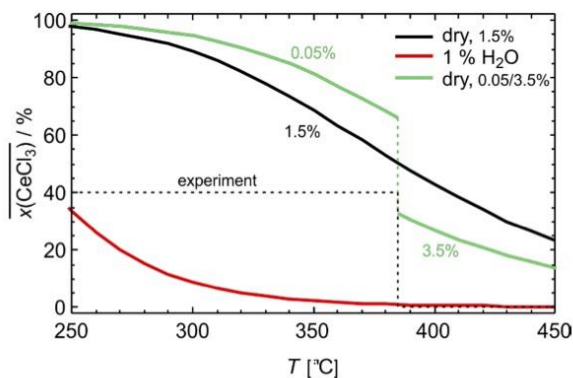
Figure S 5: Chlorination degree of CeO₂ as a function of temperature at 1.5% HCl conversion under mild conditions without (black) and with 1% water (red), as modeled by our non-equilibrium approach. Assuming 0.05 % conversion at low and 3.5 % conversion at high temperature and dry conditions results in the green curve.

It is immediately obvious that the model calculations fail to reproduce the experimentally observed sudden decrease in chlorination degree from 40 % to 0 % at 380 °C, indicated by the dashed line in **Figure S 5**. Part of the deviation can be explained by the temperature dependency of the conversion. Our model assumes 1.5 % regardless of temperature. Employing instead the experimentally obtained steady-state conversions of 0.05 % at temperatures lower than 380 K and 3.5 % at higher temperatures results in increased and decreased chlorination at lower and higher temperatures, respectively, which suggests that the chlorination is self-promoting: the lower the initial conversion, the higher the chlorination rate, which results in decreasing conversion. However, the present modelling approach cannot result in a true step function as observed experimentally due to the simple microkinetic approach that depends on the partial pressures and (bulk) catalyst composition in a polynomial fashion where three chlorination/dechlorination reactions are independent of each other with reaction orders identical to the stoichiometric coefficients.

A more accurate way to model the reaction would be to decompose the chlorination into elementary steps. This would make the rates of chlorination reactions depend on the accessible surface areas of CeO₂ and CeCl₃ and coverages and desorption rates of reactants in a nonlinear manner, none of which are considered in the present models. The chlorination of CeO₂ may be considered to be competing against Cl₂ formation in the sense that a Cl atom adsorbed on the CeO₂ surface can either be incorporated into the CeO₂ bulk, contributing to chlorination, or recombine with Cl₂ and desorb. Cl₂ recombination and desorption has an activation energy of 1.42 eV at 0 K [1], while the migration of adsorbed Cl from the surface into a vacancy is exothermic by 2.15 eV [1]. Increasing temperature increases kinetic preference for migration of Cl from the subsurface to the bulk and desorption, rather than incorporation of Cl into the bulk. This notion is consistent wtih the reduction of chlorination rate versus temperatures as observed in our experiment (**Figure S 1**). The atomic-scale processes that lead to the actual phase transformation of (chlorinated) CeO₂ to CeCl₃ are not well-understood. Since the incorporation of Cl from the subsurface into deeper bulk layers in penalized by 3 eV [1], the bulk solubility of Cl in CeO₂ can be assumed as small, thus preferring formation of bulk CeCl₃ once the CeO₂ subsurface is saturated with Cl. It is possible that this required saturation concentration of Cl in the subsurface cannot be reached at temperatures higher 380 °C under the conditions employed in our reactor because Cl₂ desorption becomes favored over Cl incorporation into the bulk. As a consequence, bulk CeCl₃ detectable by XRD would not be formed. This interpretation agrees very well with the trends observed in temperature-dependent PGAA experiments [2] that observe

increasing Cl uptake (reflected by Ce/Cl ratio) at high O_2 excess (9:1) with decreasing temperature in a smooth fashion. In contrast to XRD, PGAA measures the total Cl content of the sample, rather than ordered phases. This subsurface Cl is not detectable by XRD, so that we observe a step where the chlorination degree drops to zero instantaneously once the bulk solubility limit of Cl in CeO_2 is not achieved anymore, rather than a smooth transformation as obtained by PGAA and as suggested by the model that does not take limited bulk solubility of Cl as a threshold for $CeCl_3$ formation into consideration.

Section S 3: Formulas and definitions

Section S 3.1: General Thermodynamics

Standard formation enthalpy

$$\Delta_f H°(T) = \Delta_f H^\theta + \int_{T^\theta}^{T} c_p(T) dT$$

S 20

Standard entropy

$$S°(T) = S^\theta + \int_{T^\theta}^{T} \frac{c_p(T)}{T} dT$$

S 21

Standard reaction enthalpy

$$\Delta_r H°(T) = \sum_i \nu_i \, \Delta_f H_i°(T)$$

S 22

Standard reaction entropy

$$\Delta_r S°(T) = \sum_i \nu_i \, S_i°(T)$$

S 23

Standard free enthalpy/Gibbs enthalpy (of reaction)

$$\Delta_r G°(T) = \Delta_r H°(T) - T \, \Delta_r S°(T)$$

S 24

Free enthalpy/Gibbs enthalpy

$$\Delta_r G(T, p_1, p_2, \dots) = \Delta_r G°(T) + k_B T \sum_i \nu_i \ln\left(\frac{pi}{p°}\right)$$

S 25

Equilibrium constant

$$K = e^{-\frac{\Delta_r G°(T)}{RT}} = \prod_i a_{i,eq}^{\nu_i} = \prod_i \left(\frac{p_{i,eq}}{p°}\right)$$

S 26

Reaction quotient

$$Q = e^{-\frac{\Delta_r G(T, p_1, p_2 \dots)}{RT}} = \prod_i a_i^{\nu_i} \cong \prod_i \left(\frac{p_i}{p^\circ}\right)$$

<div align="right">S 27</div>

Section S 3.2: Thermochemical constants

$$T^\circ = 298.15 \text{ K}$$

$$p^\circ = 10^5 \text{Pa} = 1000 \text{ mbar}$$

$$k_B = 1.38 \cdot 10^{-23} \text{J/(K mol)}$$

$$R = 8.314 \text{ J/(K mol)}$$

Section S 3.3: Thermodynamic data of reactants

[3]

$c_{p,HCl}(T)/(\text{K mol J}^{-1})$

$$= 32.12 - 0.050 \left(\frac{T}{1000 \, K}\right)^{-2} - 13.46 \left(\frac{T}{1000 \, K}\right) + 19.87 \left(\frac{T}{1000 \, K}\right)^2$$
$$- 6.85 \left(\frac{T}{1000 \, K}\right)^3$$

$\Delta_f H_{HCl}^\circ = -92.31 \text{ kJ/mol}$ $\qquad\qquad$ $S_{HCl}^\circ = 186.9 \text{ J/(K mol)}$

O$_2$ (300-1000 K) [3]

$c_{p,O_2}(T)/(\text{K mol J}^{-1})$

$$= 31.32 - 0.0073 \left(\frac{T}{1000 \, K}\right)^{-2} - 20.24 \left(\frac{T}{1000 \, K}\right) + 57.87 \left(\frac{T}{1000 \, K}\right)^2$$
$$- 36.51 \left(\frac{T}{1000 \, K}\right)^3$$

$\Delta_f H_{O_2}^\circ = 0$ $\qquad\qquad$ $S_{O_2}^\circ = 205.1 \text{ J/(K mol)}$

H$_2$O (300-1000 K) [3]

$c_{p,H_2O}(T)/(\text{K mol J}^{-1})$

$$= 30.09 + 0.082 \left(\frac{T}{1000 \, K}\right)^{-2} + 6.83 \left(\frac{T}{1000 \, K}\right) + 6.79 \left(\frac{T}{1000 \, K}\right)^2 - 2.53 \left(\frac{T}{1000 \, K}\right)^3$$

$\Delta_f H_{H_2O}^\circ = -241.8 \text{ kJ/mol}$ $\qquad\qquad$ $S_{H_2O}^\circ = 188.8 \text{ J/(K mol)}$

Cl$_2$ (300-1000 K) [3]

$$c_{p,Cl_2}(T)/(K\,mol\,J^{-1})$$

$$= 33.05 - 0.159\left(\frac{T}{1000\,K}\right)^{-2} + 12.23\left(\frac{T}{1000\,K}\right) - 12.07\left(\frac{T}{1000\,K}\right)^2$$

$$+ 4.39\left(\frac{T}{1000\,K}\right)^3$$

$$\Delta_f H^{\theta}_{Cl_2} = 0 \qquad\qquad S^{\theta}_{Cl_2} = 223.1\,J/(K\,mol)$$

CeO$_2$ (300-1800 K) [4]

$$c_p(T)\,(K\,mol\,J^{-1}) = 74.48 + 5.837\left(\frac{T}{1000\,K}\right) - 1.297\left(\frac{T}{1000\,K}\right)^{-2}$$

$$\Delta_f H^{\theta}_{CeO_2} = -1090.47\,kJ/mol \qquad\qquad S^{\theta}_{CeO_2} = 62.29\,J/(K\,mol)$$

CeCl$_3$ (300-1040 K) [5-7]

$$c_p(T)\,(K\,mol\,J^{-1}) = 89.05 + 17.9\left(\frac{T}{1000\,K}\right) \text{ [7]}$$

$$\Delta_f H^{\theta}_{CeCl_3} = -1060.5\,kJ/mol\,[6] \qquad\qquad S^{\theta}_{CeCl_3} = 151\,J/(K\,mol)\,[5]$$

References

(1)   Amrute, A.; Mondelli, C.; Moser, M.; Novell-Leruth, G.; López, N.; Rosenthal, D.; Farra, R.; Schuster, M.; Teschner, D.; Schmidt, T.; Pérez-Ramírez, J. *J. Catal.* **2012**, *286*, 287–297.

(2)   Farra, R.; Eichelbaum, M.; Schlögl, R.; Szentmiklósi, L.; Schmidt, T.; Amrute, A.; Mondelli, C.; Pérez-Ramírez, J.; Teschner, D. *J. Catal* **2013**, *297*, 119–127.

(3)   NIST Chemistry Webbook. http://webbook.nist.gov/chemistry.

(4)   Konings, R.; Beneš, O.; Kovács, A.; Manara, D.; Sedmidubský, D.; Gorokhov, L.; Iorish, V.; Yungman, V.; Shenyavskaya, E.; Osina, E. *J. Phys. Chem. Ref. Data* **2014**, *43*, 013101.

(5)   Mu, L.-L.; He, H.-M.; Feng, C.-J. *Chin. J. Chem* **2008**, *26*, 1201–1209.

(6)   Cordfunke, E.; Booij, A. *J. Chem. Thermodynamics* **1995**, *27*, 897–900.

(7)   Gaune-Escard, M.; Bogacz, A.; Rycerz, L.; Szczepaniak, W. *J. Alloys Comp.* **1996**, *235*, 176–181.

5.3 Supporting Information of Article 3

Supporting Information

Catalytic HCl Oxidation Reaction:

Stabilizing Effect of Zr-Doping on CeO$_2$ Nano-rods

Chenwei Li[a,b], Yu Sun[a,b], Igor Djerdj[c], Joachim Sann[b], Pascal Voepel[b], Pascal Cop[b], Felix M Badaczewski[b], Yanglong Guo[a,*], Bernd M. Smarsly[b,*], Herbert Over[b,*]

a) Key Laboratory for Advanced Materials, Research Institute of Industrial Catalysis, School of Chemistry and Molecular Engineering, East China University of Science and Technology, Shanghai 200237, PR China
b) Physikalisch-Chemisches Institut, Justus Liebig University, Heinrich-Buff-Ring 17, 35392 Giessen, Germany
c) Department of Chemistry, J. J. Strossmayer University of Osijek, Ulica cara Hadrijana 8/a, HR-31000 Osijek, Croatia

* *Corresponding authors:* E-mail: herbert.over@phys.chemie.uni-giessen.de; Bernd.Smarsly@phys.Chemie.uni-giessen.de; ylguo@ecust.edu.cn
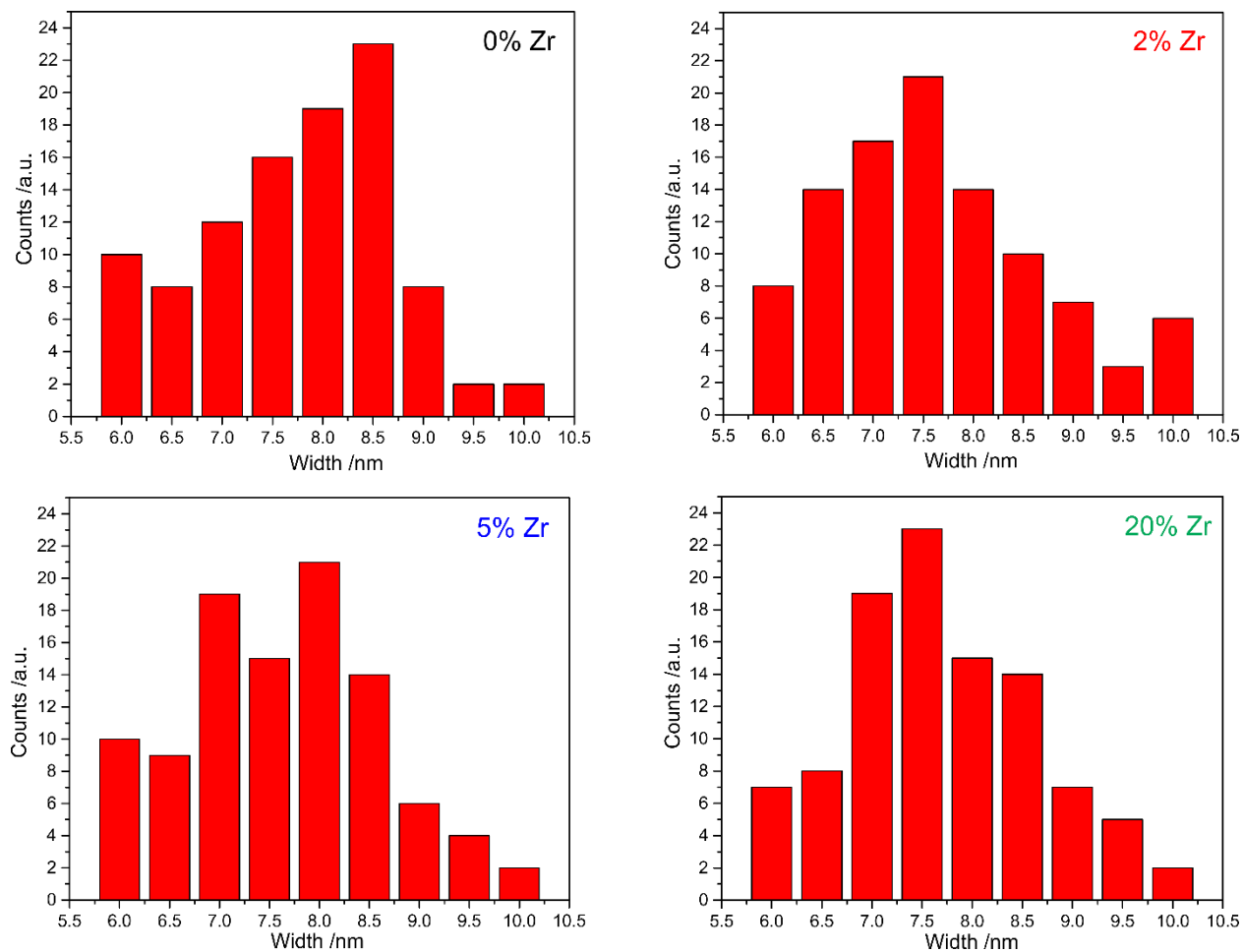
Figure S1: Width histograms of the as-prepared $Ce_{1-x}Zr_xO_2$ nano-rods (x=0 to 0.2). A minimum of 100 rods were measured for each histogram.

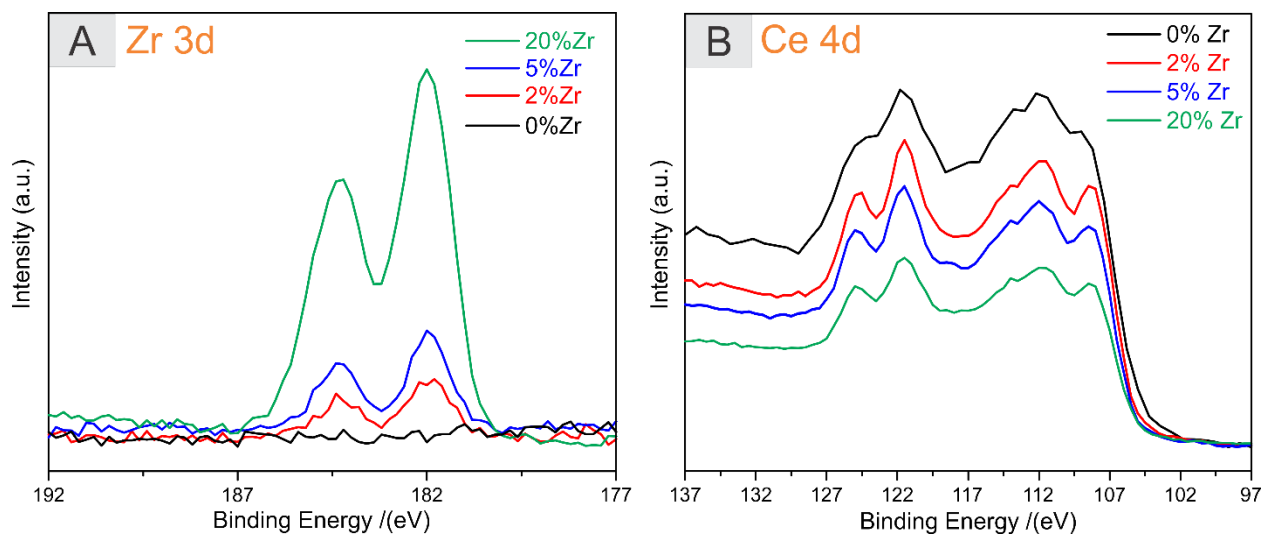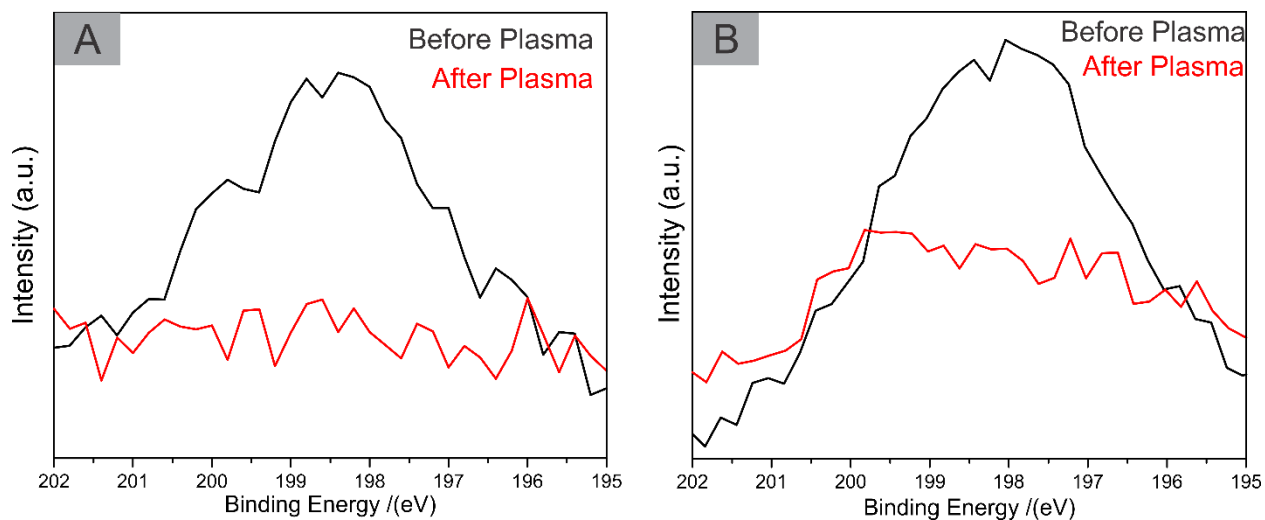**Figure S2**: XPS spectra of Zr 3d and Ce 4d of as-prepared $Ce_{1-x}Zr_xO_2$ nano-rods.

Figure S3: XPS spectra of Cl 2p of used $Ce_{1-x}Zr_xO_2$ nano-rods before and after Plasma treatment. A): CeO_2 nano-rods after Deacon reaction under $Ar:HCl:O_2 = 6:3:1$ and a reaction temperature of 500 °C; B): $Ce_{0.8}Zr_{0.2}O_2$ nano-rods after Deacon reaction under $Ar:HCl:O_2 = 6.5:2.5:1$ and a reaction temperature of 430 °C.
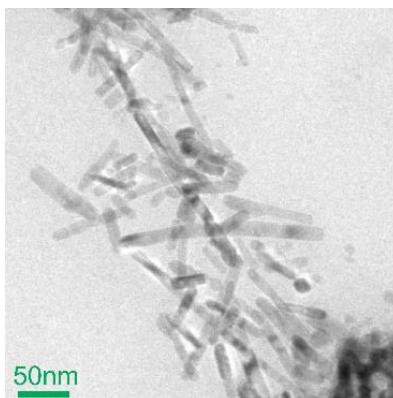
Figure S4: TEM image of CeO$_2$ nano-rods after Deacon reaction (Ar:HCl:O$_2$=6:3:1, T=500 °C). Even under such a harsh reaction condition the nano-rods survived.
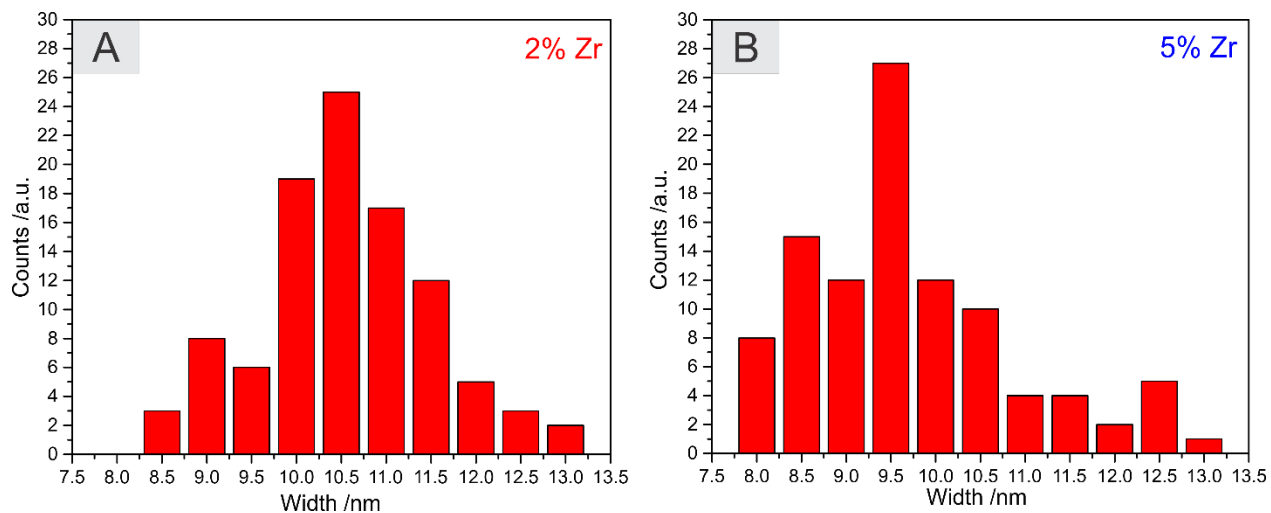
Figure S5: Width histograms of of $Ce_{1-x}Zr_xO_2$ nano-rods after Deacon reaction under the reaction condition of $Ar:HCl:O_2 = 6.5:2.5:1$. A minimum of 100 rods were measured for each histogram. A): $Ce_{0.98}Zr_{0.02}O_2$ and B): $Ce_{0.95}Zr_{0.05}O_2$

5.4 List of Abbreviations

PVC	polyvinyl chloride
MDI	methylene diphenyl diisocyanate
TDI	toluene diphenyl diisocyanate
EDC	ethylene dichloride
VOC	volatile organic compounds
WGS	water-gas shift reaction
SMR	steam methane reforming
XRD	X- ray diffraction
XPS	X- ray photoelectron spectroscopy
TEM	transmission electron microscopy
SEM	scanning electron microscopy
OSC	oxygen storage capacity
OSCc	complete oxygen storage capacity
STY	space time yield
H_2-TPR	hydrogen temperature programmed reduction
GHSV	gas hourly space velocity
DFT	density functional theory
PGAA	prompt gamma activation analysis
FTIR	fourier-transform infrared spectroscopy
TPD	temperature programmed desorption

5.5 List of Peer-Reviewed Publications and Articles to be Submitted

1. Chenwei Li, Yu Sun, Igor Djerdj, Pascal Vöpel, Carl-Christian Sack, Tobias Weller, Joachim Sann, Rüdiger Ellinghaus, Yanglong Guo, Bernd M. Smarsly, Herbert Over, *Shaped-Controlled CeO_2 Nanoparticles: Stability and Activity in the Catalyzed HCl oxidation Reaction*. **ACS Catalysis**, 7 (**2017**) 6453-6463

2. Chenwei Li, Franziska Hess, Igor Djerdj, Guangtao Chai, Yanglong Guo, Bernd M. Smarsly, Herbert Over, *The stabilizaing effect of water and high reaction temperatures on the CeO_2-catalyst in the harsh HCl oxidation reaction*. **Journal of Catalysis**, 357 (**2018**) 257-262 (**Featured Article**）

3. Chenwei Li, Yu Sun, Igor Djerdj, Joachim Sann, Pascal Vöpel, Pascal Cop, Felix M Badaczewski, Yanglong Guo, Bernd M. Smarsly, Herbert Over, *Catalytic HCl Oxidation Reaction: Stabilizing Effect of Zr-Doping on CeO_2 Nano-rods*. **Applied Catalysis B: Environment**, (to be Submitted)

4. Chenwei Li, Christoph Seitz, Igor Djerdj, Pascal Cop, Junpei Yue, Pascal Vöpel, Federica Bertolotti, Antonella Guagliardie, Yanglong Guo, Herbert Over, Bernd M. Smarsly. *Time development of morphologies evolution of the CeO_2 nano-cubes and nano-rods by hydrothermal methods*. **Crystal Growth & Design** (to be Submitted)

5. Kanka Feng, **Chenwei Li**, Yanglong Guo, Wangcheng Zhan, Binquan Ma, Binwu Chen, Maoquan Yuan, Guanzhong Lu, *An efficient $Cu-K-La/Al_2O_3$ catalyst for catalytic oxidation of hydrogen chloride to chlorine*. **Applied Catalysis B: Environment**, 164 (**2015**) 483-487

6. Yu Sun, **Chenwei Li**, Yanglong Guo, Wangcheng Zhan, Yun Guo, Li Wang, Yunsong, Wang,Guanzhong Lu, *Catalytic oxidation of hydrogen chloride to chlorine over $Cu-K-Sm/\gamma-Al_2O_3$ cataltst with excellent catalytic performance*. **Catalysis Today**, (In Press)

7. Kanka Feng, **Chenwei Li**, Yanglong Guo, Wangcheng Zhan, Binquan Ma, Binwu Chen, Maoquan Yuan, Guanzhong Lu, *Effect of KCl on the performance of $Cu-K-La/\gamma-Al_2O_3$ catalyst for HCl oxidation*. **Chinese. J. Catal**, 35 (**2014**) 1359-1363

8. Sven Urban, Igor Djerdj, Paolo Dolcet, Limei Chen, Maren Moller, Omeir Khalid, Hava Camuka, Rudiger Ellinghaus, **Chenwei Li**, Sivia Gross, Peter J. Klar, Bernd Smarsly, and Herbert Over, *In Situ Study of the Oxygen-Induced Transformation of Pyrochlore $Ce_2Zr_2O_{7+X}$ to the κ-$Ce_2Zr_2O_8$ Phase*. **Chem. Mater**. 29 (**2017**) 9218-9226